Master's thesis

NTNU
Norwegian University of Science and Technology
Faculty of Natural Sciences
Department of Chemical Engineering

Quoc Anh Tran

Development of Li_2ZrO_3-coated NMC811 Cathode via Wet-Surface Coating Process and its Electrochemical Evaluation in Argyrodite-Based Solid-State Lithium Batteries

Master's thesis in Chemical Engineering
Supervisor: Gisle Øye
Co-supervisor: Daniel Rettenwander
January 2023

NTNU
Norwegian University of
Science and Technology

Quoc Anh Tran

Development of Li_2ZrO_3-coated NMC811 Cathode via Wet-Surface Coating Process and its Electrochemical Evaluation in Argyrodite-Based Solid-State Lithium Batteries

Master's thesis in Chemical Engineering
Supervisor: Gisle Øye
Co-supervisor: Daniel Rettenwander
January 2023

Norwegian University of Science and Technology
Faculty of Natural Sciences
Department of Chemical Engineering

NTNU
Norwegian University of
Science and Technology

NTNU
Kunnskap for en bedre verden

Department of Chemical Engineering

TKP4900 Chemical Process Technology, Master's Thesis

Development of Li_2ZrO_3-coated NMC811 Cathode via Wet-Surface Coating Process and its Electrochemical Evaluation in Argyrodite-Based Solid-State Lithium Batteries

Author:
Quoc Anh Tran

External Supervisor:
Daniel Rettenwander
Internal Supervisor
Gisle Øye

December, 2022

Acknowledgement

I would like to express my affection towards my external supervisor, Associate Professor Daniel Rettenwander, Department of Materials Science and Engineering for allowing me to complete my master's thesis in his group. I have acquired a variety of knowledge in the field of batteries as well as a wealth of laboratory experience. I would also want to thank him and my co-supervisor, Dr Mir Mehraj Ud Din, Department of Materials Science and Engineering Faculty of Natural Sciences for their guidance and dedication to scientific supervision during the period of my thesis project.

I would also want to express my sincere appreciation to my internal supervisor, Professor Gisle Øye, Department of Chemical Engineering, NTNU, for his valuable support with the master's thesis project.

In addition, I would like to thank the remaining members of the Rettenwander group, PhD Student Hung Quoc Nguyen, PhD Candidate Jin Feng, and PhD Candidate Florian Flatscher, Dr Laras Fadillah for their excellent scientific discussions and assistance in the lab, as well as our lab engineer Pei Na Kui for creating a safe and pleasant lab environment. Thank you all for creating a friendly environment.

Finally, I would like to thank my family for their continuous support that has been shown to me during my my master's degree studies.

Abstract

Conventional Li-ion batteries (LIBs) with a liquid electrolyte are becoming more popular, especially for use in electric vehicles, but there is still a need for improvements in their energy and power densities as well as their reliability and safety. This has reignited interest in all-solid-state batteries (ASSBs), a possible next-generation energy storage technology that uses a solid ceramic electrolyte for ionic conduction rather than a liquid electrolyte. Application of Ni-rich layered oxide known to as NCM or NMC, cathode active materials (CAMs) with lithium thiophosphate solid electrolytes (SEs), are important for the development of ASSBs. But because of some technical problems with the interface of CAM/SE, ASSBs cannot yet match the performance of traditional LIBs. Li_6PS_5Cl (LPSCl) has been the preferred SE for ASSB research thanks to its strong ionic conductivity and favorable mechanical properties. However, due to stability problems of the SE, LPSCl has decomposition reactions at the interfaces during cycling. Coating a protective layer on the NCM secondary particles is a good way to suppress or at mitigate these side reactions.

A facile wet coating process has been successfully designed in this work, to achieve Li_2ZrO_3 (LZO) coated $LiNi_{0.8}Co_{0.1}Mn_{0.1}O_2$ (NMC811). Different LZO weight percentage, types of precursors, conditions of solvent evaporation, and calcination temperatures were investigated in order to tune the distribution, achieve uniformity, and control the crystallinity of LZO coating layers. The optimal coating process led to very uniform and conformal coating layer of LZO which have been revealed the morphology by X-ray diffraction (XRD), scanning transmission electron microscopy (S(T)EM) and energy dispersive X-ray spectroscopy (EDX) analysis. The cross-sectioning method is done in order to determine the distribution of the coating layer and to evaluate the doping effect of on NMC811 in high calcination temperature. In addition, the pretreatment of water-sensitive NMC materials with citric acid in the moisture solvent, which is required in other commonly used sol-gel coating methods, is unnecessary in our investigation of the water-free process to create uniform LZO coatings. Moreover, this coating approach is appropriate for large-scale industrial application and commercialization of Ni-rich NCM-based cathodes due to its simplicity, cost-effectiveness, energy efficiency, scalability, and reproducibility.

Pellet-type ASSBs were fabricated using polyether ether ketone (PEEK) cells. For creating cathode composite, the ratio of 11:16:1 to load CAM (coated CAM); SE; and carbon is used. Li-In alloy is produced via coulometric titration of indium by lithium and is utilized as the anode, and LPSCl pellet is positioned between two electrodes. The coatings have not only increased the specific capacity of ASSB during the initial discharge(from 103 mAh/g to 149 mAh/g), but they have also improved other electrochemical performances of the Ni-rich NM811 in terms of C-rate and cycling stability.

Table of Contents

List of Figures

List of Tables

Chapter 1

Introduction

1.1 Energy Storage

Clean and reliable energy supply is undoubtedly one of the most important issues of the 21st century, with implications for our everyday lives, the global environment, economy, and human health. Even though combustion-based energy technologies will still be a big part of meeting our energy needs for the foreseeable future, they have a number of problems, like such a fast rise in greenhouse gas emissions and long-term damage to the environment. Scientists and engineers are searching for methods to provide and store energy that are sustainable, clean, and highly efficient because fossil fuels are running out and environmental concerns are growing [1, 2]. Renewable and environmentally friendly energy sources, such as solar and wind, are alternative energy generating methods. However, they are irregular and dependent on the time, weather, seasons, and regions. LIBs are becoming more desirable than ever. In the last several decades, this energy system has experienced major advancements and considerable promise in many applications, including rechargeable eco-friendly electronic products, portable electronics, hybrid/pure electric vehicles, and smart grids [3]. Moreover, they transform chemical energy directly into electrical energy with a high degree of efficiency and little or no environmental impact.

1.2 Rechargeable Li-ion Batteries and Li Metal Batteries

In terms of specific capacity, operating voltage, rate capability, long-term cycle performance, and safety, Li-ion battery is one of the most promising energy storage technologies compared to classic nickel-cadmium batteries, lead-acid batteries, and nickel-metal hydride batteries [4]. For example, the ideal operating voltage for commercial $LiCoO_2$-based LIBs is 3.7 V, roughly three times that of commercial lead-acid batteries [5]. Since the introduction of the first commercial rechargeable LIBs by SONY in 1991, the LIB has quickly become the dominant power source for portable electronic devices in the commercial market [6]. In recent years, it has also been developed as a power source for electric and hybrid electric vehicles, and it has the potential to power future air transportation [7]. A typical LIB has two electrodes - positive (the cathode) and negative (the anode) electrode - that are separated by the electrolyte. Commonly used cathode materials include $LiCoO_2$, $LiMn_2O_4$, $LiFePO_4$, and $LiMn_{1/3}Co_{1/3}Ni_{1/3}O$. Common anode materials include graphite, silicon-based substances, graphene, and $Li_4Ti_5O_{12}$ [8, 9, 10]. Lithium salt, such as LiPF6, dissolved in organic solvents (ethylene carbonate (EC), dimethyl carbonate (DMC), and diethyl carbonate (DEC), etc.) is the most common electrolyte [11, 12]. To prevent direct contact between electrodes in liquid electrolyte cells, an electrolyte-permeable and electrically insulating porous separator is required. The energy storage and conversion in LIBs is dependent on the migration of Li ions between the cathode and anode, where electrochemical reduction and oxidation occur respectively, driven by the disparity between their chemical potentials [13, 14, 15]. When external power is added, the process in rechargeable batteries reverses, allowing for the release and storage

of energy in a reversible manner. Li ion de/intercalation occurs at both electrodes in LIBs with a graphite anode and a lithium metal oxide cathode, as seen in Figure 1.1. During charging, an external power source charges the cell, forcing electrons to flow from cathode to anode via the external circuit. Following Equation 1.1, the loss of electrons in $LiCoO_2$ causes the oxidation of Co^{3+} to Co^{4+} and the deintercalation of Li ion in order to balance the charge. Then, the Li ions migrate to the graphite anode through the electrolyte, intercalate into the graphite, and recombine with electrons according to Equation 1.2 Due to the fact that the cathode has a larger chemical potential than the anode, the opposite process (discharging) is spontaneous according to Equation 1.3 and Equation 1.4.
During Charging:
Positive electrode (Cathode):

$$LiCoO_{2-x}Li^x - xe^- -> Li_{1-x}CoO_2 \tag{1.1}$$

Negative electrode (Anode):

$$C_6 + xLi^+ + xe^- -> Li_xC_6 \tag{1.2}$$

During Discharging:
Positive electrode (Cathode):

$$Li_{1-x}CoO_2 + xLi^+ + xe^- -> LiCoO_2 \tag{1.3}$$

Negative electrode (Anode):

$$Li_xC_6 - xLi^- - xe^- -> C_6 \tag{1.4}$$

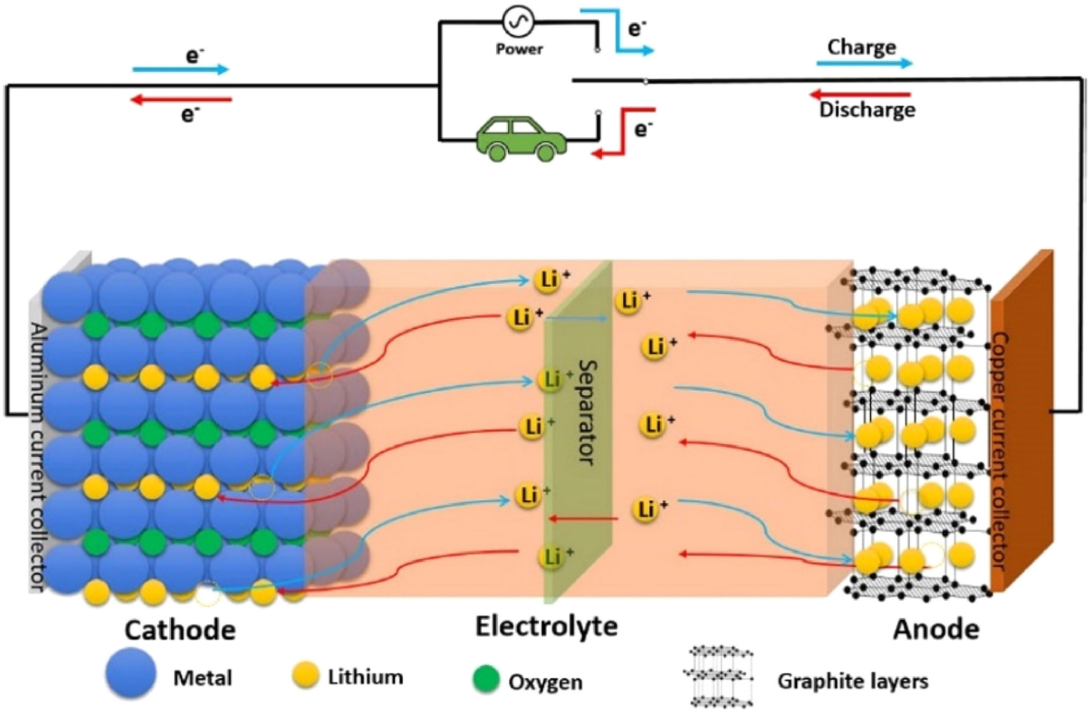

Figure 1.1: Schematic representation of the charge/discharge mechanism of a LIB cell [15]

The specific capacity of $LiCoO_2$ is 137 $mAh.g^{-1}$, since it can only allow half of the Li ion to be taken out without losing structural stability and deeper charging (removal of more than half of the Li ions) will cause oxygen to evolve from the crystal lattice, resulting in rapid capacity fade [16]. Due to this structural instability with deeper charging, as well as the expensive price, limited availability, and high toxicity of cobalt, there has been significant interest in finding new CAMs. In the past ten years, the substitution of cobalt with other transition metals has resulted to one of the most intensively studied CAM families, $LiNi_{1-x-y}Mn_xCo_yO_2$ (NMC or NCM) [17]. In this family of cathode materials, electrochemically inactive Mn maintains a 4^+ oxidation state to stabilize the

structure, while Co may reduce cation site mixing caused by the comparable ionic radii of Li^+ and Ni^{2+}. High-Ni NMC cathodes have a high discharge capacity (200 $mAh.g^{-1}$) because they depend on $Ni^{2+/4+}$ and $Co^{3+/4+}$ redox couples, which provide a greater energy density than $LiCoO_2$.

As LIBs approach the theoretical capacity of cathode/anode materials, particularly graphite anode, Li metal batteries indicate the potential for the development of next-generation high energy density electrochemical energy storage devices. Li metal anode has the largest specific capacity (3840 $mAh.g^{-1}$) of all metal anodes, which is an order of magnitude more than graphite, and the lowest reduction potential (-3.04 V vs standard hydrogen electrode) [18, 19]. However, organic liquid electrolytes are thermodynamically unstable when reduced by Li metal, which results in the formation of a solid electrolyte interphase (SEI) with a high resistance and the consumption of liquid electrolyte [20]. In addition, Li metal anodes exhibit dendrite [18] and the growth of Li dendrites leads to a high surface area of fresh Li that interacts continuously with liquid electrolyte, consuming Li and liquid electrolyte, and ultimately causing cell failure during continuous cycling [18]. Further long-term cycling may cause Li dendrites to penetrate the separator layer, resulting in a cell short circuit that, when combined with the innate flammability of organic solvents, can result in an explosion [20, 18].

All-solid-state batteries, also known as ASSBs, are being looked at as a potential contender for the role of energy storage technology in the future [21]. ASSBs are intended to provide a number of benefits over conventional LIBs, including greater safety, a broader range of operating temperatures, and larger volumetric densities [22]. In the parts that follow, the evolution, present status, and contemporary concerns of ASSBs will be examined in depth.

1.3 All-Solid-State Li Batteries

In general, "ASSB" refers to batteries that are made entirely of solid components. Currently, the term is mostly used to identify ASSBs that are comparable to the components and working mechanism of LIBs which have been described in Section 1.2, but in which the liquid electrolyte and separator have been replaced with a solid [23]. However, the above mentioned functioning concept is rather simple, the charging and discharging processes occuring inside the electrodes of ASSBs are intricate and can be explained. The cell voltage is determined by the difference between the chemical potentials of the active species (lithium) at the two electrodes. The chemical potential may be divided into electronic and ionic contributions [24, 25]. For the cathode side, which is the subject of this thesis, charging/discharging is followed by changes in the electronic and ionic states of the CAM, and consequently its chemical potential [25, 26, 27, 28]. Taking into account the electronic contribution, the energy location of the Fermi level E_F may be used to characterize changes in the electronic states [24, 25]. The CAM can be defined electronically as a small-band gap semiconductor [29]. Consequently, charging and discharging leads in changes to electronic states and energetic state of E_F. Due to the fact that the energetic position is highly reliant on defects such as intrinsic/extrinsic dopants, the process during charging/discharging is dependent on the precise electronic band structure and, therefore, the composition and microstructure of the CAM [30]. In order to correctly represent the changes in the chemical potential during charging/discharging, the respective changes in the ionic states and the interactions between both contributions must be taken into consideration as well as electronic part. Despite the importance of understanding this interaction, it is not essential for comprehending the findings of this thesis. The fundamental structure and microstructure of the analyzed CAM samples are of greater significance, as will be described below. Detailed information on the utilized materials, supplier, ratio of precursors, and the cell fabrication will be found in the next two chapters and will not be discussed further here.

ASSBs can be divided into two categories based on the solid electrolytes (SEs) employed: ASSBs with polymer SEs or polymer-ceramic composite SEs and ASSBs with inorganic SEs. The insufficient interfacial contact between active materials-SEs and the chemo-mechanical expansion of Li cathode materials can result in a high internal cell resistance [31]. Consequently, a minor quantity of liquid electrolyte is often placed between the electrolyte/electrode interface to enhance the performance of the cell, which are thus considered quasi or hybrid ASSBs. As illustrated in Figure 1.2, SSBs that utilize a SE instead of a liquid electrolyte - and preferably a Li metal anode

- may alleviate safety problems and deliver high energy densities[21].

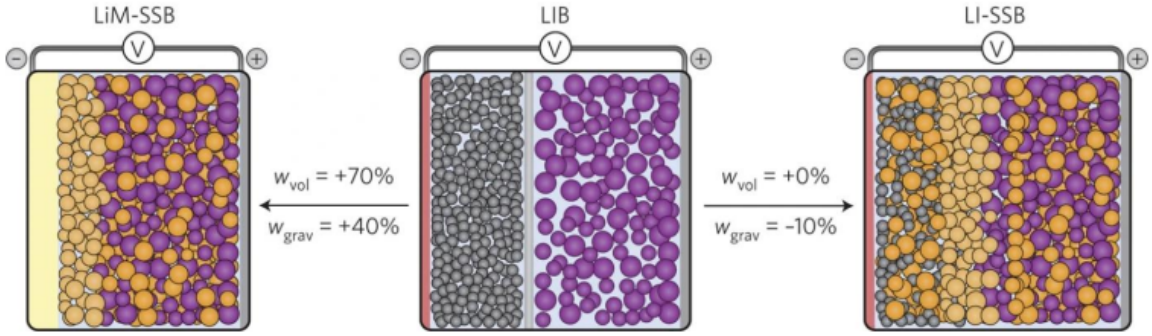

Figure 1.2: Typical battery architecture diagrams for a regular Li-ion battery (center), an all-solid-state Li-ion battery (right), and an all-solid-state Li metal battery (left). W_{vol} and W_{grav} represent the volumetric and gravimetric densities of energy, respectively [21].

ASSBs typically consist of a thin layer of SE as a separator and cathode and anode composites that are a homogenous mixture of active material, SE powder, and electronic conductive material (such as carbon, if necessary) [32]. Li metal anode or other high specific capacity material (such as silicon anode) is necessary to further increase the energy density [33].

Figure 1.3 depicts a standard cell configuration in which ASSB pellets were cycled [34]. The ASSB pellet (10 mm inner diameter) is situated in the middle of the apparatus and is encircled by a cell casing that is positioned in an aluminum framework. The anode is positioned at the bottom of the ASSB pellet design, and lithiated indium alloy anodes were employed. On the top side of the ASSB pellet schematic, cathode is placed. The cathode is composed of a composite material incorporating CAM secondary particles, a thiophosphate-based SE, and a conductive carbon additive. The CAM dominates the electronic partial conductivity, whereas the SE dominates the ionic partial conductivity of the composite cathode. Carbon additives can be used to increase the electronic partial conductivity and simultaneously improve the utilization of the otherwise electronically isolated CAM. In addition, the composite cathodes have a typical porosity range of 8-17% for uniaxially coldpressed ASSBs, which is depending on the precise cell assembly process and the grain size and hardness of the materials utilized. As current collectors, two stainless steel stamps apply pressure to the negative and positive electrode sides, respectively.

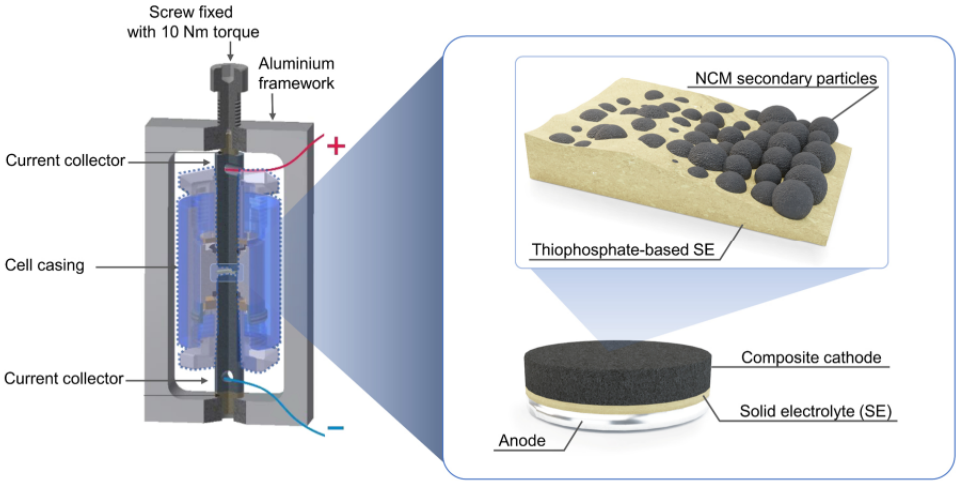

Figure 1.3: Schematic of ASSB pellet structure. The ASSB pellet is positioned in the center of a cell casing. The cell casing is then positioned inside an aluminum framework. Two stamps made of stainless steel function as current collectors and apply pressure to the pellet.The screw on top of the setup is used to regulate the pressure [34]

During electrochemical testing, the pressure on the ASSB pellet is normally in the range of 50 to 70 MPa, which may be modified using the screw. After cell cycling, the apparatus may be disassembled and the pellet can be recovered since the current collector can be easily removed and the electrode surface is readily accessible for additional analytical analyses. However, only the microstructure of the CAM and the modification of its surface prior to cell cycling must be taken into account when evaluating the outcomes of this thesis. Due to the relatively high pressures applied during cell cycling and the excellent malleability of the SE (low Young's modulus), the cathode composite surface is reasonably smooth at the start of the subsequent experiments [35, 36].

1.3.1 Inorganic Solid Electrolyte for ASSBs

Ionically conductive inorganic SEs (> 1 mS.cm^{-1}) are the essential component of ASSBs, which eliminates the safety problems inherent in traditional LIBs. Inorganic SEs also have high thermal stability and conductivities across a broader temperature range from -10 to 100 °C, where traditional liquid electrolytes will freeze, boil, or decompose [37]. To achieve the potential of ASSBs, a variety of innovative SE materials have been discovered and studied to satisfy many essential characteristics, including high Li ion conductivity, low electronic conductivity, and excellent chemical and electrochemical stability against Li metal and cathode/anode active materials [38]. In terms of practical use, they should be economical, non-toxic, and ecologically benign [39]. Numerous inorganic SEs have been identified and studied in the past, including oxides and phosphates SEs: LISICON-type $Li_{14}Zn(GeO_4)_4$ (LZGO), perovskite-type $Li_{3x}La_{2/3-x}TiO_3$ (LLTO), NASICON-type $Li_{1.07}Al_{0.69}Ti_{1.46}(PO_4)_3$ (LATP) and $Li_{1.5}Al_{0.5}Ge_{1.5}(PO_4)_3$ (LAGP), thiophosphates (sulfides). Sulfide SEs: glassy sulfides, thio-LISICON-type binary/trinary sulfides. LGPS-types: $Li_{10}MP_2S_{12}$ (M=Ge, Sn). Chloride SEs: binary/ternary LiCl-M_xCl_y and derivatives [32, 38, 40]. And currently, Li-argyrodite $Li_{7+x-y}M^V{}_{1-x}M^{IV}{}_xCh_{6-y}X_y$ or Li_6PS_5CX (M^V = P, Sb; M^{IV} = Si, Ge, Sn; Ch = O, S, Se; X = Cl, Br, I, BH_4; $0 \leq x \leq 1$; $0 \leq y \leq 2$) SEs are the predominant SEs used for the fabrication of ASSB [41, 42, 43, 44, 45, 46, 47, 48, 49, 50, 51, 52], which this thesis focuses on. Due to their high Li ion conductivity, Li_6PS_5CX are attractive for the development of ASSB (up to 24 mS.cm^{-1}, the highest values reported to date [53]) and scalable solution-assisted synthetic process, both of which are essential for commercial applications [54]. The structure of argyrodite is derived from the mineral Ag_8GeS_6 (orthorhombic, S. G.: $Pna2_1$). Depending on their chemical composition, Li-argyrodites display two structural polymorphs with distinct phase transition temperatures [55]. Compounds that crystallize in the low-temperature orthorhombic structure, such as Li_7PS_6 (S. G.: Pna21), exhibit very poor Li ion conductivity at ambient temperature, while high ionic conductivities have only been attained in the high-temperature cubic phase (S. G.: F43m). By substituting one or more sulfide anions with halide anions, the cubic structure is stabilized at room temperature, resulting in Li_6PS_5X (X = Cl, Br, I) [44]. Depending on the composition of Li_6PS_5X, S^{2-}/X^- anion site disorder has been found to varying degrees [42]. As a result of a substantially bigger ionic size difference between I^- and S^{2-} in Li_6PS_5I, both stay on their two distinct crystallographic sites, while in Li_6PS_5Cl, Cl^- and S^{2-} exhibit a major site disorder [42]. Anion-ordered Li_6PS_5I has a negligible Li ion conductivity, but anion-disordered Li_6PS_5Cl has a significant Li ion conductivity. Figure 1.4 depicts the crystal structure of SEs utilized in this thesis.

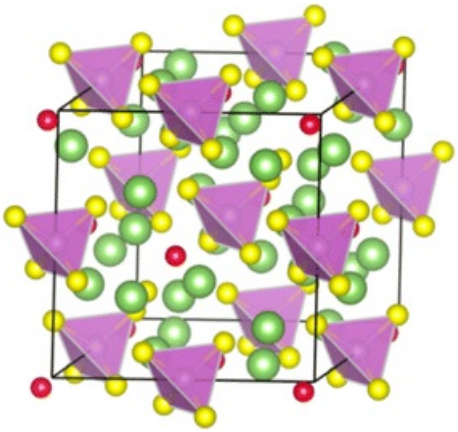

Figure 1.4: Crystalline structure of Li_6PS_5Cl. Li^+: green, Cl^-: red, S^{2-}: yellow, and $(PS4)^{3-}$ tetrahedron: purple [56].

1.3.2 Cathodes and Cathode Active Materials for ASSBs

As indicated in Section 1.2, cathode active material (CAM) in its lithiated form is the primary component of LIB and this is also the primary component of ASSBs as present in a discharged cell. In its delithiated state, while the cell is being charged, it is the sole cell component contributing to energy storage (along with a hypothetical in situ lithium-plated anode generated during charging), making it the material that must be present in significant quantities for a high-performance cell [57]. All other components, which may be required for large scale processing, only decrease the specific energy of the cell and are, therefore, engineered to minimize their content without affecting the function of the cell [57]. The kind and amount of CAM in a cell ultimately define the greatest specific energy that the system can produce. CAM also contributes significantly to the total cost of the cell, necessitating constant optimization toward lower costs and greater energy density [58]. Until now, CAM development has focused mostly on performance optimization using liquid electrolytes in LIBs. The issues of cathode electrolyte interface (CEI) development [59], cracking of CAM particles [60], transition metal dissolving [61], and HF scavenging [62] have been discovered and intensively investigated, and rational materials design has made it possible to solve them [63]. This led to the development of current state-of-the-art CAMs for NMC. However, a move from LIBs to ASSBs is accompanied by distinct needs for CAMs, which stem from the different properties of SEs. The manufacturing of high-performance ASSB cathodes offers difficulties on many length ranges, spanning from the micro- to the nano-scale, which are associated with the composite cathode, CAM particles, and interface between CAM and SE, respectively [59, 62, 64, 65]. Figure 1.5 represents the important processes occurring on different length scales in SSB cathodes, causing various challenges to the development of scalable fabrication processes and tailored materials properties. In addition to microscale optimization of composite cathodes, the CAM must be engineered for ulization in ASSBs to be mechanically compatible with the SE [66, 31]. To attain high performance ASSBs, the following challenges posed by cathodes must be overcome.

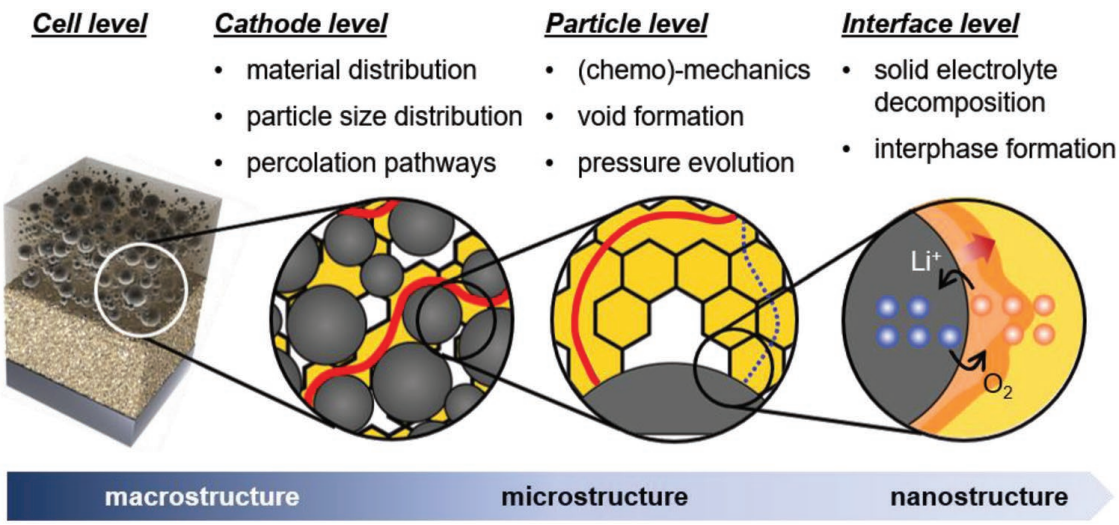

Figure 1.5: Schematic overview of the processes on three length scales cathodes which could cause challenges to the development of ASSBs [57]

I. Cathode Microstructure and Charge Transport

ASSB cathodes must have high ionic and electronic partial conductivities as well as a high loading of CAM in order to keep within a few tens of $\Omega\ cm^2$ of internal cell resistance and optimize both energy and power density [33]. Nevertheless, there is often a trade-off between optimum energy and power, which requires careful balance of CAM volume fraction and electrode thickness. A lower SE concentration increases the tortuosity of ionic conduction pathways and restricts the power density that may be achieved [67, 68, 69, 70, 34]. Sandvik et al. [71] studied composite cathode loadings of CAM, SE, and carbon additives with the ratio of 11:16:1 to offer high energy density.

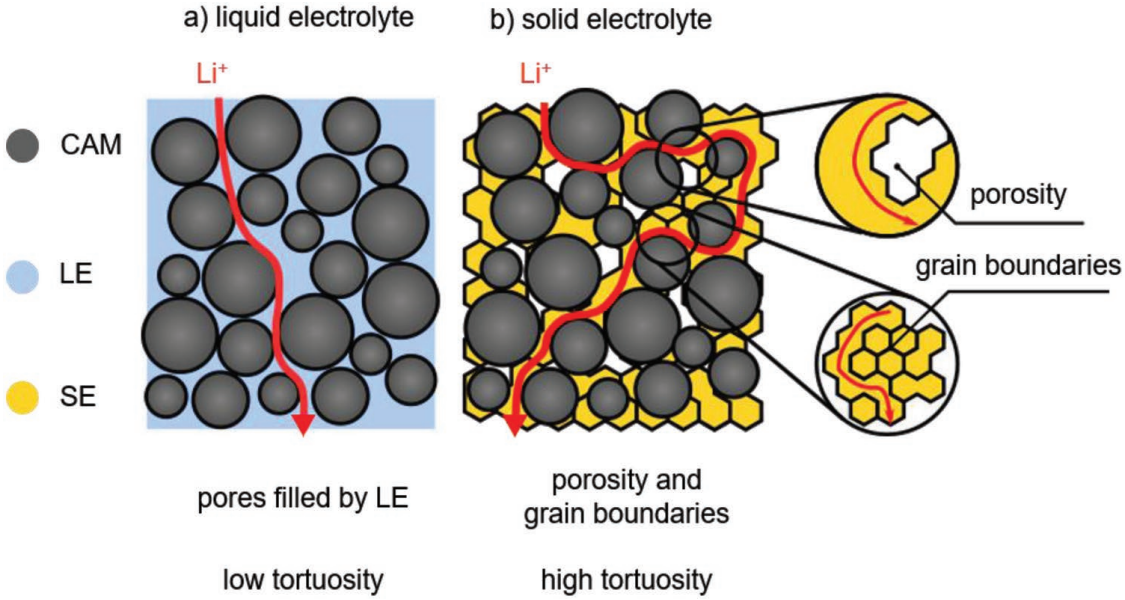

Figure 1.6: Comparison of composite cathodes using a a) liquid- or b) solid-electrolyte. A LE can infiltrate the cathode and penetrate pores, resulting in a homogeneous distribution of charge transport pathways and minimal ion transport tortuosity. In the case of SE, residual porosity and grain boundary resistances provide much more tortuous transport pathways and a higher overall tortuosity. Red lines indicate the interface between electroyte and CAM [57].

In contrast to LIB cathodes, ASSB cathodes should have porosity which is shown in Figure 1.6 as

minimal as possible since pores are neither electronically nor ionically conductive and adversely impact charge transport [72]. Pores hinder active interface between SE and CAM and a significant increase in overvoltage could be predicted by surface coverage, pore size, and distribution models [73]. As a result, this could impair the capacity to provide electrons and ions to all areas of the cathode, which is a necessary prerequisite for the fabrication of high-performance composite cathodes. In contrast to LEs, SEs have their own microstructure, consisting of bulk and grain boundaries, which may result in ill-defined and non-uniform microscale transport features [73]. Poorly conducting grain boundaries may raise the "apparent tortuosity" of the ionic transport over and beyond the "geometric tortuosity", which solely examines the distribution of phases [57].

II. Chemo-Mechanics during Electrochemical Cycling

As all elements of inorganic SSBs are solids and are often constrained by volume in the cell housing, (electro-)chemically induced volume or shape changes during cycling have a significant impact on the cell performance and degradation [69]. Volume and morphology changes at the cathode rely on (de-)lithiation and the state of charge (SOC) [57]. Figure 1.7 represents how (chemo-)mechanical effects create cracking and volume change in CAM by replacing an LE with a SE.

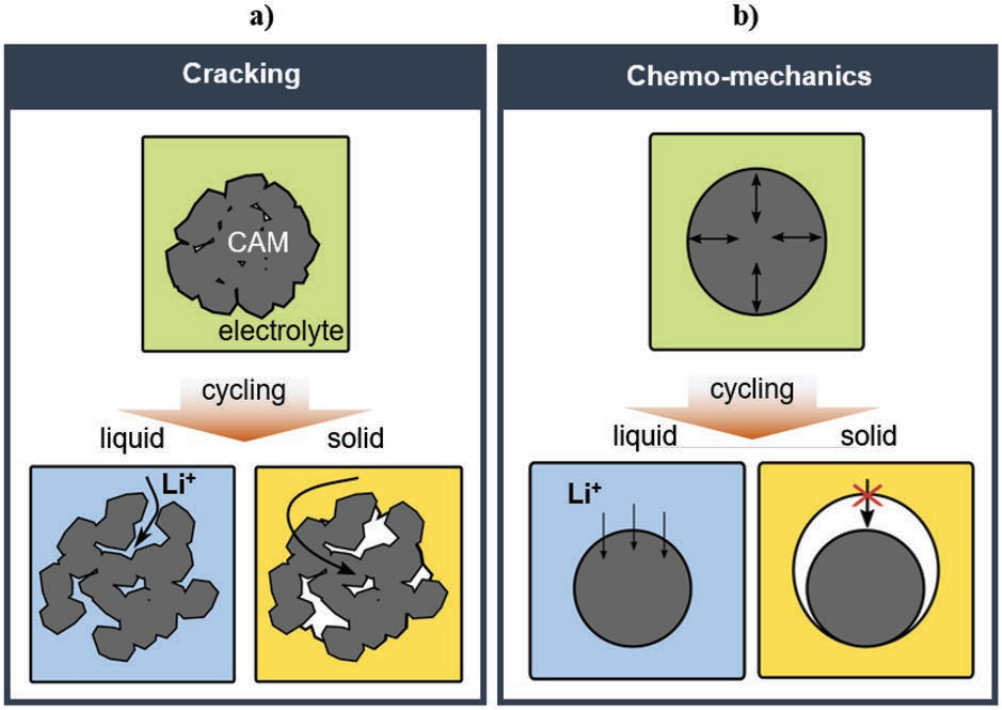

Figure 1.7: Schematic depiction of the consequences of transforming a liquid electrolyte into a solid electrolyte. a) Cracking of CAMs generated by (chemo-)mechanical stress reduces transport pathways for liquid electrolytes because they may enter the newly created pores. In the case of a solid electrolyte, the length of the transport pathways is extended. b) Large fluctuations in volume lead to contact loss between CAM and SE and higher interface resistances.

Whereas conventional intercalation- or insertion-type CAMs undergo volume changes in the range of several percent while retaining their original crystal structure, conversion-type CAMs can undergo volume changes of up to hundreds of percent as well as morphology changes due to the electrochemical conversion reaction [57]. The combination of thiophosphate-based SE (LPSCl) and Ni-rich NCM CAM is highly attractive. This is due to the high ionic conductivity combined with their malleability (low Young's modulus), which enables them to accommodate (electro-) chemically induced volume changes during battery operation [74].

Additionally, it may be expected that internal stress/strain creation in the cathode might result in the SE matrix cracking [57]. This has a negative impact on the ionic and electronic percolation

pathways, resulting in poor electrochemical reversibility and capacity fading owing to lack of contact with CAM during continuous cycling. As shown in Figure 1.7a), LEs can enter these pores and cracks, but SEs are inflexible and unable to do so. In order to compensated these effect, external pressures were applied to ASSBs during cycling, the detail experimental setup will be shown and discussed in Section 2.5.

III. Interfacial Compatibility

The low chemical potential of lithium in the utilized CAMs leads to oxidation of the SE. During oxidation, ionically weakly conducting phases are produced, which in the case of thiophosphate-based SEs are polysulfides [69]. These reaction products impede the charge transfer by narrowing transport pathways resulting in increased interfacial resistance and poor cycling performance as depicted in Figure 1.8b) [65, 75, 76]. Therefore surface engineered CAM are desirable to inhibit SE oxidation (Figure 1.8a).

The fundamental role of a surface modification is to serve as an electron-blocking and lithium-ion conducting layer, so that the SE is not exposed to the low chemical potential of lithium in the CAM . In addition, to allow (de-)lithiation of the CAM, it is important that adequate electrical transmission via the protective covering between the particles must be achieved. Moreover, if the coating is excessively brittle, it may lose contact with the CAM during cycling owing to the accompanying volume or morphology changes. Finally, the application of a surface coating creates additional interfaces, particularly SE/coating and CAM/coating interfaces, which may have negative impacts on the charge-transport properties of the composite cathode For all of these aforementioned reasons, it is necessary to optimize the coverage and morphology in order to maintain percolation. From now on, the fundamentals, experiments, and outcomes of CAM coating will command attention in this thesis.

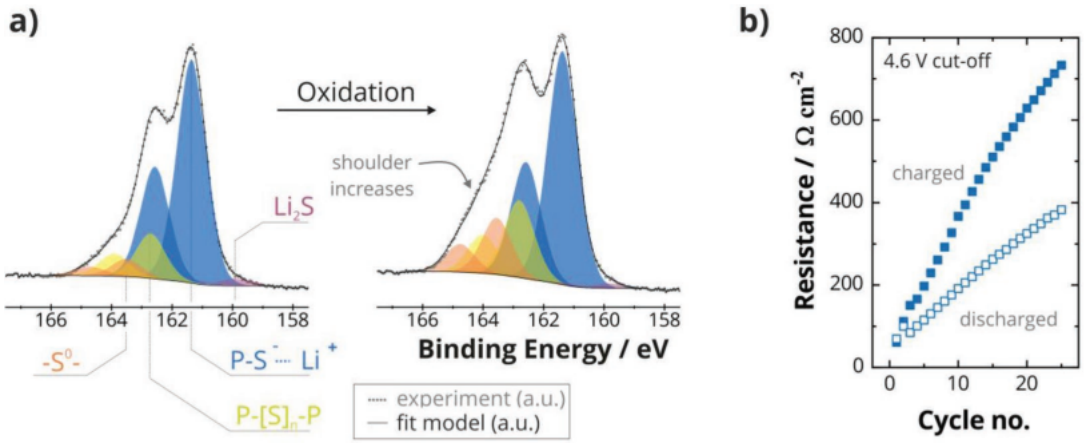

Figure 1.8: a) Before and after exposure to positive (oxidizing) potentials, X-ray photoelectron spectroscopy studies were performed on β-Li_3PS_4. The shoulder at higher binding energies rises dramatically, suggesting thiophosphate-based SE oxidation. b) Evolution of the interfacial resistance between uncoated NCM and a thiophosphate SE, illustrating the increase in resistance with increasing cycle number due to electrolyte degradation by the uncoated cathode [65].

1.3.3 Anode and Indium-Lithium Electrode for ASSBs

Due to its ultrahigh theoretical capacity (3860 mAh/g), lowest redox potential (-3.04 V compared to the conventional hydrogen electrode), and low density, lithium metal is a particularly attractive anode material for lithium metal batteries [77].

As discussed before, the chemical stability of solid electrolytes against the cathode electrode is a major challenge. This is also the case at the Li-SE interface of the anode, where a number of

experimental observations suggest that physical contact between lithium metal and thiophosphate-based SEs results in the creation of Li_3P, Li_2S, and other byproducts [78, 79].

Utilizing lithium alloys as opposed to lithium metal is a promising strategy for achieving a more stable anode electrode/solid electrolyte interface that permits long-term cycling of solid state batteries. Especially lithium intermetallic phases containing Al, Ga, In, Sn or Sb can possess even larger chemical diffusion coefficients when compared with the Li-self diffusion [80]. Lithium alloys are easily synthesized via solid-state diffusion at ambient temperature. Typically, lithium insertion into metals (alloy formation) happens at potentials below 1 V vs. Li+/Li. This remains below the threshold for thiophosphate electrolytes [81]. However, compared to lithium metal, the thermodynamic driving force for electrolyte reduction is reduced. The introduction of an alloy in place of Li metal in anode would further mitigate the problem of dendrite growth, hence eliminating the danger of short circuiting. In spite of the possibility of dendrite growth, it is important to note that the interfaces between Li and some solid electrolytes can be "stable." Ma et al. found in the case of cubic $Li_{7-3x}Al_xLa_3Zr_2O_{12}$ SE, ultra thin interphase occurs in direct contact with lithium [82].

The lithium-indium (Li-In) system stands out among lithium alloys because of its high ductility and constant redox potential of about 0.6 V vs. Li^+/Li (0.5 V at 415℃) [83] over a wide stoichiometry range [84, 85]. The high cost of indium impedes any large-scale application; however, the use of Li-In alloys as the counter electrode facilitates the assembly of ASSBs, enabling electrochemical investigations on CAM and SE on the lab scale.

1.4 CAM Coatings for ASSBs

The inclusion of a protective coating layer must be investigated in order to overcome the cathode challenges for ASSBs. As mentioned above, in the absence of a protective coating layer, thiophosphate-based SEs will inevitably oxidize at high potentials as well as state-of-the-art CAMs undergo significant volume changes during lithium (de) intercalation. The existence of coating layers replaces the original SE/CAM interface by the SE/coating and the coating/CAM interfaces. The coating of CAM has been studied for LIBs, which are similar to ASSBs in many ways. However CAM coating for LIBs are often designed to be electronically conductive so as to maintain a percolating network; remove unwanted surface functional groups; act as an HF scavenger and reduce the acidity of the liquid electrolyte; prevent transition metal dissolution from the cathode into the liquid electrolyte; and provide physical protection against side reactions that decompose the liquid electrolyte [86, 87]. On the other hand. the fundamental role of surface coating materials for the CAM–SE interface is to function as a lithium ion conducting and an oxidation-stable solid electrolyte. Therefore, the major focus of this thesis is on coating materials containing lithium as a principal and suitably mobile cation. In addition, because redox reactions involving the SE must be avoided, the coating must be a poor electronic conductor so that the SE does not experience the low chemical potential of lithium in the CAM, or so that a sufficient gradient of the chemical potential of lithium is formed across the coating [88]. Sulfur in LPSCl will be oxidized at around 2.3 V relative to Li^+/Li [89]. As so, the sulfur is redox-stabilized by the P(+5) by several hundred millivolts, as contrasted to the pure sulfur redox system in lithium–sulfur cells. As the lower cut-off potential during cycling of NCM-containing ASSBs is commonly set at values greater than 2.3 V, the cathode may thermodynamically oxidize the SE in any state of charge. Therefore, we must look for materials that exhibit no redox activity in the potential range of 2.38 V to 3.68 V that this thesis investigates.

On the cathode side, oxides have the benefit of being quite stable. However, electron-hole formation may occur at high potentials, and oxygen redox reactions are a crucial aspect of cathode electrochemistry. The energy of the 2p orbitals of oxygen anions in oxides is dependent on the cation environment, and the formation of complex oxo-anions may reduce the 2p states to such a degree that oxidation can only occur at high potentials. When oxygen under the redox reaction, it correlates chemically to the formation of "O" in the lattice and may result in the formation of peroxide species. This corresponds, on an electronic level, to the formation of electrons that may result in electronic conductivity.

To ensure electrical percolation via the cathode composite, the CAM particles must be in direct contact with one another, or at the very least connected by percolated carbon networks [90]. Therefore, complete covering of the CAM particles with an electrically insulating coating substance would render the electrode unusable. One method would be to modify the coating coverage to allow for regions of direct contact with the CAM particles; however, this would also expose regions to SE decomposition. Assuming that the CAM particles are uniformly covered with a protective layer, contact must be established during electrode processing. For instance, the coating may fracture during mechanical mixing with the SE or electrode compression. Figure 1.9 a) is a schematic displaying two possible compression situations involving two coated CAM particles.

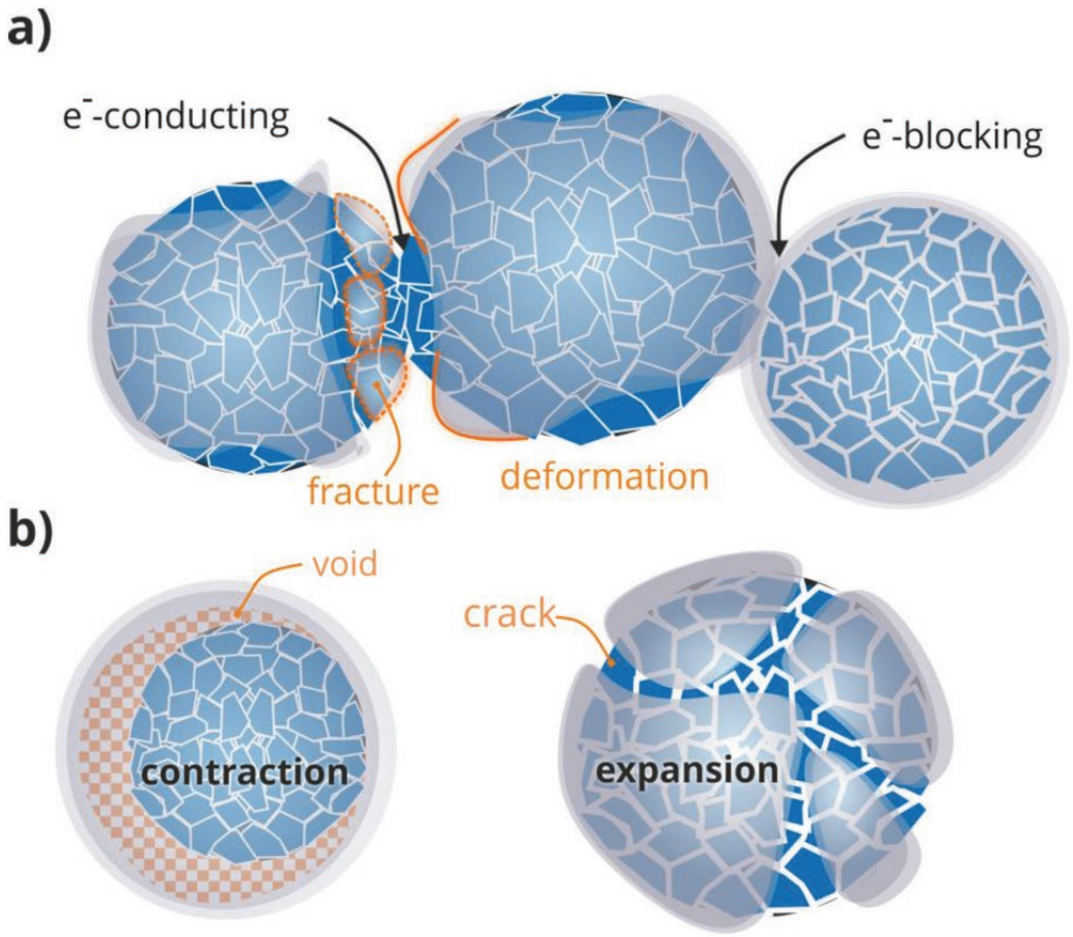

Figure 1.9: a) the potential processing scenarios for achieving electrical contact between coated CAM particles. b) impact of volumetric changes in the material of the electrode on the coating

Due to the volumetric strain during lithium (de)intercalation, the expansion or contraction of CAMs must be restrained or, more likely, accommodated by the coating layer. Consequently, the coating material will determine the strain of the CAM and may prevent cracking. If not, the coating might delaminate from the CAM material during contraction or split during expansion owing to the increase in surface area Figure 1.9 b). As previously stated, CAM volume change during cell cycling, are unfavorable to ASSB performance, however, a coating may minimize lithium-induced strain by constraining the CAM structure. In spite of this, there is still considerable controversy around this topic. A simple calculation reveals that a change in surface energy caused by a coating of 1 J m^{-2} for the CAM results in a cohesive pressure that is about 2 bar for a particle that has a diameter of 10 µm [90]. Because of this, a coating that is just a few nanometers thick will not be able to contain the volume changes that are caused by CAM materials. The chemical expansion of CAMs cannot be regulated by a coating; however, the consequences of this expansion may be affected by a coating. It has previously been shown that coatings have the ability to prevent the development of mechanical cracks in CAMs that are caused by volumetric strain [91].

Once solids come into contact with one another, interdiffusion will always take place, and the degree to which it happens will be determined by the degree to which the two solids' constituents are mutually soluble as well as the diffusion coefficients of the mobile components. It is more likely to take place during high-temperature processing or electrochemical cycling since diffusion in ionic solids is extremely sluggish under ambient circumstances (at least for multivalent ions) [90]. During the electrochemical cycling of ASSBs with high voltage cathodes and thiophosphate SEs, it is known that a significant quantity of interdiffusion takes place [92, 93] as shown in Figure 2.11 a). But adding an interlayer can cut down on this interdiffusion, stopping the breakdown and stopping the formation of resistive interphases as shown in Figure 2.11 b) [94]. In general, the presence of a protective interlayer between the CAM and the SE reduces the formation of an interfacial layer and inhibits Co diffusion into the SE. [90].

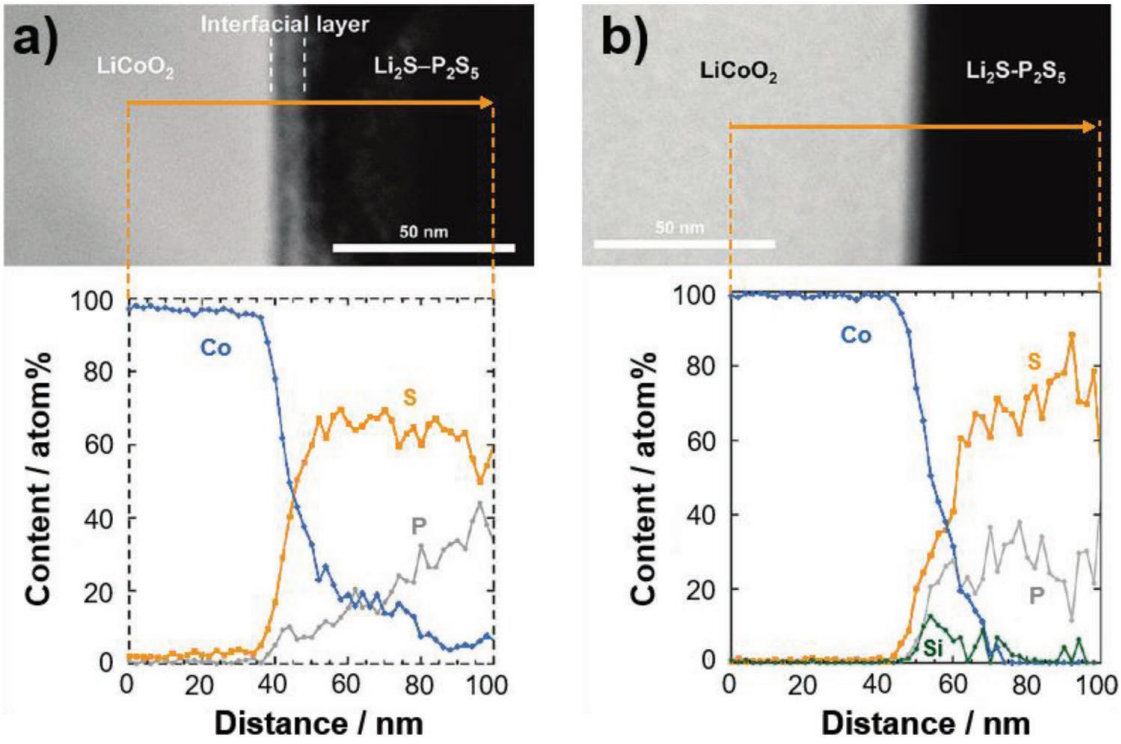

Figure 1.10: Cross-sectional scanning transmission electron microscopy images of the $LiCoO_2/Li_2S–P_2S_5$ interface a) without and b) with a Li_2SiO_3 layer that has been accumulated following the initial charge. Moreover, cross-sectional energy dispersive X-ray spectroscopy line profiles across the $LiCoO_2/Li_2S–P_2S_5$ interface c) without and d) with a Li_2SiO_3 coating were measured [94].

Solid-state side reactions between the coating and the CAM must also be avoided, since their products are often interphases with low conductivity that increase the impedance of the interphase/interface. However, in certain instances, interdiffusion between the CAM and the coating may improve the CAM's overall stability [95]. After 300 cycles, the $LiNbO_3$-coated LCO in Figure 1.11 reveals evidence of Co diffusion from the LCO into the $LiNbO_3$ coating layer [96].

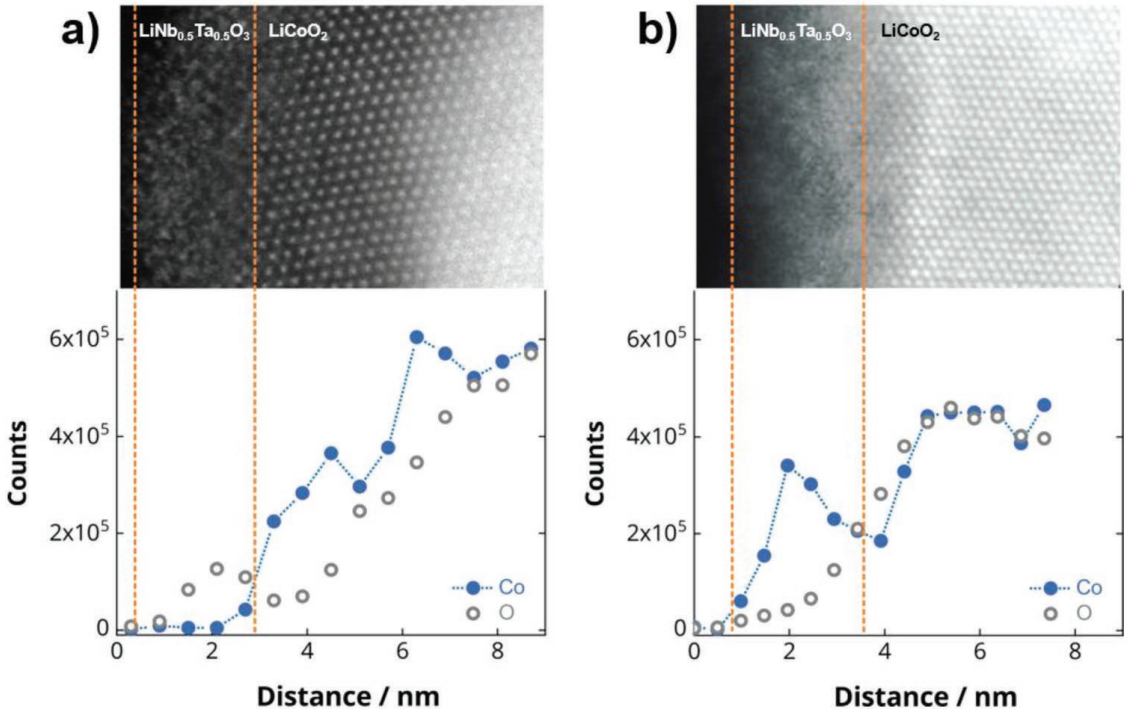

Figure 1.11: High-resolution STEM images and corresponding electron energy loss spectroscopy line scans of a LiNbO3-coated LCO particle a) before and b) after 300 cycles [96].

In conclusion, the ideal coating material (Figure 1.12) will behave like a SE with low electronic partial conductivity (low redox activity of the cation(s)), be sufficiently brittle to allow direct contact of CAM particles by mechanical deformation, and be sufficiently elastic to reduce strain during volume changes of the CAM particles.

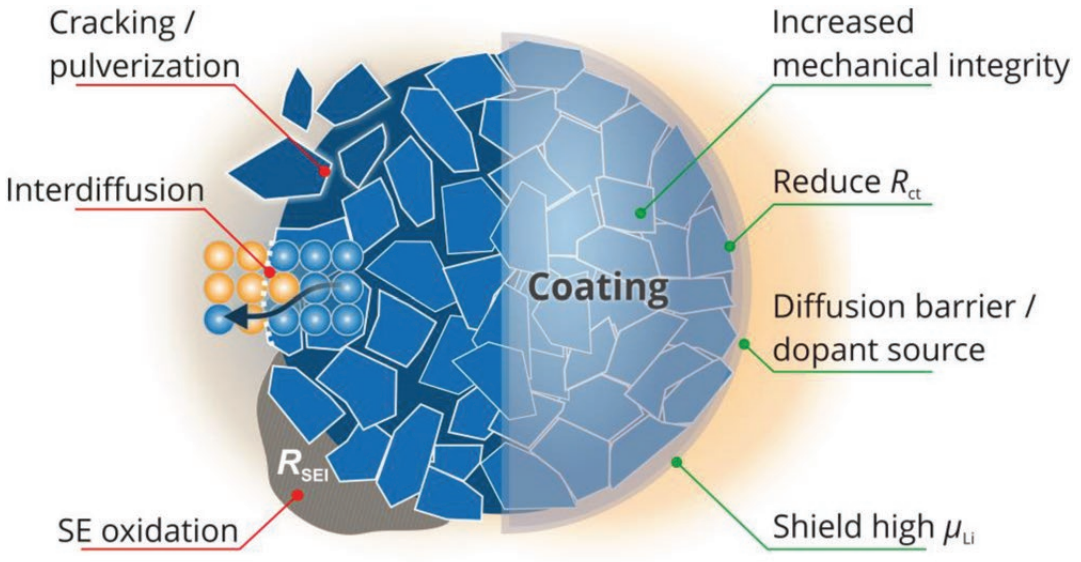

Figure 1.12: The primary challenges that arise at the interface between the cathode and solid electrolyte during battery operation, as well as the advantages of using an appropriate cathode coating [90].

1.4.1 Classes of CAM coatings and Lithium Ion Conductors

The relevant properties of bulk crystalline solids (e.g., ionic and electronic conductivities) are often utilized to identify potential coating materials; yet, coatings are typically amorphous. Therefore, the properties of amorphous coatings will undoubtedly vary from those of their crystalline counterparts. As an example, amorphous oxides have a lower electronic conductivity than their crystalline counterparts, which is a favorable characteristic. On the one hand, amorphous materials are often less conductive than their highly conductive crystalline counterparts in terms of lithium-ion conductivity [97]. In contrast, crystalline ionic conductors with poor conductivity may display higher ionic conductivity in an amorphous phase [98, 99, 100]. Despite the contrast between crystalline and amorphous coating qualities, the vast majority of commonly used coatings have adequate ionic conductivities, and if the coating is sufficiently thin, even a low conductivity may suffice. For instance, an area specific resistance of 1 cm^2 would need a minimum ionic conductivity of 0.5 µS cm^{-1} [90]. So, any coating material with the same level of ionic conductivity as a poorly conducting LiPON film should work, as long as the interface between the CAM and the coating doesn't slow down the process.

Binary Oxides

A lot of research has been done on binary oxides such as ZrO_2, $Al2O_3$, TiO_2, and SiO_2 as CAM coatings in LIBs to improve cycle life, rate capability, and thermal stability by stopping liquid electrolyte degradation. Cho et al. also reported that LCO in LIBs has different binary coatings and that a thin 10 nm ZrO_2 film can completely stop the volume expansion of LCO [101]. However, Chen and Dahn showed that the changes in volume were not stopped, and that the improvement in the electrochemical properties was probably due to the protective nature of the ZrO_2 coating [102]. In SSB cells, binary oxides, such as ZrO_2, have either not been used or have been utilized with little effectiveness. In typical LIBs, the liquid electrolyte may diffuse into the tiny pores of a coating layer, providing for enough ionic conductivity. This is not achievable in the SE environment, but it is possible for a binary coating to react with Li_2O, LiOH, or $LiCO_3$ to produce a ternary Li-ion conducting coating or get lithiated in situ during electrochemical cycling. The quantity of Li-containing contaminants on the surface of the CAM is variable and difficult to regulate, therefore the low reproducibility of this method becomes a practical issue [90].

Ternary Oxides (Lithium Ion Conductors)

For solid-state batteries comprising Li_2S–P_2S_5 glasses or $Li_{4-k}Ge_{1-k}P_kS_4$ solid electrolytes, predominantly $Li_4Ti_5O_{12}$ and $LiNbO_3$ buffer layers have been used to encapsulate $LiCoO_2$. These coating layer were used for reducing interfacial resistance, avoiding SE deterioration, and improving the battery's specific capacity, rate capability, and cycle life. Whereas the vast majority of previous research on CAM coatings was conducted using cells containing Li_2S–P_2S_5 glasses and $Li_{4-k}Ge_{1-k}P_kS_4$ SEs, several reports have utilized Li_6PS_5Cl.

It has been widely reported that LZO is a suitable choice for high-temperature CO_2 adsorption [103, 104, 105]. But due to its combination of thermal, chemical, and electrochemical stability, LZO has also recently gained a great deal of interest as a coating material for modifying cathodes in LIBs [106]. Song et al. discovered that when LZO was coated on the surface of $LiNi_{0.7}Co_{0.15}Mn_{0.15}O_2$, the LZO coating layer protected the cathode interface by reducing the corrosion reaction with electrolyte during the charge and discharge process. And the 3 wt% LZO-coated cathode retained 92.8% of its discharge capacity after 100 cycles, whereas the uncoated $LiNi_{0.7}Co_{0.15}Mn_{0.15}O_2$ had the discharge capacity of just 82.8% [107]. Liang et al. have also synthesized varied concentrations of LZO-coated NMC811 using the sol–gel technique. Cathodes coated with LZO demonstrated higher cycle stability and rate performance in comparison to uncoated cathodes [108]. Chen et al. discovered a technique that enables the production of a uniform LZO coating on NMC811; this coating considerably enhances the capacity retention of cathode composite to 98.3% (300 cycles at 1 C) [109]. Furthermore, crystalline LZO formed on the surface of the coating layer may provide tunnels for lithium ion movement during the charge and discharge process [110]. In addition,

a portion of the Zr enters the crystal lattice, expanding the interplanar gap and enhancing the layered structure's stability [111], mitigating Li/Ni cation mixing [112, 113] and phase transition [114], minimizing oxygen vacancies and optimizing microstructure [115, 116, 114]. Yang et al. discovered that the ordered occupancy of Ni in the Li slab with less Li/Ni mixing is induced by the LZO coating, Figure 1.13 is evidenced by super lattice diffraction peaks of (20–1) and (202) [114].

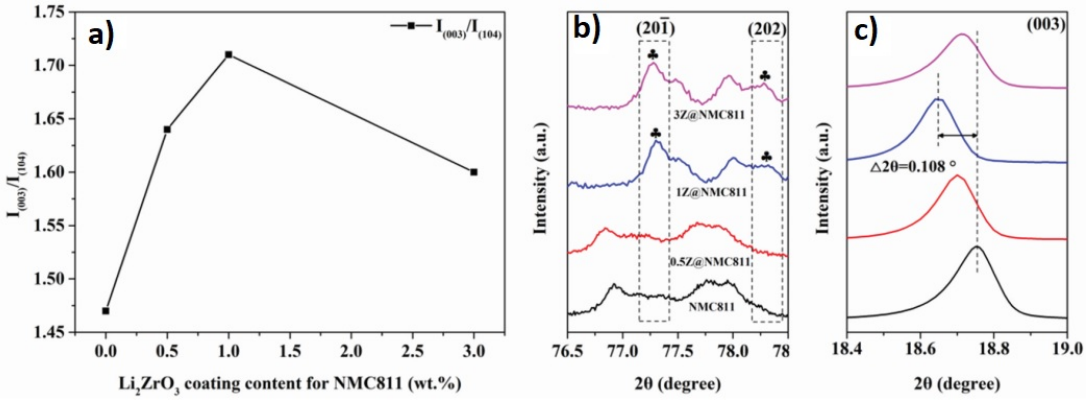

Figure 1.13: a) Variation of the I(003)/I(104) with different LZO content for NMC811. b) Superlattice diffraction peaks of ordered occupancy of Ni in Li slab. c) Enlarged region of the (003) peaks [114].

Yang et al. has compared the pristine NMC811 and the transition metal slab shrinks while the Li slab expands after LZO coating. The reduced Li/ Ni mixing, ordered Ni occupancy in Li slab as well as expansion of Li slab give rise to greatly enhanced Li ions' diffusivity [114].

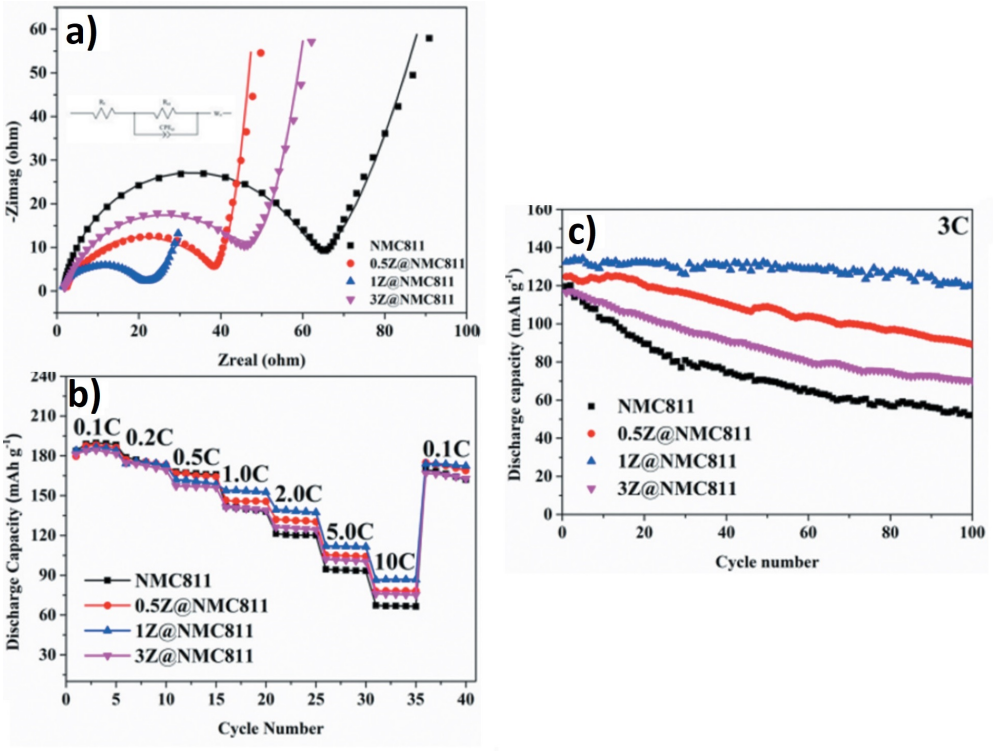

Figure 1.14: Nyquist plot of a) pristine NMC811, 0.5 wt% LZO-coated NMC811, 1 wt% LZO-coated, 3 wt% LZO-coated NMC811, b) rate performances, c) cycling performance at 3 C [114].

Electrochemical impedance spectrum (EIS) measurement (Figure 1.14 a) clearly demonstrate the

conductivity difference of LZO coating content. The semicircle landing on the real axis at medium frequency is directly related to the charge transfer resistance (Rct), whereas the linear component at low frequency is due to the diffusion of Li ions [117]. The pristine NMC811 exhibits the highest Rct and the lowest Li ions' diffusivity, while the 1 wt% LZO-coated NMC811 samples exhibit the greatest improvement in both Rct and Li ions' diffusivity. The rate capability of each cathode is compared in Figure 1.14 b). Each was initially charged at 0.1 C before being discharged at various rates. At low discharge rates between 0.1 and 0.5 C, the pristine NMC811 and 0.5 wt% LZO-coated NMC811 samples are able to give the highest capacity. When the current density exceeds 1 C, the 1 wt% LZO-coated NMC811 samples offer the highest capacity, indicating that conductivity largely dictates the possible capacity at high rates. Figure 1.14 c) compares cycling performance at 3 C. Under high rate charge/discharge, the pristine NMC811 can release a maximum of 120 $mAhg^{-1}$ and then quickly degrades in subsequent cycles, retaining just 43.9% of its capacity after 100 cycles. At 3 C cycling, the conductivity advantage and decreased surface reactivity of the LZO-coated NMC811 provide improved performance. The 1 wt% LZO-coated NMC811 samples have an initial capacity of 130 $mAhg^{-1}$ and retains 92% of its original capacity after 100 cycles. In general, LZO coating for CAMs will result in a LIB with lower interfacial resistance, often resulting in an improvement in initial discharge capacity, enhanced high rate capability, and enhanced capacity retention compared to a LIB with an uncoated CAM.

1.5 Nucleation of LZO coating layer

Top-down and bottom-up synthesis approaches Figure 1.15 have facilitated the integration of customized nanomaterials into multifunctional devices, allowing for a wide variety of applications. First, the 'top-down' technique is a high-energy synthesis process that includes breaking down a bigger dimension into smaller particles until the desired size and shape is achieved, or initiating reactions in a mixture by applying tremendous mechanical forces [118]. Despite the fact that the particles synthesized by this approach have a broad size distribution and a range of morphologies, this kind of synthesis is most usually used to produce ceramic materials for which these features are not essential [118]. The example of 'Top-down' synthesis for the production of LZO nanoparticles is the destruction of the crystal lattice of the precursors by means of high-energy ball milling [119].

"Bottom-up" self-assembly of atoms and molecules is the alternative that will be the primary emphasis of this thesis. This approach is based on a chemical reaction in which a reduction in solution is followed by the precipitation, formation, and stabilization of nanoparticles. [120]. The optimized process, according to this methodology, can result in no waste of precursor materials or the elimination of parts from end products, as opposed to the 'top-down' approach. Nanoparticles with fewer flaws are produced, resulting in a more consistent size and shape distribution as well as a more homogeneous chemical composition[118].

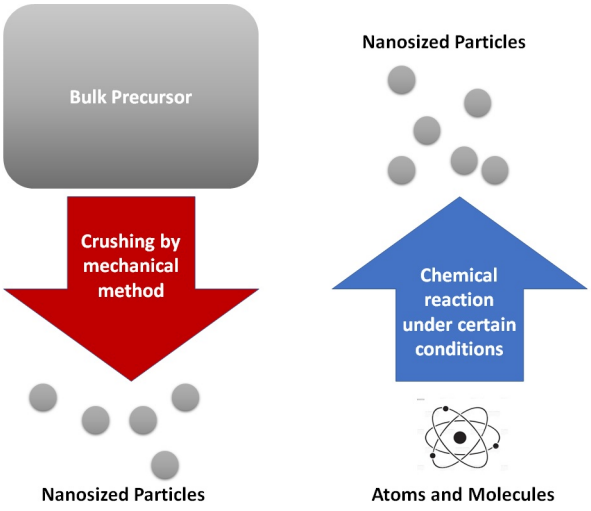

Figure 1.15: Bottom-Up and Top-Down Approaches for nanoparticles synthesis

The most commonly used ”bottom up” synthesis of lithium zirconium oxides is via "Sol-Gel" method. Using zirconium precursor such as $Zr(NO_3)_4{\cdot}5H_2O$, $ZrO(NO_3)_2.6H_2O$; lithium precursor such as $LiCH_3COO{\cdot}2H_2O$, $LiNO_3$ to synthesize LZO. Kang et al. [121] proposed a possible mechanism when ZrO^{2+} and Li^+ are added to an aqueous solution, such as water or 100% ethanol, the polar groups present in these solutions interact with ZrO^{2+} and Li^+ to form heterogeneous nucleation sites. These numerous polar groups make hydrogels form and act as nanoreactor to template and stabilize nanocrystal containing Zr and Li elements. When the precursor is annealed, it converts into LZO nanoparticles. Due to the very high surface energy of nanocrystals, the precursor to LZO may be transformed at a relatively low temperature.

1.6 Sol-gel Coating Methods

Depending on the coating technique, the electrochemical performance of the cathode material might vary greatly, indicating that the coating method itself has a considerable impact on the cathode properties [122, 86, 123]. The effect of coating method on cathode performance may be attributable to the following factors:

I. Variable coating methods may result in a different coating microstructure on the cathode surface, which can affect the Li^+ transport properties through the coating layer for the same coating material.

II. The method of coating might have an adverse effect on the cathode's surface structure. The surface of Ni-rich multilayer cathodes, for example, is very sensitive to water. If the coating method is water-assisted, the cathode's electrochemical performance might be significantly impacted.

In general, coating preparation must be simple, nondestructive against CAM particles, and cost-effective. The achieved coating layers should be thick enough to perform the "electron-blocking" and protective functions, but thin enough to prevent severe specific capacity losses due to ionic transport obstructions. Wet chemical techniques provide the least expensive and simplest paths to coated CAMs, since they may be undertaken on a workbench without the need for extra, costly equipment. The appropriate metal alkoxides required to achieve the desired oxide coating composition participate in a series of hydrolysis or alcoholysis and polycondensation reactions in the presence of water, initiating on the cathode particle surfaces which are dispersed in a prepared solution to form a homogeneous polymeric network of metal–oxygen bonds [124, 125, 126, 127, 128]. In order to acquire the appropriate morphology and crystallinity of the particle coating, the resulting products are then annealed at different temperatures. In comparison to other coating technologies, the sol-gel coating method offers chemical homogeneity of multi-component systems and a coating process that is simple to regulate [129]. However, it takes a considerable amount of time to finish the coating process. In addition, the microstructure and chemical properties of the coating layer may be strongly impacted by reaction conditions (concentration, temperature, water content, mixing time...), which can have a substantial impact on the cathode's electrochemical performance [129].

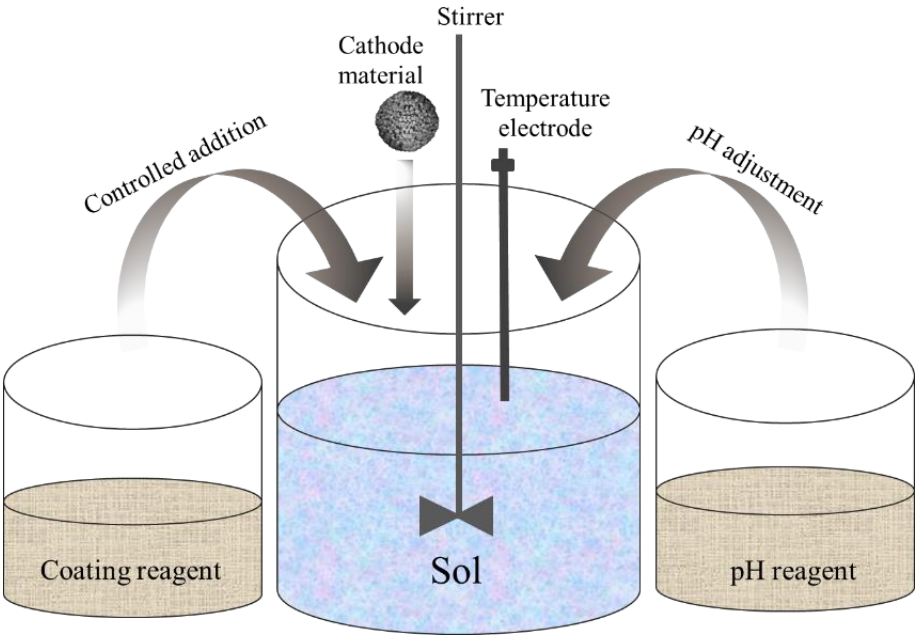

Figure 1.16: Schematic representation of the sol-gel coating method [130]

1.7 Aims of the Work

This thesis aims to develop an efficient coating process that not only enhances the electrochemical performance of NMC811, but also moves them one step closer to commercialisation. There are many coating methods that have been studied to date for the surface modification of NMC, such as the dry coating method as a top-down method, chemical vapor deposition (CDV) coating methods, and atomic layer deposition (ALD). However, the primary distinction between these approaches and the sol-gel methods is that the sol-gel methods can be used on an industrial scale. In addition, the sol-gel method makes it possible to make highly homogeneous composites with very high purity (99.99% purity). The lower temperature of this procedure, in comparison to other methods, might safeguard CAM from the side effects of crack formation during cycling.

Several coating materials for NCM-based cathodes have been studied. However, due to their various qualities, a standard coating material has not been determined. Coating materials based on LZO are recognized as among the most promising coating materials. The LZO coating layer might lower the degradation mechanisms and interfacial resistance of NMC811 and LPSCl, therefore protecting the LPSCl during cycling. Understanding the mechanism of the LZO coating process and the beneficial effects of the coatings on the electrochemical performance of NMC811-based cathodes is essential for the use of ASSBs. Figure 1.17 demonstrates the block diagram of proposed methodology for this study.

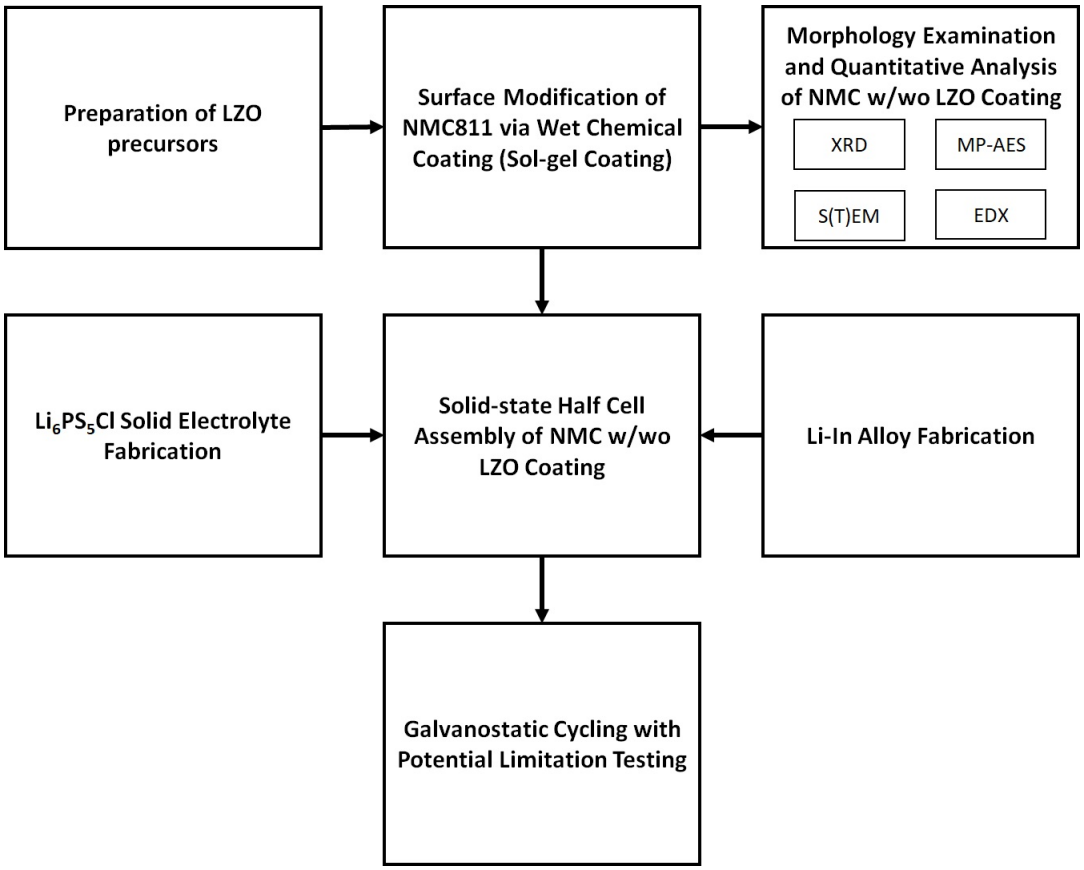

Figure 1.17: Block diagram of the proposed methodology

Chapter 2

Materials and Methods

This chapter describes in detail the methodology adopted to (1) develop surface coated cathode materials, (2) assemble solid-state half-cell battery and (3) perform physicochemical and electrochemical characterizations. The experimental part can be described using the aforementioned methodology Figure 1.17.

2.1 In Situ Surface Modification of NMC811 by LZO using Sol-gel Coating Method

To attain the ideal experimental conditions for varied coating thickness and crystallinity phase, three methods of in situ coating LZO on nickel-rich NMC811 cathode active materials were implemented.

2.1.1 Chemicals

Zirconium (IV) oxynitrate hydrate $\geq$ 99,0%($ZrO(NO_3)_2.6H_2O$, Sigma-Aldrich), lithium acetate dihydrate $\geq$ 99.0% ($CH_3COOLi{\cdot}2H_2O$, Thermo-Scientific), absolute ethanol (C_2H_5OH, VWR Chemicals), lithium nitrate 99.99% ($LiNO_3$, Sigma-Aldrich), commercial powdes of lithium nickel manganese cobalt oxide NMC811 with batch number SNMC03008 ($LiNi_{0.8}Co_{0.1}Mn_{0.1}O_2$, TARGRAY) were used in this thesis to develop the surface modified cathode for all-solid-state batteries. As received NMC811 powder was dried and stored inside Ar-filled glove box (O_2 and $H_20 < 0.1$ppm).

2.1.2 Apparatus

50 ml erlenmeyer flask, magnetic stirring bar, magnetic stirrer with heating LLG-uniSTIRRER 3 was provided by Lab Logistic Group, vacuum drying oven was provided by TMAXCN, muffle furnace was provided by Nabertherm, mortars and pestles, alumina crucibles, 20 ml volumetric of sample vials, LABmaster pro glove box workstation with powerful closed loop integrated gas purifier circulation was provided by MBRAUN,

2.1.3 Methods

In a series of studies, the optimal coating conditions for lithium ion conductors on NMC811 were determined. In this way, sol-gel coating experiments were performed in an improvised silicone oil bath with a 50-mL Erlenmeyer flask containing chemical reagents. The Erlenmeyer flask was submerged in silicone oil in a thick-walled Pyrex glass set on a hot plate inside fume hood, and

the temperature of the silicone oil was monitored using a thermometer to ensure that the temperature was maintained for the duration of the coating. To avoid contamination, the Erlenmeyer flask was completely covered, and the solution was constantly stirred with a magnetic stirrer to prevent particle agglomerations and maintain the solution homogeneity. Figure 2.1 demonstrates a schematic of the experimental set up.

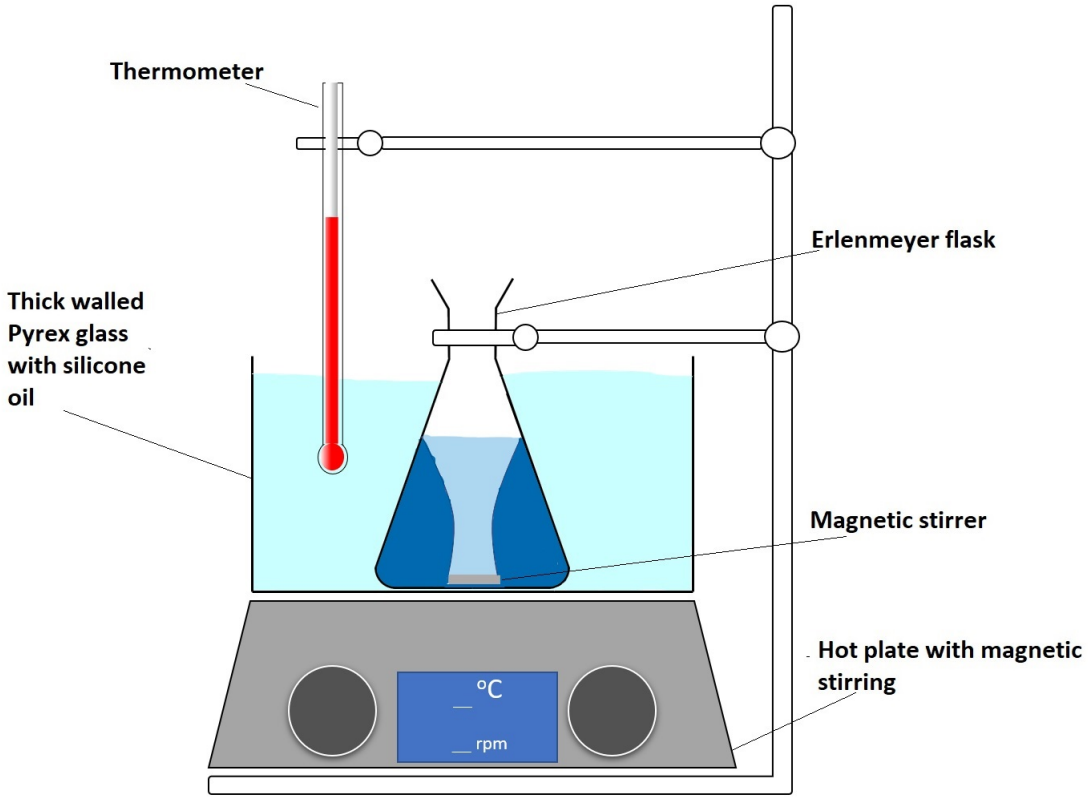

Figure 2.1: Schematic representation of Sol-gel coating experiment set-up

Lithium Zirconium Oxide coated $LiNi_{0.8}Co_{0.1}Mn_{0.1}O_2$

Lithium acetate was used as the precursor to synthesize and coat LZO on NMC811 for **Method 1**. First, 30 ml absolute ethanol was pipetted into the flask, followed by 0.0442 g $ZrO(NO_3)_2.6H_2O$ and 0.026 g $CH_3COOLi_2.H_2O$. The prepared colloid system was stirred at room temperature by a magnetic stirrer until a clear solution was achieved to produce the "Sol" precursor solution. While waiting for a clear solution, 2 g NMC811 powder was dispersed into the precursor solution with steady stirring at 480 rpm for 24 hours before being evaporated on a hot plate using an oil bath set to 90°C and kept under stirring at the same speed at until the ethanol was adequately evaporated to make the "Gel" form. The magnetic stirrer with a hot plate was switched off and the Erlenmeyer flask was pulled out of the oil bath for cooling down the temperature. Finally, the remaining materials were dried completely in a vacuum oven overnight at 50 ℃. The powder was grounded using a mortar and pestle and transferred in to a aluminium crucible for calcination. Calcination of powders was carried out in muffle furnace at 650℃ for 5 h to obtain 1 wt.% LZO coated NMC811. Similarly, 0.5 wt.%, 2 wt.%, and 3 wt.% LZO coatings were applied using the concentrations of precursors that met the molar ratio criteria of Li/Zr equal to 2.

All the previous steps before calcination of **Method 2** were similar to **Method 1**. After being grounded by a mortar and pestle, the remaining materials was pre-heated at 400 ℃ for 5 hours before being calcined at 800°C for 15 hours to obtain LZO-coated NMC811 powders. This method was used to coat 1 wt.% and 3 wt.% LZO on NMC811. Hereafter, as received NMC811, 0.5 wt.%, 1

wt.%, 2 wt.%, and 3 wt.% LZO-coated NMC811 using lithium acetate as the precursor were abbreviated as TARGRAY NMC811, 0.5LiAcZO@NMC811, 1LiAcZO@NMC811, 2LiAcZO@NMC811, and 3LiAcZO@NMC811, with each calcination process being followed by _Cal650 or _Cal800. The final products were stored in an argon glovebox for further analysis. Figure 2.2 demonstrates the step-by-step surface modification of NMC811 cathode active materials utilizing Sol-gel coating process of **Method 1** and **Method 2**.

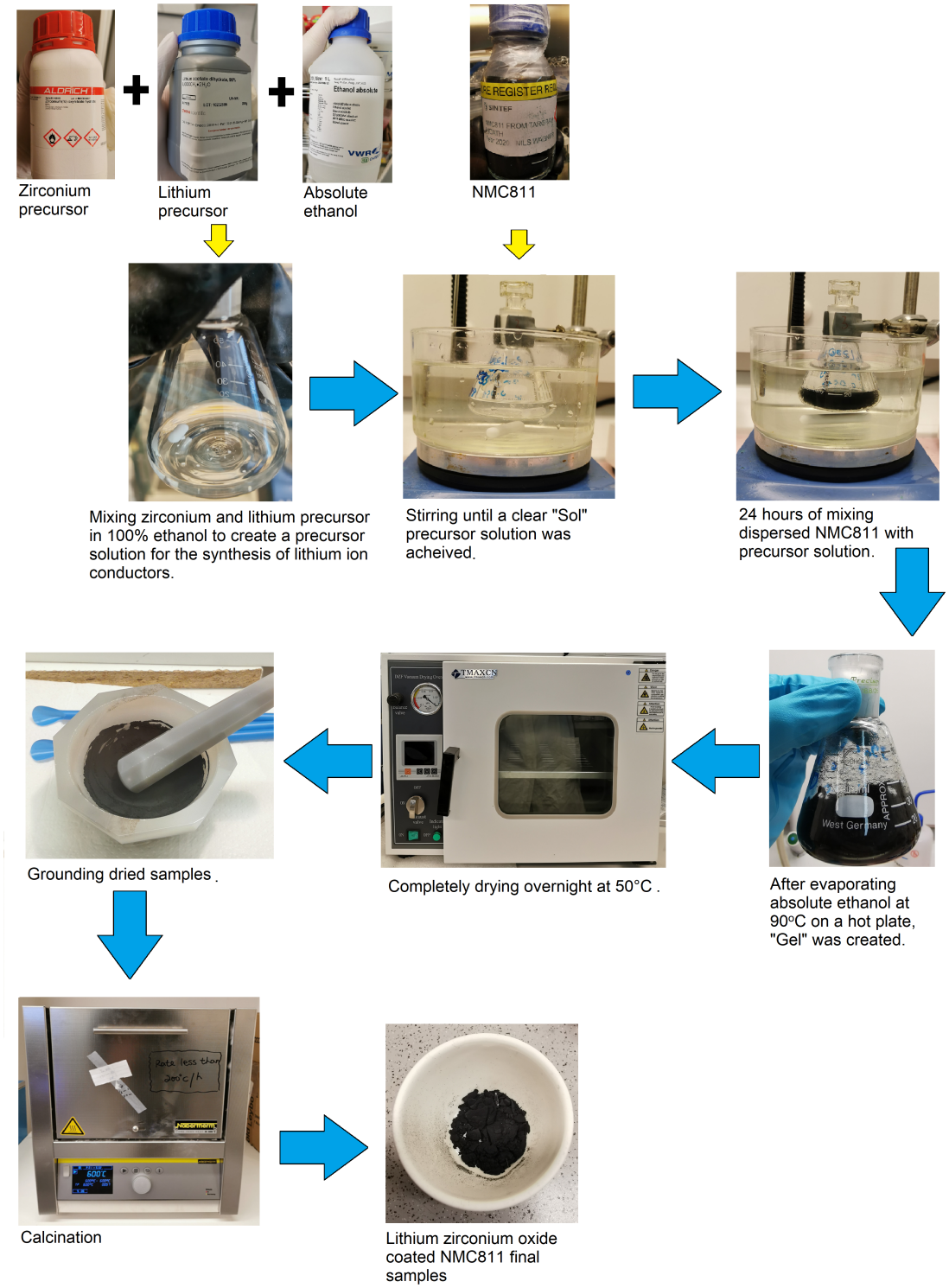

Figure 2.2: Illustration of sol-gel technique coating experiments

Table 2.1 shows the precursor concentrations and the heating process used in each experiment.

Name	**Zirconium (IV) oxynitrate hydrate** $[mg]$	**Lithium acetate dihydrate** $[mg]$	**Heating temperature** [℃]
0.5LiAcZO@NMC811_Cal650	0.0221	0.013	650
1LiAcZO@NMC811_Cal650	0.0442	0.026	650
2LiAcZO@NMC811_Cal650	0.0882	0.052	650
3LiAcZO@NMC811_Cal650	0.1326	0.079	650
1LiAcZO@NMC811_Cal800	0.0442	0.026	800
3LiAcZO@NMC811_Cal800	0.1326	0.079	800

Table 2.1: Experiment design for lithium zirconate coating using lithium acetate as the precursor

In addition, a new set of experiments were conducted in **Method 3** by using lithium nitrate as the precursor to develop in situ LZO coating on NMC811. This method is nearly similar to two previous methods with the exception of stirring during ethanol evaporation and the use of a drying vacuum instead until the samples are completely dried. The samples were taken directly to heating process with out grounding step. There were only one heating temperature in a muffle furnace at 650 ℃ for 5 hours and samples were abbreviated as 1LiNiZO@NMC811, 3LiNiZO@NMC811, 6LiNiZO@NMC811, and 9LiNiZO@NMC811, respectively and were followed by _Cal650. The concentrations of precursors used in each experiment are indicated in the Table 2.2.

Name	**Zirconium (IV) oxynitrate hydrate** $[mg]$	**Lithium nitrate** $[mg]$	**Calcination temperature** [℃]
1LiNiZO@NMC811_Cal650	0.0442	0.018	650
3LiNiZO@NMC811_Cal650	0.1326	0.0539	650
6LiNiZO@NMC811_Cal650	0.2652	0.1078	650
9LiNiZO@NMC811_Cal650	0.3978	0.162	650

Table 2.2: Experiment design for lithium zirconate coating using lithium nitrate as the precursor

In order to determine the influence of utilizing two distinct lithium precursors on the development coating process, two other experiments were conducted. In the first experiment, 0.0539 g $LiNO_3$ was used as the precursor and followed by 0.1326 g $ZrO(NO_3)_2.6H_2O$ to dissolve in 30 ml of 100% ethanol. All of following steps are identical to **Method 1** and the obtained 3 wt.% LZO-coated NMC811 sample was abbreviated as 3LiNiZO@NMC811_method1. In the second experiment, 0.079 g $CH_3COOLi_2.H_2O$ and 0.1326 g $ZrO(NO_3)_2.6H_2O$ were disovle in the same amount of absolute ethanol. All of the following steps of **Method 3** were applied on this experiment. The final powder was abbreviated as 3LiAcZO@NMC811_method3 to represent 3 wt.% LZO-coated NMC811.

2.2 Cross-sectioning Method

Cross-section particles are prepared using a destructive technique, which requires that a portion of LZO-coated NMC811 be ground away to expose the internal plane for the investigation of LZO coating layers, this method is combined with Scanning Electron Microscopes (Section 2.6.2) and Energy-dispersive X-ray Spectroscopy (Section 2.6.4) analysis.

2.2.1 Chemicals

EpoFix epoxy resin (Struers), Epofix epoxy hardener (Struers), DP-spray M, 1 μm monocrystalline diamonds (Struers).

2.2.2 Apparatus

TTegramin-20, an automatic, microprocessor-controlled machine for polishing of specimens on a 200 mm MD-Disk (Struers), Minitom, an automatic precision cutting machine (Struers), LaboPol-21, a manual grinding machine (Struers), Sputter Coater S150B for gold coating (Edwards), Silicon carbide grinding paper, grit 2400 and grit 4000 for wet grinding of materials and MD-Nap polishing cloth for final polishing of materials were utilized to prepare the samples for cross-sectional analysis.

2.2.3 Methods

First, small amount of the the coated cathode material was placed in the plastic mold/cup. Secondly, 15 ml of epoxy resin with 2 ml of hardener by volume were measured in the correct quantity by the syringes and stirred for two minutes to obatin a homogeneous solution. The prepared epoxy solution was poured into the mold with care and allowed to cure for 12h at room temperature. Prior to additional processing, which included sawing, grinding, polishing until the plane of interest was ready for gold conductive coating. Following sample preparation, the encapsulated specimen of NMC powders was cut with a diamond wheel cutter along a plane parallel to the plane of interest to reduce the amount of grinding required to expose the plane of interest in the specimen. After the specimen has been cut to the optimal size, grinding step was applied. SiC papers (silicon carbide paper) were placed on the surface of manual grinder. The grinding process began with 2400 Grit SiC paper, followed by 4000 Grit SiC paper to eliminate any scratches from the previous steps. The next step was polishing, which was similar to grinding with the exception that silk cloth containing 1 μm monocrystalline diamonds was put on the controlled polisher in lieu of SiC paper. The entire fine polishing duration was three minutes, and following this stage, all surface scratches should have been eliminated. The samples were coated with a thin layer for gold before being put on S(T)EM standard holder for further characterization. Figure 2.3 represents the prepareation of cross-sectioning NMC particles for S(T)EM imaging.

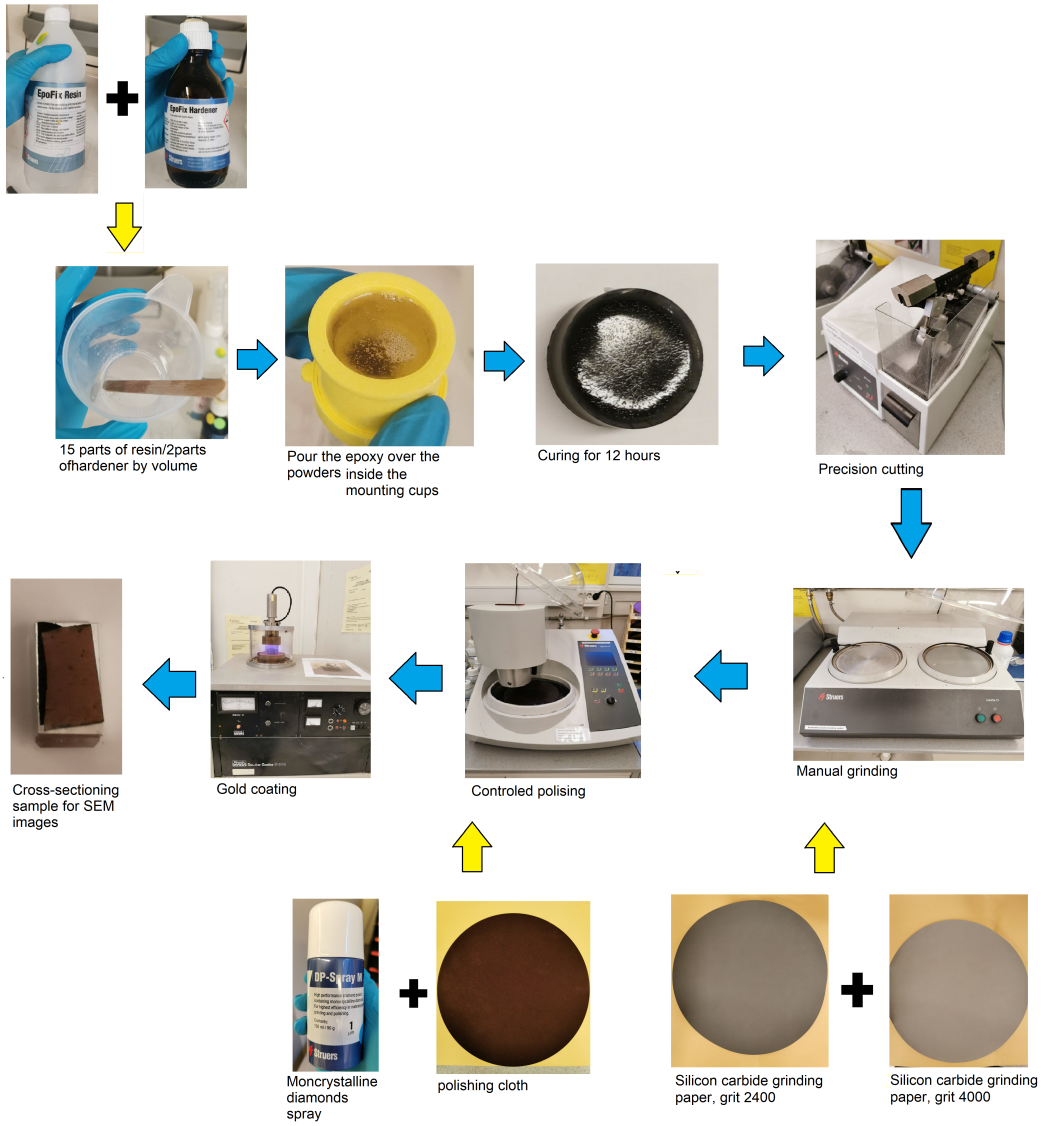

Figure 2.3: Cross-sectioning steps of LZO-coated NMC811.

2.3 Microwave digestion of commercial and LZO-coated NMC811

TARGRAY NMC811 and LZO@NMC811 were digested to evaluate the amount of metals in solid samples. This method is combined with Microwave Plasma Atomic Emission Spectroscopy (Section 2.6.5) characterization.

2.3.1 Apparatus

Speedwave XPERT for Microwave Digestion Systems by Berghof Products.

2.3.2 Chemicals

Nitric acid $\geq$ 65% (HNO_3) was distributed by Sigma-Aldrich, hydrochloric acid ACS reagent, 37 % (HCl), MQ water was distilled from Millipore water filtration system

2.3.3 Method

A specified quantity of TARGRAY NMC811 and LZO-coated NMC811 was weighed out in separate weighing cups (Speedwave XPERT accessories) and transferred to the digesting vessels. The vessels were then added to an 8 ml aqua regia solution of HCl and HNO_3 (volumetric ratio 5:3) and allowed to react for 10 minutes in a fume hood. After that, the vessels were closed and sealed. A appropriate digestion protocol (Table 2.3) was meticulously modified and implemented.

Step	**T** (℃)	**P (bar)**	**Ramp (min)**	**Hold (min)**	**Power (%)**
1	150	40	10	15	40
2	180	40	10	25	40

Table 2.3: Speedwave XPERT application settings for cathode active material powders digestion

Figure 2.4 shows the powder at the beginning, followed by the steps of digestion and the filtered suspension.

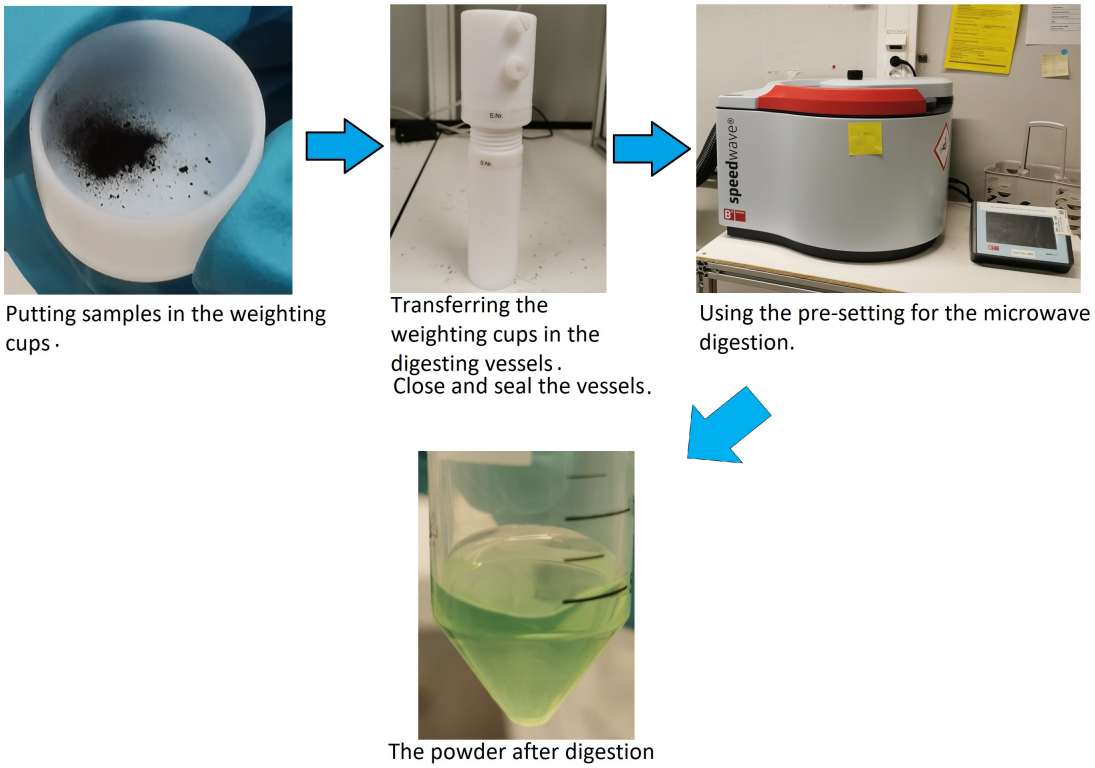

Figure 2.4: CAM powder before and after digestion and how digestion performs

After the process was complete, the vessels were allowed to cool before the samples were transferred to centrifuge tubes and diluted with MQ water. Table 2.4 indicated that all samples were digested prior to MP-AES analysis.

Sample	Digesting weight (g)	Dilution volume (mL)
Commercial NMC811	0.0525	50
0.5LiAcZO@NMC811_Cal650	0.0500	50
1LiAcZO@NMC81_Cal650	0.0410	100
2LiAcZO@NMC811_Cal650	0.0507	50
3LiAcZO@NMC811_Cal650	0.0523	50

Table 2.4: Sample digestion table for MP-AES analysis

Each sample was then filtered using PTFE 0.2 m Hydrophobic Syringe Filters and continuously diluted 50 times for detecting Li, Ni, Co, and Mn contents and two times for detecting Zr contents separately. Now, all the samples were prepared for further MP-AES analysis in Section 2.6.5.

2.4 Lithium-Indium alloys fabrication

Li-In alloys were fabricate by coulometric titration of indium by lithium in coin cells for the anode of ASSBs.

2.4.1 Chemicals

Lithium bisimide $\geq$ 99,0% ($LiC_2F_6NO_4S_2$, Sigma Aldrich), dioxolane DOL $\geq$ 99,0% $(CH_2)_2O_2CH_2$, Sigma Aldrich), dimethoxyethane DME $\geq$ 99,0% ($CH_3OCH_2CH_2OCH_3$, Thermo Scientific), dimethym carbonate DMC $\geq$ 99,0% ($H_3COCOOCH_3$, Thermo Scientific), indium foil 99.99% (Thermo Scientific), lithium disc (TMAX-LCO).

2.4.2 Apparatus

LABmaster pro glove box workstation with powerful closed loop integrated gas purifier circulation was provided by MBRAUN, automatic coin cell crimper wasprovided by Hohsen Crops., 2016 coin cells comprise a large bottom cap and a small top cap, 0.3mm stainless steel spacer, 18mm Celgard separator.

2.4.3 Methods

2032 coin cell assembly beginning with a 10mm indium foil was placed on top of a large bottom cap made of stainless steel followed by an 18mm Celgard separator. As an electrolyte, a 1 M solution of LiTFS was dissolved in a 1:1 mixture of DOL and DME. All solvents were dried in molecular sieve (4Å) for 24 hours and lithium bis(trifluoromethanesulfonyl)imide was used as received. Then 50 μL mixture of liquid electrolyte was added on the separator. During handling and storage, a 14mm lithium disc may get oxidized; therefore the surface was cleaned with a stainless steel scalpel until a shiny silvery surface emerged before placed on the liquid electrolyte to use as a counter electrode. Before closing the cell with the small top cap, a 0.3mm-thick stainless steel spacer was positioned over the lithium disc and a gasket was inserted in the big bottom cap. The coin cell was crimped for 5 seconds using an automated coin cell crimper. The assembling of the cell was performed in an argon-filled glovebox (O_2 and $H_2O \leq$ 0.1 ppm). Coulometric titration was performed by discharging the cell at 0.1mA.cm^{-2} with 10 second discharge and 10 second rest cycles for 6 hours. In order to collect the lithiated indium foil that was connected to the stainless steel spacer, the cell was disassembled using the coin cell disassembler tool. After the lithiated In foils had been retrieved, they were washed with DME and then dried in an oven, placed inside the glovebox, at 50 ℃ for 2h. The general procedure for the lithiation of indium foil is illustrated in Figure 2.7

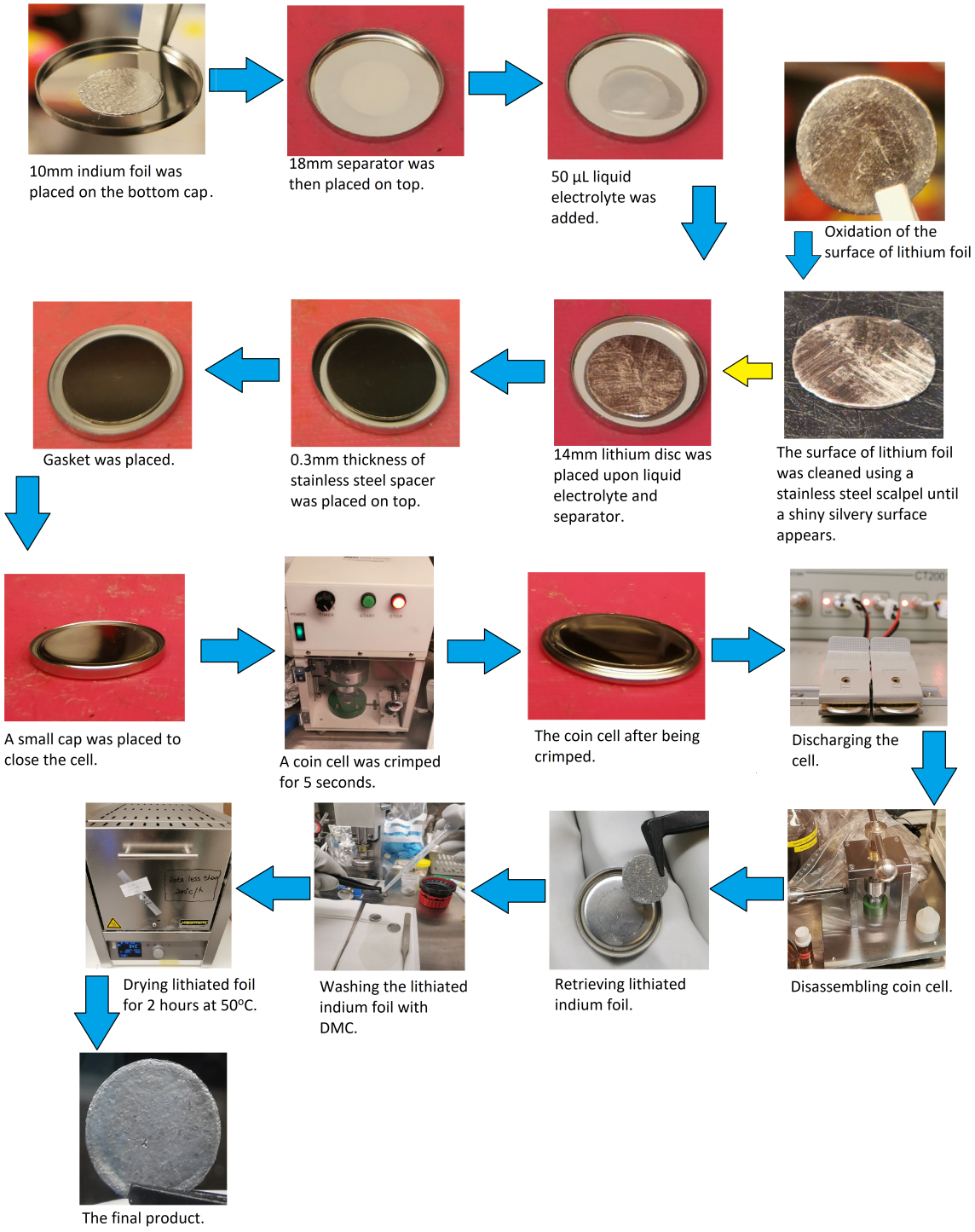

Figure 2.5: Illustration of making of Li-In alloys

2.5 ASSB Cell Assembly

ASSBs were assembled using cathode composite pellets containing pure NMC811 powder and LZO-coated NMC811 powder separately; LPSCl pellets as SE; and Li-In alloy for anode.

2.5.1 Chemicals

Lithium Phosphorus Sulfur Chloride LPSCl powder (Li_6PS_5Cl, NEI Corporation), SUPER C65 Nano Carbon Black (NEI Corporation), lithium nickel manganese cobalt oxide commercial NMC811 powder (TARGRAY), lithium zirconium oxide coated lithium nickel manganese cobalt oxide LZO@NMC811 were synthesized in Section 2.1, lithiated indium foil was fabricated in Section 2.3.

2.5.2 Apparatus

Polyether ether ketone (PEEK)-cells with 10mm press dimension, 30mm chamber depth and 50x120mm outside dimension are provided by Zhengzhou TCH Instrument, tons force applications with reinforced external pressure assemblies are provided by workshops of Faculty of Natural Sciences at NTNU, manual hydraulic pellet press 15 Ton is distributed by Specac,

2.5.3 Methods

Half-cells of SSBs including NMC811 with varied weight percentages of LZO coating synthesized were fabricated and investigated in an Argon gas environment. CAM, LPSCl, and carbon black (C65) were mixed uniformly using an agate mortar and pestle for 20 min to create composite cathodes (the NMC811:LPSC:C65 ratio was 11:16:1 by weight). To assemble the cell, 80 mg of LPSCl powder was filled into a 10-mm-diameter polyether-ether-ketone (PEEK) cell die and pressed for 3 min at a pressure of 300 MPa using the hydraulic press. 12 mg of the composite cathode was distributed uniformly on the top of the flat LPSCl pellet in the long Ti die and re-pressed at 300 MPa for three minutes using the hydraulic press. Li-In alloy was then added to the other side of the pellet and finally pressed at 120 Mpa for 1 min using the hydraulic press. The cross-sectional diagram of battery stack within the assembly is shown in Figure 2.7.

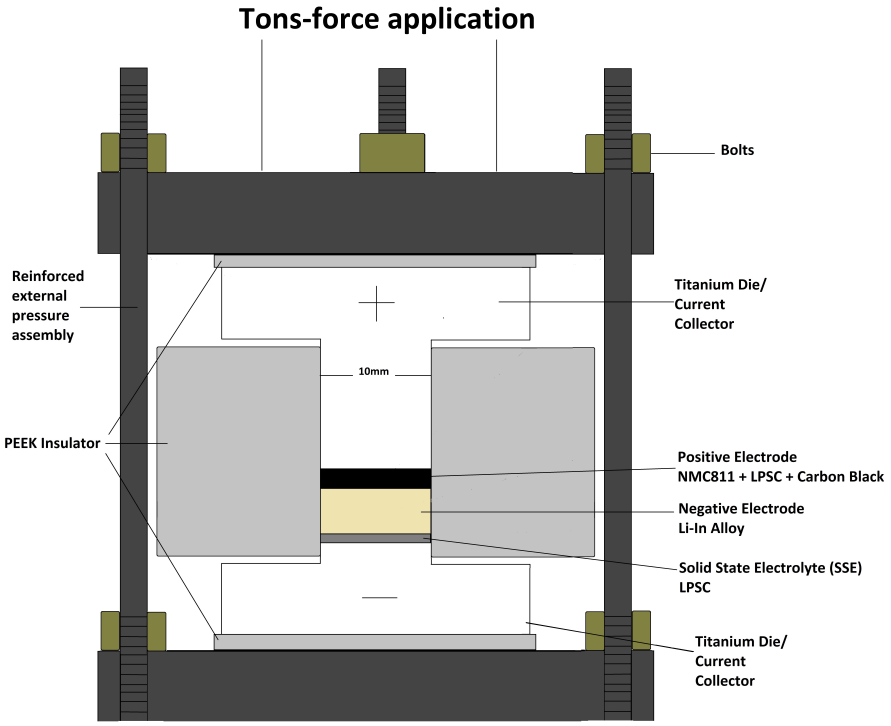

Figure 2.6: Cross-sectional diagram of a titanium/PEEK test die used to apply and maintain pressure on an all-solid-state battery.

The assembly consisted of two machined Ti die that were uniaxially forced onto the cell stack by two stainless steel metal plates, which were tightened by three nuts joining the bottom steel plate and three bolts connecting the top steel plate. Before cycling, the assembly was finally uniaxially compressed using a torque wrench set to 5.5 Nm. This set up of stack pressure was chosen to achieve optimal capacity within the cells.

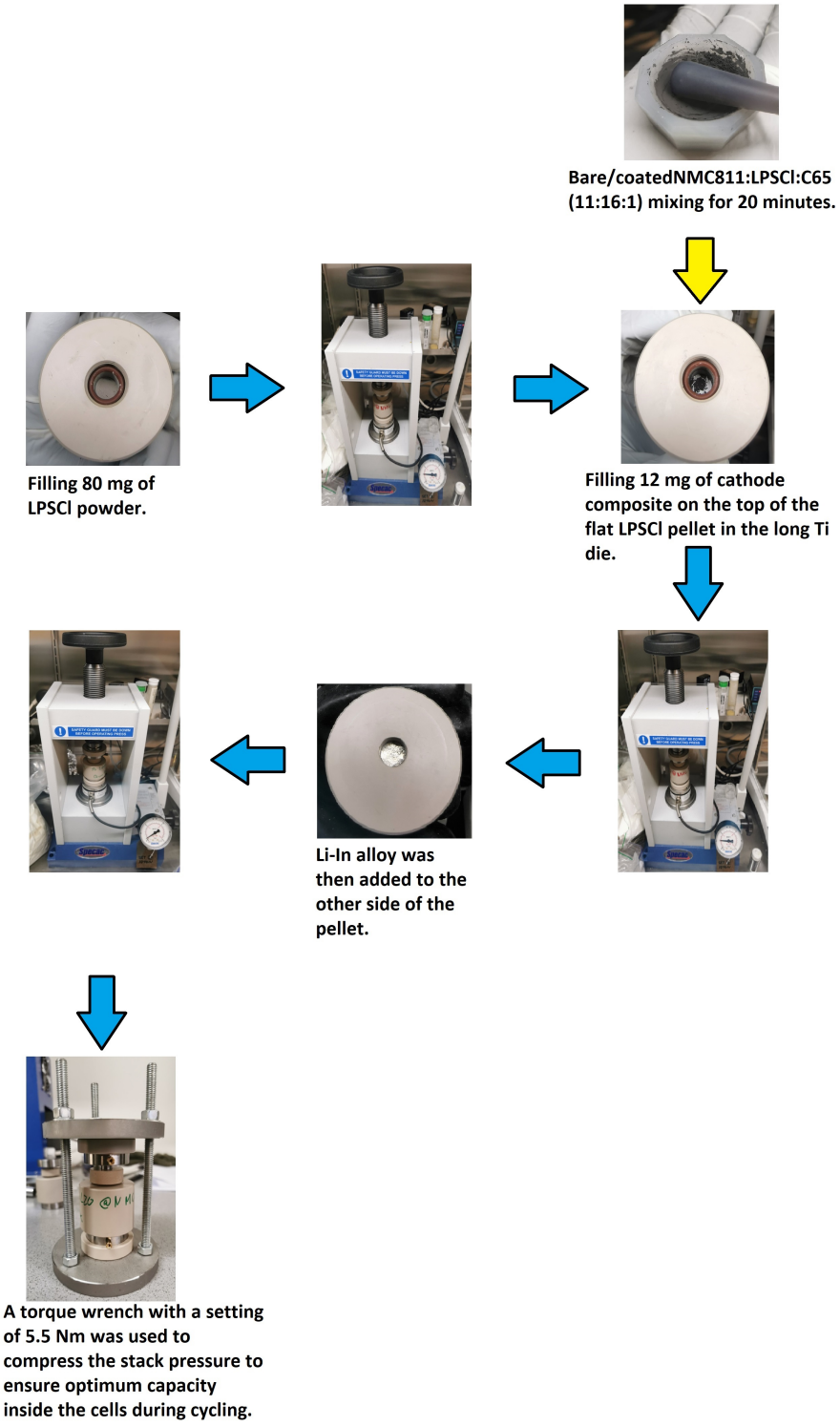

Figure 2.7: Illustration of making ASSB half cell.

2.6 Materials Characterization and Electrochemical Testing

2.6.1 Powder X-ray Diffraction

X-ray diffraction (XRD) is a powerful non-destructive technique for analysing the crystalline materials. Information on structures, phases, preferred crystal orientations (texture), average grain size, and crystal defects etc., can be obtained from X-ray diffraction. X-rays with wavelengths between 0.01 and 10 nm may be diffracted by the repeating atom planes in a crystal because their wavelengths are in the same range as the atomic distance. As illustrated in Eq. (2.1), Bragg's law is utilized to explain the emergence of a unique diffraction pattern that identifies a particular structure.

$$n\lambda = 2d \cdot \sin\theta \tag{2.1}$$

where θ is the angle between the incident X-ray beam and the corresponding parallel imaginary planes, λ is the X-ray wavelength, and d is the distance between crystallographic planes, as shown in Figure 2.8

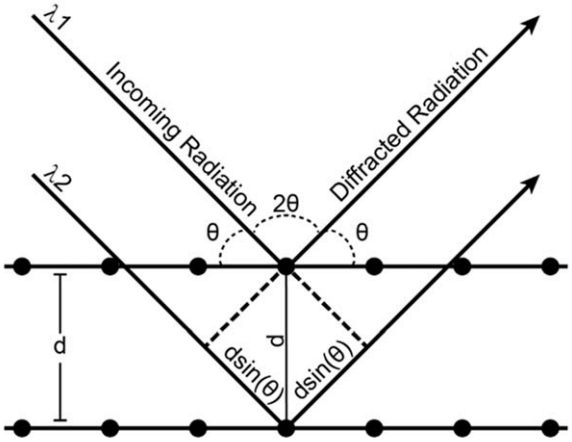

Figure 2.8: Schematic representation of the conditions of Bragg's law [131].

The fundamental concept is that X-ray beams scattered from consecutive planes in a crystal would travel a distance that differs by precisely one wavelength (for n=1). X-rays dispersed from consecutive planes will interact constructively when they reach the X-ray detector at an angle θ. As the powder sample includes millions of differently oriented single crystals, the diffraction beams go in all directions according to Bragg's law, resulting in the diffraction pattern. As X-Ray is scattered by electron clouds surrounding the atoms, the intensity of the diffraction beam corresponds directly to the quantity and location of the electrons. Eq. (2.2) relates the intensity of the peaks to the structural factor F as follows:

$$I = A \cdot F^2 \tag{2.2}$$

Where A contains other variables like as polarization, absorption, and temperature. Consequently, the XRD pattern is used to analyze the crystal structure information. In this thesis, XRD patterns of solid samples (CAM) were acquired using an X-ray Diffractometer (XRD, Bruker D8 A25 DaVinci) with Cu Kα_1 (λ=1.5406Å) and Cu Kα_2 (λ=1.5444Å) radiation. For the detection of NMC811 crystal structure information and LZO coating layer, the analysis was done in the range of 10-80°, with a step size of 0.024° and a step time of 2 seconds, for a total of 100 minutes. In addition to detecting the coating layer using low concentrations of zirconium precusor, the step size and step time were adjusted to 0.045° and 5.13 seconds, respectively, resulting in a total measurement duration of 2 hours per sample. To enable X-ray penetration while preventing exposure to air and moisture during measurement, all samples were placed on a silicon zero background holder and a protective Kapton tape was sealed by Kapton holder. To determine the lattice parameters

of samples, the program Topas used Rietveld refinement which utilizes the position, width, and intensity of the peaks in order to match the peak positions with a certain space group.

2.6.2 Scanning Electron Microscopy

The scanning electron microscope (SEM) is one of the most flexible tools for examining and analyzing the morphology on the surface of micro/nanostructures and their chemical composition. The generation of an image in the SEM is based on the acquisition of signals generated by the electron beam and specimen contacts. These contacts can be categorized into two major groups: elastic scattering and inelastic scattering. Inelastic scattering occurs through a number of interactions between incident electrons and the electrons and atoms of the sample, resulting in the transfer of significant energy from the main beam electron to the atom. The quantity of energy loss depends on whether the electrons of the specimen are excited singularly or collectively, as well as the electron's binding energy to the atom. Consequently, the excitation of specimen electrons during ionization of specimen atoms generates secondary electrons (SE), which are utilized to analyze the sample. Typically, the energies of SE are low, so they only occur near the specimen's surface (10nm depth) and the deeper ones are absorbed on their way out. Meanwhile, elastic scattering is caused by the deflection of the incident electron by the specimen's atomic nucleus or by similar-energy outer shell electrons. This kind of interaction is characterized by negligible energy loss during the collision and by a wide-angle directional change of the scattered electron. Backscattered electrons (BSE) are incident electrons that are elastically scattered at an angle greater than 90° and heavier components scattered better than lighter ones. BSE gives information on the atomic number and phase difference with greater energy than SE, therefore deeper BSE (1-3µm) may also be identified; however, the spatial resolution of the images is diminished owing to the teardrop-shaped interaction volume. In addition to the signals used to generate an image, a variety of additional signals are produced when an electron beam strikes a sample shown in Figure 2.9, including the emission of characteristic X-ray which will be discussed in Section 2.6.4, all of the signals are detected by specialized detectors.

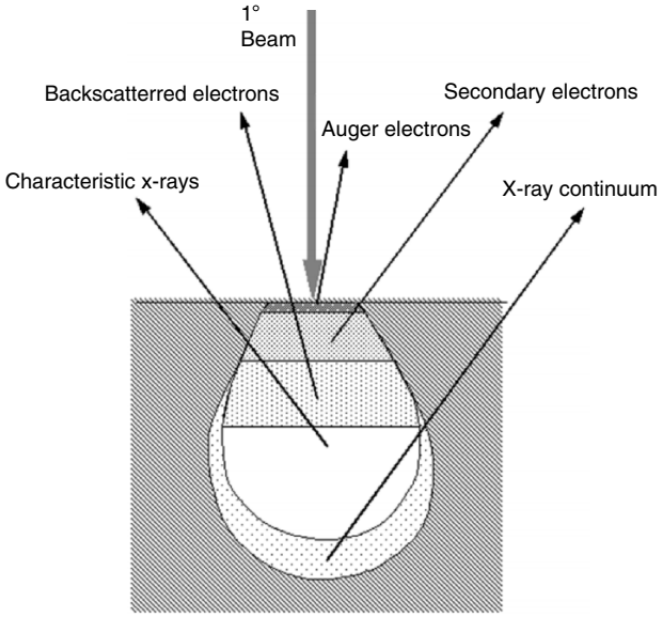

Figure 2.9: Multiple signals produced by the electron beam–specimen interaction in the scanning electron microscope and the regions from which they can be detected [132].

The majority of the time, when an incident electron hits the surface of a specimen, the energetic electrons penetrate deeper into the sample before they encounter and collide with a specimen atom. The volume and depth of electron penetration rise with increasing beam energy and decrease

with rising specimen atomic number. This is because specimens with a higher atomic number contain a greater number of particles that may block electron penetration. One effect of the interaction volume on signal collection is that the use of a high accelerating voltage will result in a deep penetration length and a wide main excitation zone, resulting in the loss of sample surface information. For all the reasons stated above, SE mode with low accelerating voltage (1kV) was used in this thesis in order to achieve the best surface resolution for examining the change of morphology of NMC811 particles before and after being functionlized.

2.6.3 Scanning Transmission Electron Microscopy

The scanning transmission electron microscope (STEM) is an exceptionally potent and adaptable equipment capable of imaging with atomic resolution and nanoscale analysis. STEM and SEM are similar in many ways, however, whereas SEM normally uses a bulk sample, STEM needs a thinned, electron transparent specimen. The most often used STEM detectors are therefore situated after the sample and detect transmitted electrons. STEM's major strength is that probe sizes below the interatomic spacings in various materials are often attainable. Atomic resolution images are easily created, and the probe may then be stopped over an area of interest for spectroscopic investigation at or near atomic resolution. Bright-field (BF) and dark-field (DF) detectors are two of the most used in STEM which collect the transmitted electrons. The BF detector typically collects across a disc of scattering angles centered on the optic axis of the microscope, but the DF detector collects over an annulus at a higher angle where only scattered electrons are detected. In fact, the capacity of STEM to do DF imaging is one of STEM's greatest assets. It gives images that are generally immune to focusing errors and has a high sensitivity to atomic number, in which compositional changes are evident in the contrast, enabling various elements to appear with varying intensities. For this reason, DF detector was used in this thesis to detect the coating layers of LZO on NMC811 and copper grids with a 300 mesh were used to prepare the samples for taking images. Hitachi S-5500 Scanning Transmission Electron Microscopy enabled with the secondary electron (SE) detector, which is described in Section 2.6.2 and the energy-dispersive X-ray (EDX) spectrometer,which will be mentioned in Section 2.6.4, was used for samples morphology analysis.

Figure 2.10: Hitachi S-5500 S(T)EM

2.6.4 Energy Dispersive X-ray Spectroscopy

As shown in Figure 2.9, X-ray emission is a phenomena caused by the excitation of the inner shell by incident electrons. In other words, when an inner shell electron transits to a high-energy

level, the inner shell hole is filled by an electron at a high-energy level, resulting in the emission of a characteristic X-ray with energy between these two energy levels. These characteristic X-rays contain different energies which is detected by the detector in order to identify the chemical elements present in a sample (qualitative analysis) and to estimate their relative abundance (quantitative analysis). In this thesis, EDX was performed in conjunction with an STEM with the accelerating voltage of 20kV in order to detect the elements of Ni (Kα = 7.480 and Lα = 0.849), Co (Kα = 6.931 and Lα = 0.775), Mn (Kα = 5.900 and Lα = 0.637), Zr (Kα = 15.775 and Lα = 2.044) and O (Kα = 0.525).

2.6.5 Microwave Plasma Atomic Emission Spectroscopy

Microwave plasma atomic emission spectroscopy (MP-AES) is an atomic emission method designed to detect elements and determine their concentrations in various types of materials. MP-AES with a self-sustaining atmospheric pressure microwave plasma source using nitrogen gas, generated by a nitrogen generator, provide a novel alternative to both atomic absorption spectrometry (AAS) and inductively coupled plasma atomic emission spectrometry (ICP-AES). In addition, the technique has several advantages such as smaller footprint, multi-element capability, good detection power and speed. The intensity of each emitted line will be directly proportionate to the element's concentration. However, this technique operates on a similar concept as any other emission technology. Few steps are involved in this procedure, including sample introduction into the high temperature source, atom formation, excitation, and emission, measurement of the emitted light intensity of a specific element of interest at a specified wavelength, and determination of the concentration by comparing it to that of a known concentration. Liquid and gas samples may be injected directly into the instrument, however solid samples must be dissolved in a solvent before analysis. Commercial NMC811 and LZO-coated NMC811 were digested by the use of the Speedwave XPERT Microwave Digestion System in Section 2.3 prior to MP-AES analysis.

ICP Multi-element standard solution IV (1000 mg/L Ag, Al, B, Ba, Bi, Ca, Cd, Co, Cr, Cu, Fe, Ga, In, K, Li, Mg, Mn, Na, Ni, Pb, Sr, Tl, Zn) was used to prepare calibration standards of 50, 25, 12.5, 6.25, 3.125, 1.5625 and 0 mg/L using MQ water. The software connected with the MP-AES created external calibration curves for measuring metals (Li, Ni, Co, and Mn). For measuring Zr metal, calibration curves were made using standards of 6.25, 3.125, 1.5625, 0.7812, 0.3906, 0.1953, 0.0976, and 0 mg/L. This was done by diluting the initial ICP Multi-element standard solution XVII (100 mg/L Hf,Ir, Sb, Sn, Ta, Ti, Zr) with MQ water. The Agilent 4210 MP-AES was employed for these analyses, as seen in Figure 2.11.

Figure 2.11: MP-AES agilent 4210

2.6.6 Galvanostatic Cycling with Potential Limitation

Galvanostatic Cycling with Potential Limitation (GCPL) is a common electrochemical cycling technique in which a constant current is applied to a cell until a certain quantity of charge has been transferred or a cutoff voltage is reached. Generally, negative current forces discharge a cell whereas positive current forces charge it. In this thesis, GCPL is used to investigate the specific capacity, rate capability, capacity retention, and cycle life of a CAM. The CAM is oxidized/reduced with cation de/insertion when a constant current is applied. The related voltage response might be a linear increase/decrease with respect to capacity, corresponding to a solid solution de/insertion process, or a flat plateau, resulting from a two-phase reaction. As the capacity limit is approached, voltage increases and decreases will accelerate significantly. "C-rate" refers to the applied cycling current, which is proportional to the specific capacity Q of the materials, which is proportional to the molar mass M_W of the compound and may be determined by Eq. (2.3):

$$Q = nF/3.6M_W \tag{2.3}$$

where F is Faraday's constant and n is the number of transported electrons. $1C$ rate indicates the battery is charged and discharged in one hour. C/x rate indicates that the battery is charged and discharged in x hours, correspondingly. GCPL was carried out with all of the SSBs that were assembled in Section 2.5, each consists of a cathode (bare/coated NMC811 mixed with LPSCl and C65) and an anode (Li-In alloy) which is separated by a layer of LPSCl as SE. The measurements were performed with the Battery Test System CT3002A (Landt Instruments) at 2.38 - 3.68V with C-rates ranging from 0.1C to 2C

Chapter 3

Results and Discussion

3.1 Pristine Cathode Active Material

Before the material was subjected to any surface modification (Section 2.1), characterizations using XRD, S(T)EM, EDX, and MP-AES were performed in order to investigate the morphology, crystallinity phase, and composition of the commercial NMC811 (Targray).

3.1.1 Phase Identification of Pristine CAM by XRD

TARGRAY NMC811 was taken for an XRD analysis, resulting in the pattern seen in Figure 3.1.

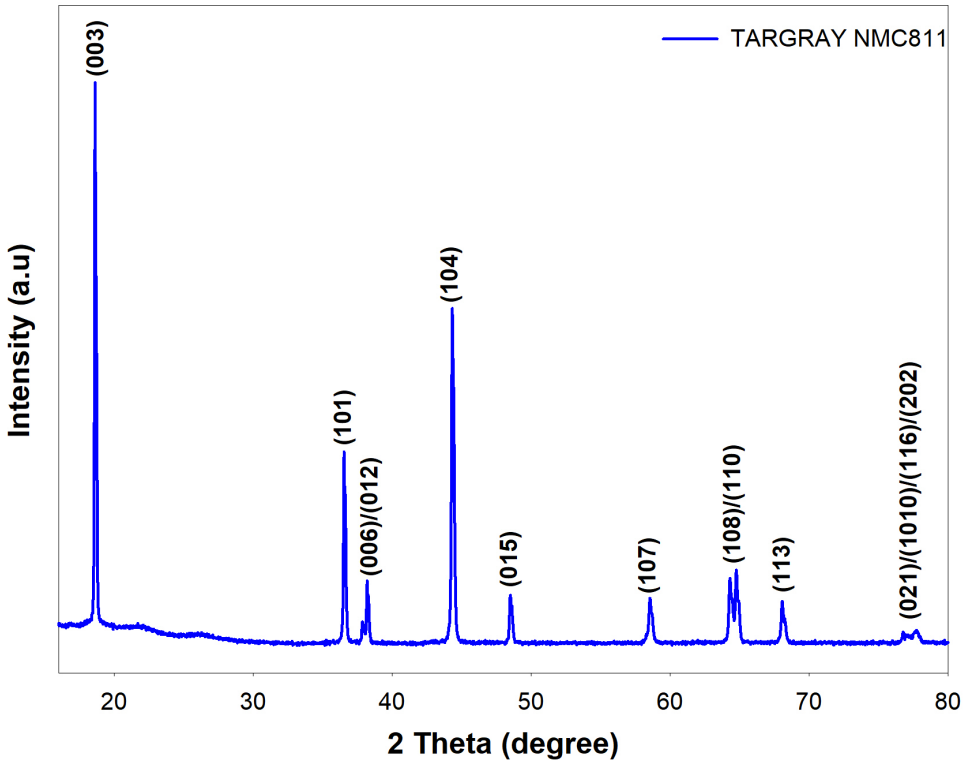

Figure 3.1: XRD patterns of NMC811 material from Targray

The measurement conditions for the high level of crystallinity can be found in Section 2.6.1. The sample has high crystallinity for the sharp diffraction peaks. The layered hexagonal α-$NaFeO_2$ structure with the R-3m space groups is well indexed by the strong XRD peaks, and the pristine CAM is composed of the metal oxide compound NMC811 (PDF No. 00-066-0856). Separation of the (108)/(110) and (006)/(102) peaks around 38° and 65° indicates that the sample may have a highly ordered layered structure [133].

Sample	a	c	c/a	$I_{(003)}/I_{(104)}$	$I_{(006)} + I_{(012)}/I_{(101)}$
TARGRAY NMC811	2.8752	14.2180	4.9450	1.6191	0.6493

Table 3.1: Lattice parameters of TARGRAY NMC811

In Table 3.1, the parameters of the lattice were found by fitting the positions of the peaks to an R-3m space group. The ratios c/a and $I_{(003)}/I_{(104)}$ have been reported to indicate the direction of cation mixing. Furthermore, cation mixing may occur when the c/a ratio is less than 4.96 and the $I_{(003)}/I_{(104)}$ ratio is less than 1.2 [134]. The sample has high $I_{(003)}/I_{(104)}$ values, as well as a c/a value of 4.9450. Besides, the sample has a good hexagonal ordering because of the low value of $I_{(006)} + I_{(012)}/I_{(101)}$ [135].

3.1.2 Morphology Examination of TARGRAY NMC811 by S(T)EM

The particle morphology of TARGRAY NMC811 was investigated using S(T)EM in SE mode.

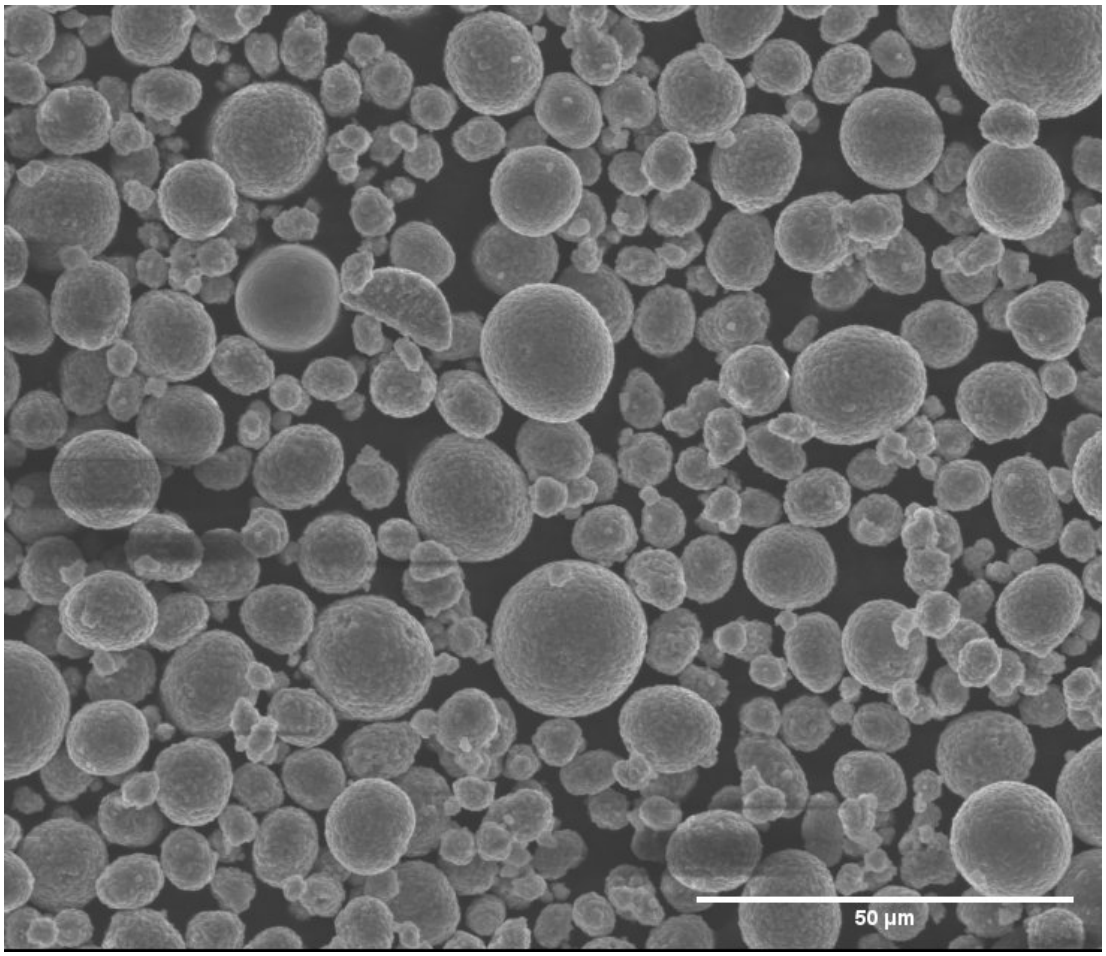

Figure 3.2: S(T)EM image of Targray NMC811 material at low magnification in SE mode.

S(T)EM was used to analyze a small amount of the powder samples applied to carbon-conductive tape (Section 2.6.3). The S(T)EM image at low magnification (Figure 3.2) (emission current of 20300 nA and accelerating voltage of 20 kV) reveals that the TARGRAY NMC811 are monodispersed. The pristine powders are spheroidal in diameter 5 $\sim$ 25 µm composed of polyhedral primary particles. It also can be seen that some NMC811 particles experienced cracking before any further modification, cell assembly or cycling were taken placed.

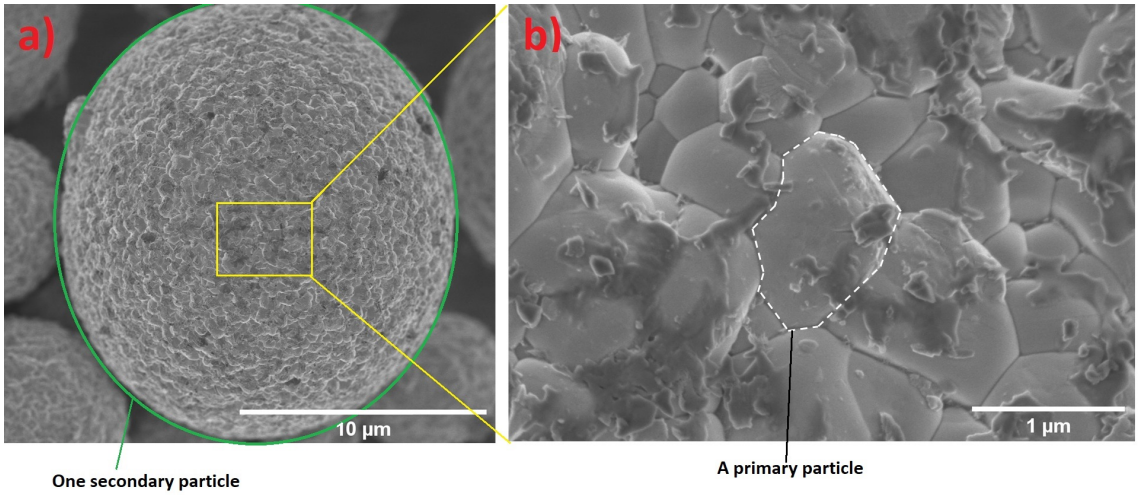

Figure 3.3: High-magnification S(T)EM images in SE mode of a) one secondary and b) a primary particle of NMC811 materials from Targray.

The images (10100 nA of emission current and 1 kV of accelerating voltage) at a high magnification (Figure 3.3) can observe one secondary particle of NMC811 consisting of densely packed single crystals (primary particles) with mostly random orientations. The size of the secondary particle measures $\approx$ 20 µm in diameter and has a relatively spherical shape; yet, it has been indicated that the sizes of secondary particles vary throughout the powders (Figure 3.2). In the PDS of NMC811 (SNMCC03008) provided by Targray [136], the particle size distribution has been reported to be D10/µm, D50/µm and D90/µm equals to 6.1, 12.1 and 21.8, respectively. The spherical morphology of NMC811 has been reported to have a relatively small surface area, which may increase the volumetric density and reduce side reactions between the cathode and electrolyte [57]. The grain boundaries between primary particles could be seen with the magnification in Figure 3.3b) The problems of this structure, according to Minnmann et al. [57], during the charging and discharging process, cracks can form inside the primary particles and along the grain boundaries between the primary particles. These cracks could make the cathode's surface area larger, which could lead to more side reactions. Moreover, it was observable that the surfaces of TARGRAY NMC811 primary particles may contain traces (Figure 3.3b). According to the material's PDS [136], the TARGRAY NMC811 powder contains Fe, Na, and Cu impurities in concentrations of 21, 75, and 3 ppm, respectively. TARGRAY NMC811 was subjected to qualitative (Section 2.6.4) and quantitative (Section 2.6.5) analysis to confirm the contaminants.

To explore the internal morphology of the secondary particles, a typical micron-sized sphere ($\approxeq$ 16 m) of TARGRAY NCM811 were cross-sectioned using the cross-sectioning method (Section 2.2). In the S(T)EM images (19900 nA of emission current and 20 kV of accelerating voltage) of cross-sectional particles (Figure 3.4), it was possible to detect the sharp grain boundaries, which provide details of the internal submorphology of the polycrystaline NMC811. The spheres are composed of tightly packed primary nanoparticles of diverse sizes and shapes. The hexagonal unit cell enables 12 different symmetries [137], which may explain the heterogeneity in NMC811 particle morphology. Figure 3.4b shows the magnification of the marked area of the sphere that depicts the arrangement of the nano- and submicron-sized particles that make up the NCM811 spherical primary particles. During EDX analysis, it is easy to see the layer of electrically conductive gold that has been added to keep the sample from getting charged. However, it is difficult to recognize the traces that have appeared before on the surface of the primary particles (Figure 3.3b). These traces may be

eliminated during surface preparation of cross-sectional particles.

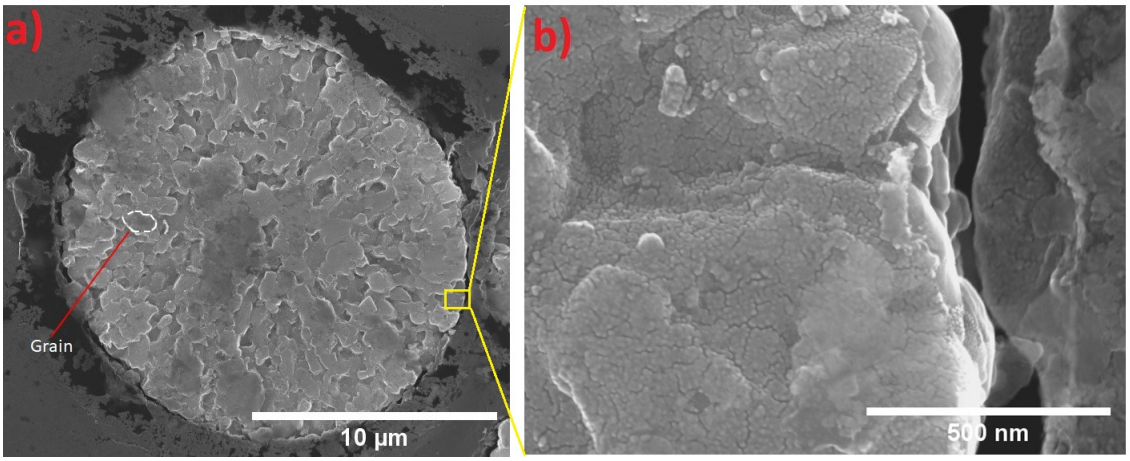

Figure 3.4: Cross-sectional S(T)EM image of a) the internal submorphology of the secondary spherical NMC811 particle from Targray, b) magnified view of the submicron primary particles that compose microspheres and a partial part of surface in SE mode.

S(T)EM images in BF (Figure 3.5a) and DF (Figure 3.5b) modes reveal more detailed morphology of the TARGRAY NMC811. Both images indicate that the surface of the commercial NMC811 particle is smooth and free of layering phenomena. Since there is no sign of traces, it is possible that the levels of contaminants are too low to be seen in DF and BF mode.

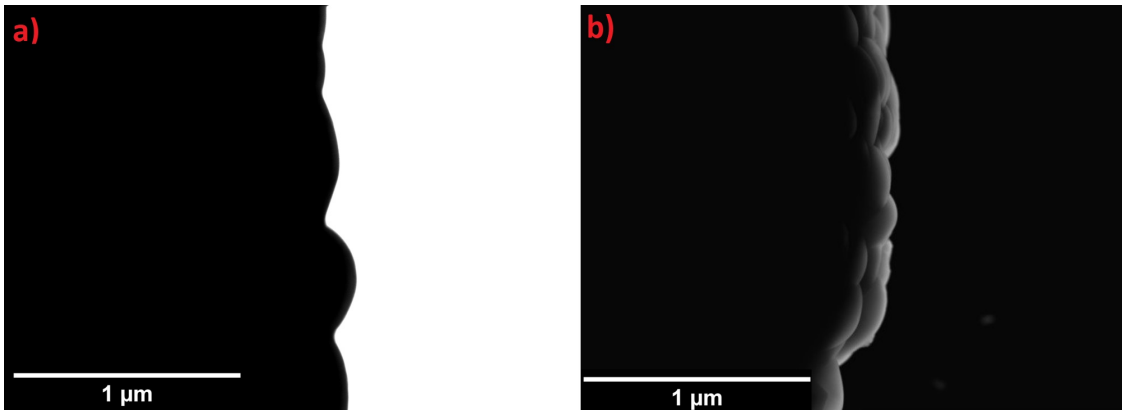

Figure 3.5: S(T)EM image of NMC811 materials from Targray a) in BF mode, b) in DF mode.

3.1.3 Qualitative Elemental Analysis of Pristine CAM by EDX.

AutoID was performed in AZtec Software for EDX mapping to establish that the particle is composed of the metals (Ni, Mn, and Co) and to identify the impurities in TARGRAY NMC811 powder. Each element, including Ni, Co, Mn, and O, is distributed uniformly throughout the particle. Na and Fe have been reported as the impurities of TARGRAY NMC811 [136], but Zr has also been detected in the elemental mapping, although at a lower level than the other two impurities, as will be discussed later. Due to the low concentration of traces, the visual contrasts of the Na, Fe, and Zr elemental mappings are weaker than those of Ni, Co, Mn, and O.

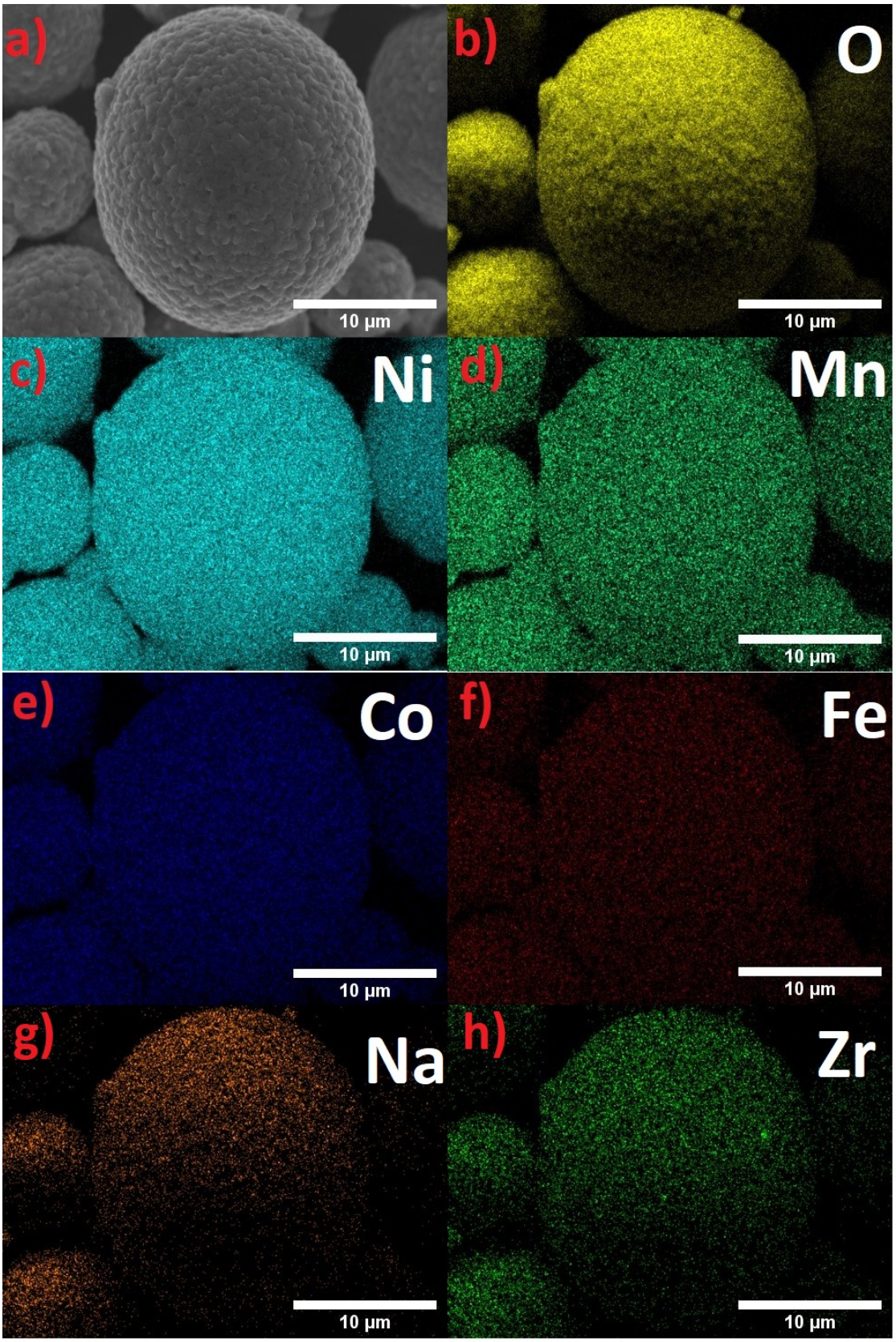

Figure 3.6: a) S(T)EM image of NMC811 from Targray sample; EDS mappings of (b–h) O, Ni, Mn, Co, Mn, Fe, Na and Zr.

A typical EDX spectrum has been established, as depicted in Figure 3.7 to demonstrate the presence

of O, Ni, Co, Mn, and traces. The O peak at 0.525 keV has the strongest signal, followed by the Ni peaks (Lα = 0.849 keV and Kα = 7.480 keV). The peak signals of Mn (Kα = 6.931) and Co (Kα = 5.900) are substantially lower than those of two other atoms. In addition, the amplifying EDX spectra pattern of pristine NMC811 has minor peaks at 1.041, 2,042, and 6.398 keV which correspond to the impurities Na, Zr, and Fe, respectively. However, the Zr peaks are almost invisible, indicating that the TARGRAY NMC811 powder contained trace amounts of Zr impurities This will be compared to the Zr intensities in the TARGRAY NMC811 EDX spectrum after surface modification later on. EDX might also identify C atoms (Kα = 0.277); however, the majority of this signal may originate from the carbon conductive tape in the analyzed area.

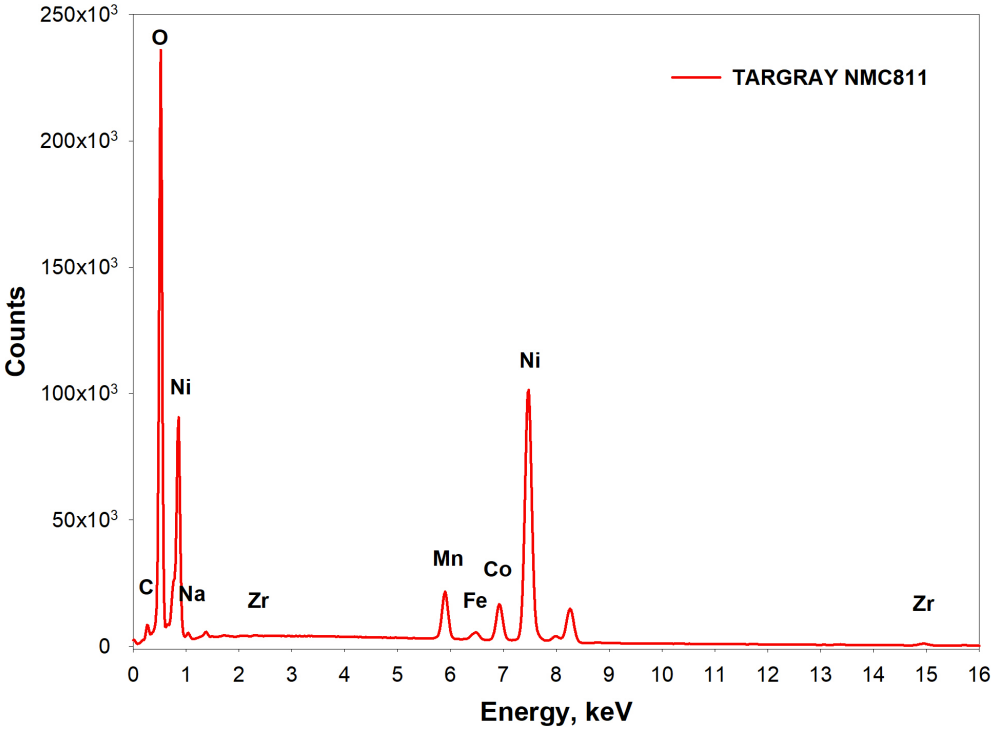

Figure 3.7: The EDX spectrum of NMC811 material from Targray.

EDX was also used to determine the weight percentages of mapping elements in TARGRAY NMC811 powder, as shown in (Table 3.2.

O / wt.%	**Ni/ wt.%**	**Mn/ wt.%**	**Co/ wt.%**	**Fe/ wt.%**	**Zr/ wt.%**
35.27	51.93	5.18	6.46	0.22	0.15

Table 3.2: EDX analysis of the weight percentages of mapping elements in NMC811 powder from Targray.

According to the above table, O, Ni, Mn, and Co are the most abundant elements in NMC811. Differences in contrast in Figure 3.6 and differences in intensities of these elements' peaks in Figure 3.7 represent their weight content levels. These metal compositions were utilized to validate the elemental ratio between Ni, Mn, and Co, and therefore to confirm the kind of CAM; the powder has a Ni:Co:Mn ratio of 0.817:0.082:0.102, respectively. The fact that the weight percentage of Zr is less than that of the evidentiary impurity content of Fe in PDS [136], which is 0.15 % and 0.22 %, respectively, may conclude that the Zr concentration in TARGRAY NMC811 powder consists only of trace amounts. The weight percentage acquired from EDX analysis of the three main metals present in TARGRAY NMC811 (Ni, Mn, and Co) as well as the defect Zr will be compared to the weight percentage obtained from subsequent MP-AES result (Section 3.1.4).

3.1.4 Quantitative Elemental Analysis of Pristine CAM by MP-AES

The metal compositions of the TARGRAY NMC811 are constructed from the digestion of powder (Section 2.3) followed by MP-AES analysis (Section 2.6.4). The calculated weight fractions of Ni, Co, and Mn are 45.43 %, 5.52 %, and 5.43 %, respectively. The presence of these three metals is similar to the weight percent of pristine NMC811 in the PDS [136] (Ni = 47.5%, Co = 5.72%, and Mn = 5.5%). In addition to Ni, Mn, and Co, Li is abundant with a weight fraction of 6.67 %, whereas the Zr trace has a weight fraction of 0.17 %.

It is essential to quantify the content of Zr and Li in TARGRAY NMC811 powder before and after the surface modification in order to confirm the success of coating method and determine the zirconium contents of the LZO-coated NMC811 samples.

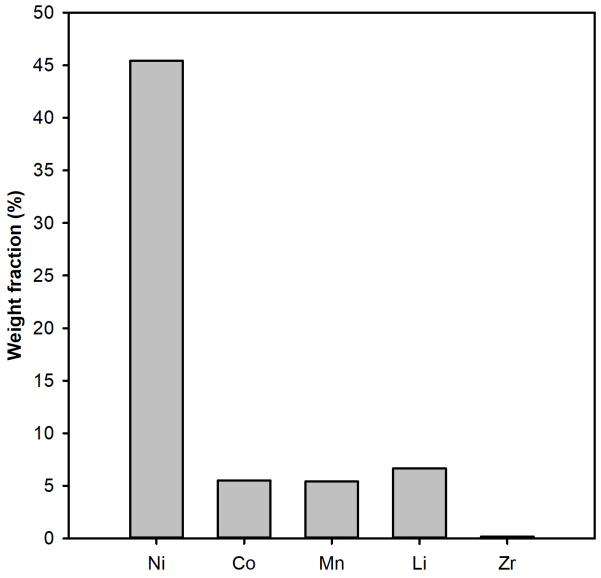

Figure 3.8: MP-AES analysis of the weight percentage of metals in NMC811 powder from Targray.

Based on the composition of metal in TARGRAY NMC811 powder shown above, the metal ratio of the CAM can be determined. CAM is often classified by the weight percent of the constituent metals, such as NMC-111 ($Ni_{0.1}Mn_{0.1}Co_{0.1}$). The weight fractions of Ni, Mn, and Co in TARGRAY NMC811 as determined by MP-AES and EDX analyses are shown in Figure 3.9a and Figure 3.9b, respectively. The microwave digestion of CAM powder in aqua regia is used for the MP-AES analysis, while a dry fraction of the same powder is used immediately for qualitative elemental EDX analysis by S(T)EM. According to MP-AES analysis, CAM is classified as $Ni_{0.806}Co_{0.098}Mn_{0.096}$. The related EDX analysis provides a ratio of $Ni_{0.817}Co_{0.082}Mn_{0.102}$; the findings are consistent. Both calculated ratio could confirm the PDS of TARGRAY NMC811 [136] ($Ni_{0.812}Co_{0.098}Mn_{0.095}$), however MP-AES results are more sensitive. An MP-AES have been reported to have high sensitivity with detection limits down to sub ppb levels [138]. Minor differences in weight percentage results between two methods may result from different sample processing in each method. For the digested sample, minimal metal loss during preparation (weighing, transferring) is probable. Concerning the solid sample for EDX, only a small amount of powder is used, and it is reasonable to assume that the grain size could be affecting the measurement and that a small fraction of powder might not be able to represent the whole TARGRAY NMC811 because of the nonuniformity.

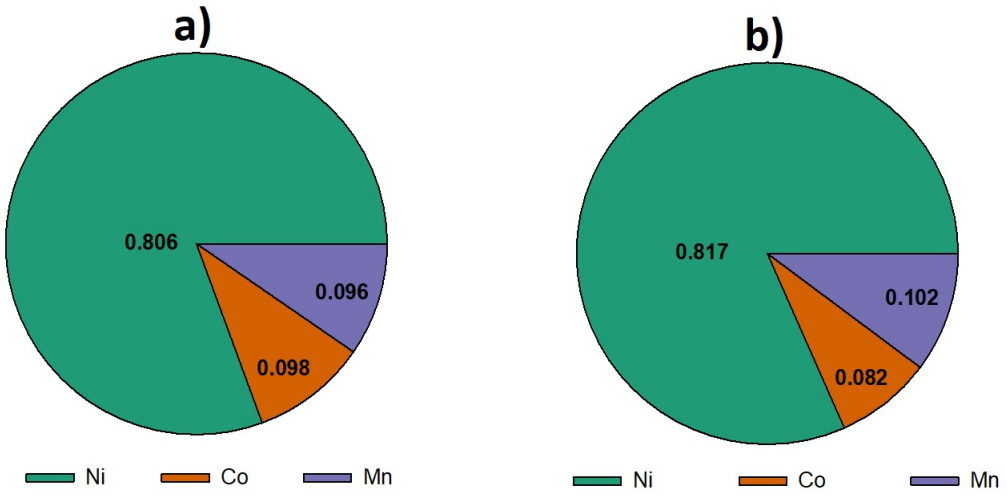

Figure 3.9: The weight percentage of Ni, Co and Mn in TARGRAY NMC811 powder from a) MP-AES b) EDX.

3.2 Surface Modification of Cathode Active Materials

As mentioned in the aims of the work (Section 1.7), the primary goal of this thesis was to develop an efficient coating process that not only enhances the electrochemical performance of Ni-rich NCM-based cathodes but also gets them one step closer to commercialization. This section will describe the mechanism of the designed wet coating process and provide the results of the morphology, crystallinity phase, and composition of the LZO coating layer based on XRD, S(T)EM, EDX, and MP-AES analysis in comparison to the pristine CAM, TARGRAY NMC811. In addition, various process factors that influence the final coating layers were identified and addressed.

3.2.1 Wet Coating Processes for The Surface Modification

In Section 2.1, the experimental steps of three wet coating methods designed for this work are presented in detail. The flow diagrams (Figure 3.10) provide a possible process occurring in the first two LZO sol-gel coating methods. The mechanism and chemical reactions in the processes of these two coating methods have been proposed:

Zirconium and lithium precursors were added to the alcoholic solution for the formation of nanometer-sized colloidal solid particles (Sol). As a result of the alcoholysis process, ZrO^{2+} and Li^{+} are are introduced at this stage:

$$ZrO(NO_3)_2 -> ZrO^{2+} + {NO_3}^{-} \tag{3.1}$$

$$CH_3COOLi -> Li^{+} + CH_3COO^{-} \tag{3.2}$$

Colloidal particles in the solvent combining with many polar groups (OH^{-}) in absolute ethanol, which may, to a certain extent, function as nanoreactors to serve as a template and stabilize nanocrystals, resulting in the formation of the wet Gel [121]. Furthermore, when TARGRAY NCM811 powder was added to the reactor, OH^{-} could spontaneously bond to the surface of NCM811 particles, and ZrO^{2+} and Li^{+} colloidal particles could adsorb on NMC811 via hydrogen-bonding interactions with groups OH^{-} groups [109].

After 24 hours of mixing, the solution was evaporated at 90 °C while being stirred vigorously in the fume hood until all of the solvent was gone. By evaporating in this approach, nanocrystal

precursors containing Zr and Li are transformed into xerogels that bond to the surface of TAR-GRAY NMC811 [121, 139]. The samples were put in a vacuum drying oven at 50 degrees Celsius for 12 hours, at which point the aging process occurred to enhance the structural integrity and mechanical properties of xerogels [139]. Following completion of the grinding process, the samples were subjected to a final heat treatment using calcination. he precursor on NMC811 becomes Li_2ZrO_3 as a result of air calcination:

$$2Li^+ + ZrO^{2+} + O_2 - > Li_2ZrO_3 \tag{3.3}$$

Because nanocrystals have a very high surface energy, the transformation from the precursor to LZO might proceed at a very low temperature in calcination [121]. While Method 1 was designed with the optimal heating temperature for LZO coatings (650 °C for 5 hours), which was used in the majority of studies [108, 114, 140], mMthod 2 was developed with conditions for pre-heating at 400 °C for 5 hours and then heating at 800 °C for 15 hours based on Schipper et al. [141] finding that significant Zr doping occurred in ZrO_2-coated NMC811 prepared with a similar wet chemical coating process. Schipper et al. concluded that the Zr^{4+} residing in the bulk may stabilize the layered structure and improve cell performance.

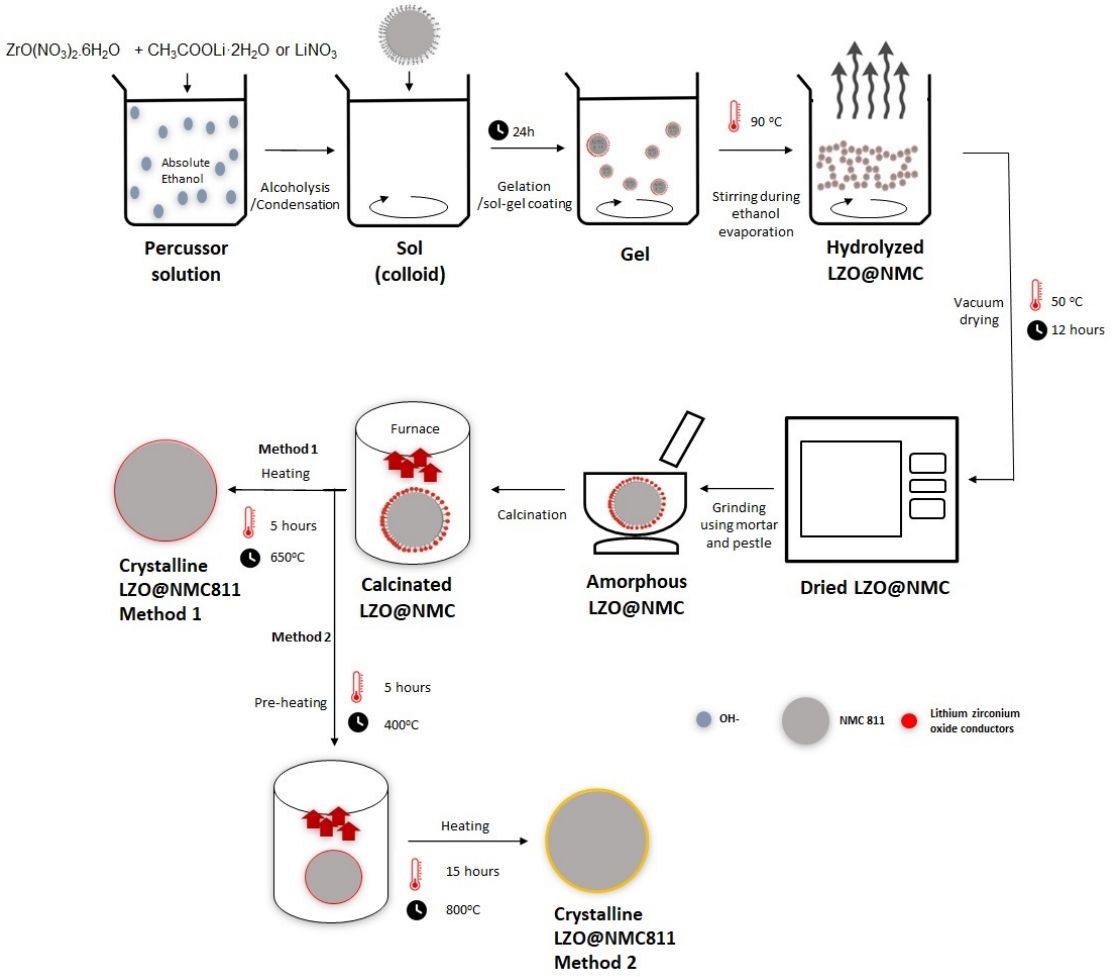

Figure 3.10: The flow diagram illustrating the process of the LZO sol-gel coating Method 1 and Method 2

Method 3 was designed to modify the condition of evaporation in Method 1. The process is similar to the first two, except that the solvent was removed from the system as a gas by heating wet gel in a closed space without stirring at a controlled temperature (90 °C) and pressure (-0.1 MPa). This drying method is similar to the "supercritical method," which was used to transform wet gel to aerogel. However, the temperature and pressure of the vacuum oven were not adjusted to meet

the critical conditions of absolute ethanol that the liquid trapped in the pores of the gel [139]. Instead, the samples were completely dried before the calcination conditions stated in Method 1 were applied. This method was made to protect NMC811 from humidity in the air during solvent evaporation, which methods 1 and 2 were not able to do. The effects of humidity on Ni-rich CAM have been reported by Jung et al. [142] who investigated the accumulation of impurities on the surface of NMC811 for up to one year of storage at room temperature. Using XPS and Raman spectroscopy, Jung et al. has found a 5-fold rise in carbonate species on the surface of NMC811, leading to a subsequent deterioration in electrochemical performance.

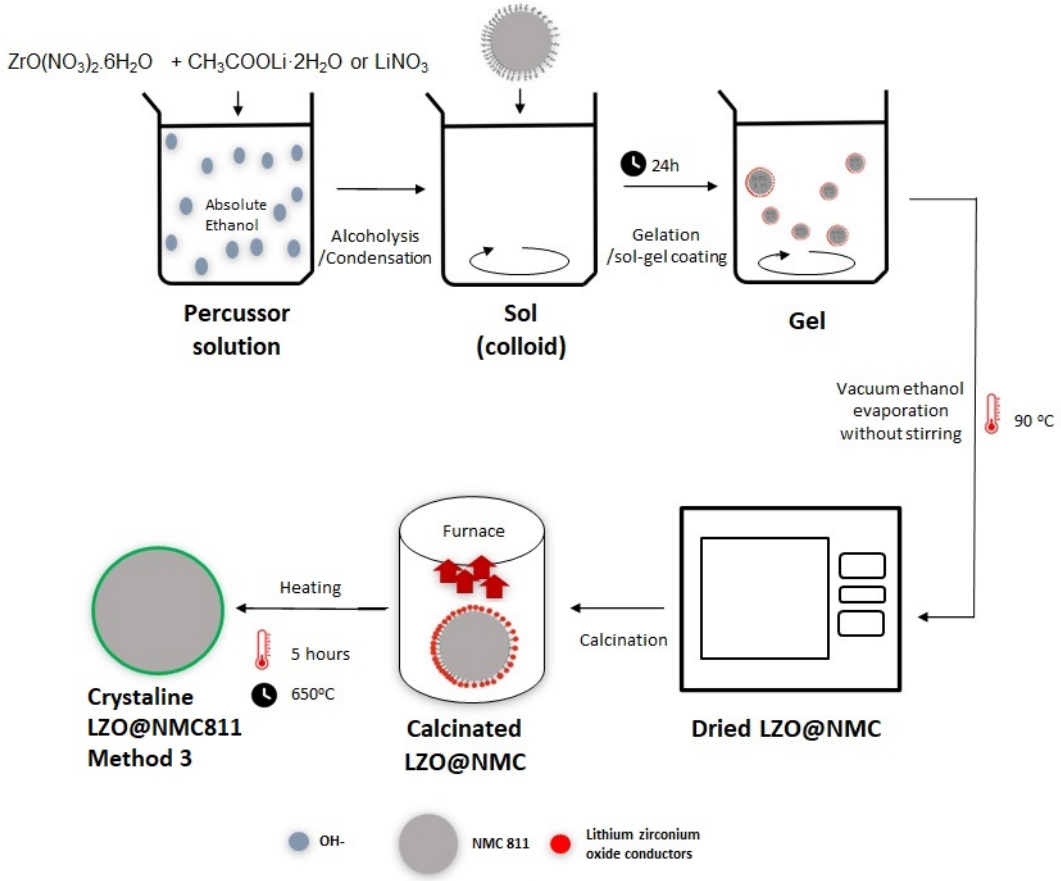

Figure 3.11: The flow diagrams illustrating the process of the LZO coating Method 3.

In addition, findings that will be discussed in more detail in the next sections show that the conditions of evaporation are important for the formation of a uniform LZO coating layer. In order to validate the reproducibility of the aforementioned methods, various concentrations of precursors were utilized in each method to coat different weight contents of LZO (from 0.5 wt.% to 9 wt.%) on TARGRAY NMC811. In the following sections, how process modifications influence the phase identification and final form of LZO coating layers will be discussed.

3.2.2 Phase Identification of LZO coated Cathode Active Material

Figure 3.12(a1) and Figure 3.12(b1) show the X-ray diffraction patterns of TARGRAY NMC811 before and after LZO surface coating using Method 1 and Method 2, respectively, with $CH_3COOLi{\cdot}2H_2O$ as the precursor. In addition, the (003) and (104) peaks in the regions 17 – 20° and 43 – 46°, respectively, of all LZO-coated NMC811 samples hardly shift when compared to the commercial CAM, suggesting that there may have been no chemical reaction between TARGRAY NMC811 and LZO during the coating process [143]. It may also imply that Zr atoms are not embedded in the lattice structure of bulk materials [143]. On the surface of the 0.5 wt.% coated sample by

Method 1 and the 1 wt.% coated sample by both methods, the diffraction peaks of LZO can not be found, probably because the LZO films are too thin to be detected. However, when the coating content increases to 2 wt.% and 3 wt.%, the diffraction patterns of LZO-coated NMC811 display the LZO peaks, as the number of LZO particles grows. When the X-ray diffraction patterns of both methods are magnified from 41 to 43 degrees (Figure 3.12(a2) and Figure 3.12(b2)), the (0 2 0) plane of LZO (PDF No. 00-041-0324) is visible at 42.34 degrees.

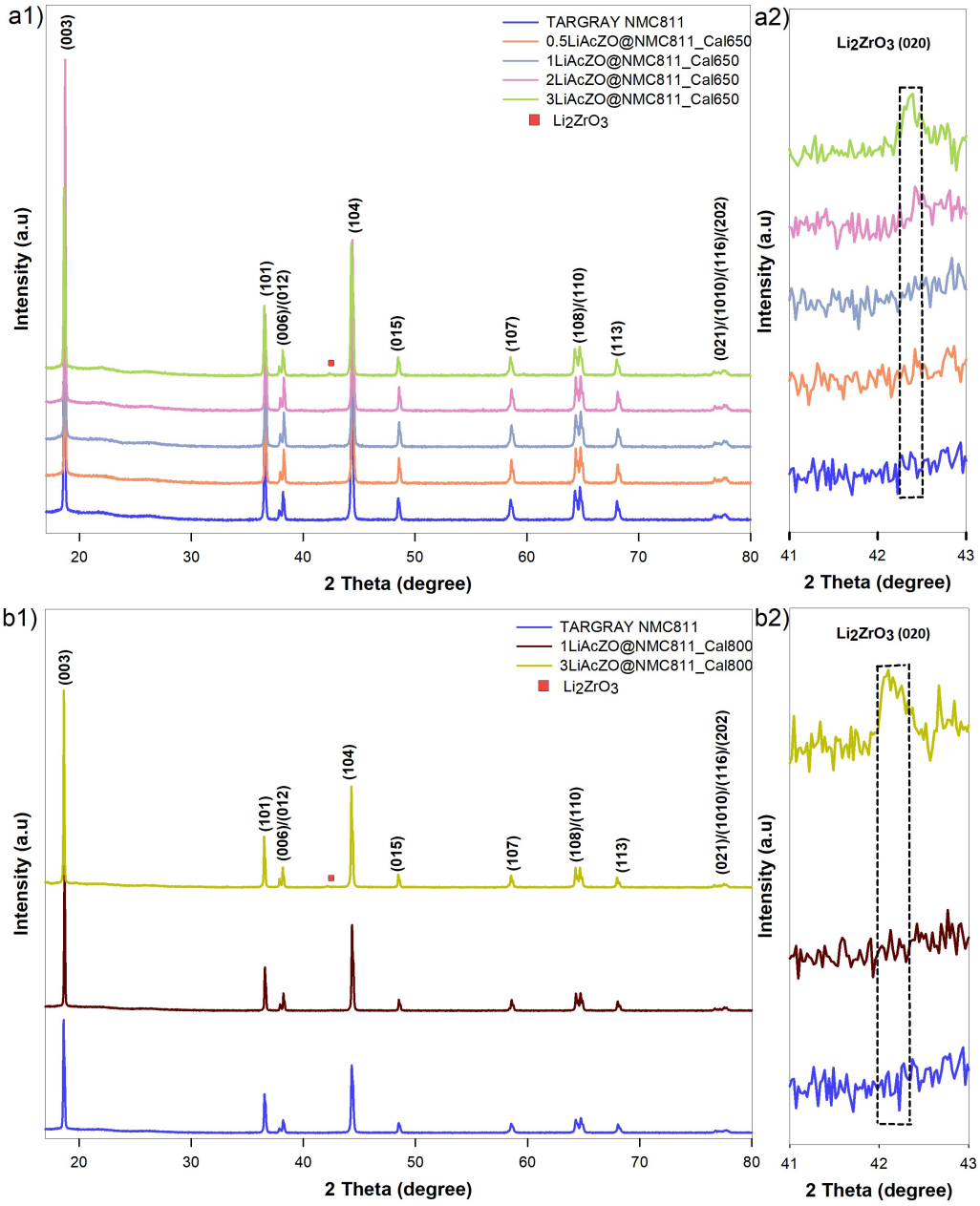

Figure 3.12: a1) XRD patterns of TARGRAY NMC811 and LZ0-coated NMC811 using lithium acetate as the precursor for Method 1. a2) Diffraction peaks of LZO found in coated samples using $CH_3COOLi{\cdot}2H_2O$ as the precursor for Method 1. b1) XRD patterns of TARGRAY NMC811 and LZ0-coated NMC811 using lithium acetate as the precursor for Method 2. b2) Diffraction peaks of LZO found in coated samples using $CH_3COOLi{\cdot}2H_2O$ as the precursor for Method 2.

The lattice parameters of all samples are included in Table 3.3, they were computed using Topas Software by fitting the peak location to an R-3m space group. All six samples exhibit high c/a

and I(003)/I(104) ratios, this may indicate that the cathodes coated with LZO have maintained low cation mixing in compliance with TARGRAY NMC811 (Table 3.1). For method 1, it was observed that the I(003)/I(104) ratios grew from 0.5 wt.% to 2 wt.%, or 1.7725 to 1.9788 until they decreased to 1.3838 at 3 wt.%. Yang et al. [114] also discovered a similar trend in the Li/Ni mixing degree. All cathodes have delivered a low I(006)+I(102))/I(101) ratio, indicating that the as-prepared samples may have a good hexagonal ordering. The values of the lattice parameters did not change much after LZO coating, and the c/a ratio hardly changed. Even 3 wt.% LZO-coated NCM811 exhibited little change, indicating that the LZO modification of the surface of NCM using an absolute ethanol solvent may reduce the danger of structural change in the coated object when coating water-sensitive materials. This also suggests that the LZO may stay on the surface of cathode active materials rather than being incorporated into the structure of the host.

Sample	a	c	c/a	$I_{(003)}/I_{(104)}$	$I_{(006)} + I_{(012)}/I_{(101)}$
0.5LiAcZO@NMC811_Cal650	2.8745	14.2067	4.9423	1.7725	0.6508
1LiAcZO@NMC811_Cal650	2.8743	14.2083	4.9432	1.9238	0.4070
2LiAcZO@NMC811_Cal650	2.8745	14.2088	4.9430	1.9788	0.6625
3LiAcZO@NMC811_Cal650	2.8761	14.2181	4.9435	1.3838	0.7195
1LiAcZO@NMC811_Cal800	2.8782	14.2198	4.9405	1.6543	0.7222
3LiAcZO@NMC811_Cal800	2.8782	14.2182	4.9399	1.8916	0.7373

Table 3.3: Lattice parameters of LZO-coated NMC811

Figure 3.13a depicts the X-ray diffraction patterns of TARGRAY NMC811 and LZO-coated NMC811 samples using Method 3 with $LiNO_3$ as the precursor. Similar to Method 1 and Method 2, there is no LZO diffraction peak in 1 wt.% coated samples, presumably owing to the low coating concentration, and there is also no peak shifting in the ranges of 17 - 20 and 43 – 46 degree. However, the crystalline phase of the LZO is also seen in the XRD pattern of 3LiNiZO@NMC811_Cal650 and is clearly observed in excessive 6 wt.% and 9 wt.% LZO-coated NCM811 samples. The partial amplified curves of 3 wt.%, 6 wt.% and 9 wt.% LZO-coated NMC811 are shown in Figure 3.13 (b - d). It could be seen that the intensities of LZO peaks increase with coating layer thickness, and a similar trend was seen in Figure 3.12(b1) and Figure 3.12(b2). But when X-ray diffraction patterns are magnified from 41 to 43 degrees, the LZO peaks move slightly to a higher angle. This may indicate that a distinct crystalline structure of the coating layer was created. And the use of a different lithium precursor in this method may be the cause, as will be explained later. Compared with methods 1 and 2, the (0 2 0) peaks of LZO shifted from 42.34 to 42.6. In addition, there are two weak diffraction peaks at 35.85 (112) and 39.9 (004) degrees detected in excessively coated NMC samples that correspond to LZO (PDF No. 00-041-0324).

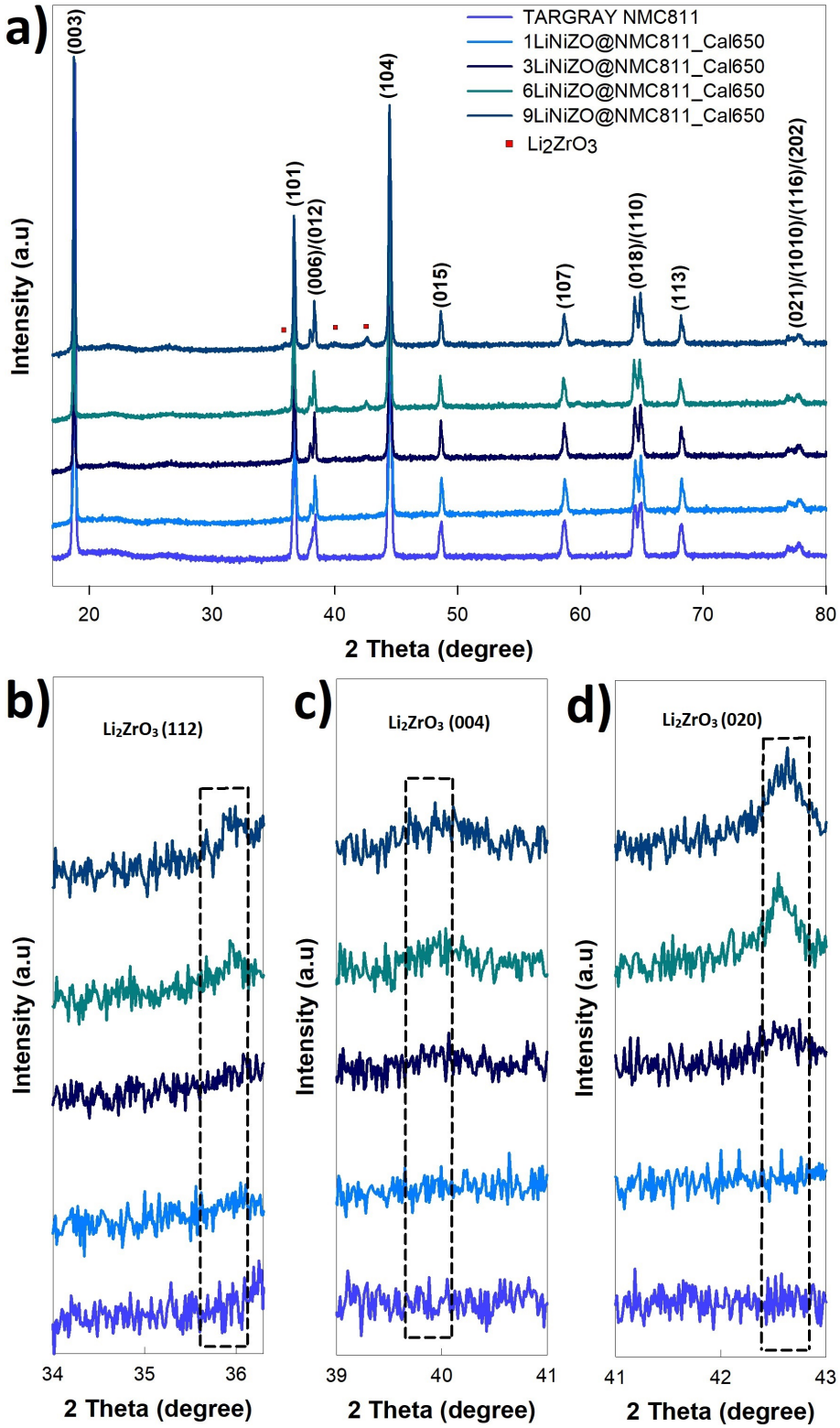

Figure 3.13: a) XRD patterns of TARGRAY NMC811 and LZ0-coated NMC811 using $LiNO_3$ as the precursor for method 3. b), c) and d) Diffraction peaks of LZO found in coated samples using $LiNO_3$ as the precursor for Method 3.

The high cation mixing is observed in all LiNiZO@NMC811_Cal650 samples. As shown in Figure 3.14, the I(003)/I(104) of the samples synthesized by Method 3 are 1.0517, 1.2217, 1.1348, and 1.1575 for the samples of 1LiNiZO@NMC811_Cal650, 3LiNiZO@NMC811_Cal650, 6LiNiZO@NM

C811_Cal650, 6LiNiZO@NMC811_Cal650 respectively. All samples are less than 1.2, with the exception of the 3LiNiZO@NMC811_Cal650 sample. The Li/Ni mixing degrees in method 3 samples are much lower than samples in Method 1 and Method 2. The significant cation mixing might be attributed to the non-uniformity of the LZO coating layer, which will be discussed in details a subsequent section.

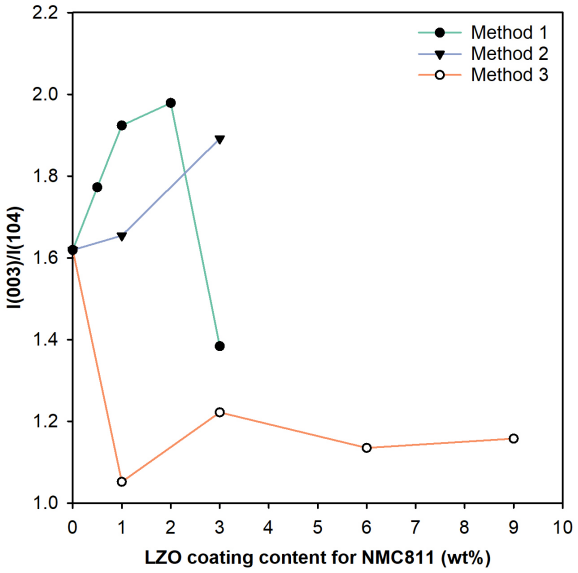

Figure 3.14: Variation of the I(003)/I(104) with different LZO content and method for NMC811.

As shown in Figure 3.13 (c - d), the XRD peaks of LZO in the Method 3 using $LiNO_3$ as the precursor have a slight shift to a higher angle than the XRD peak of LZO in the methods using $CH_3COOLi{\cdot}2H_2O$ (Figure 3.12(a2) and (b2)). According to the majority of research [141, 144], the calcination environment is principally responsible for the phase transformations in the crystal structures of LZO. Although Method 2 used a pre-heating step at 400 °C for 5 hours followed by a heating step at 400 °C for 15 hours, which is different than Method 3. However, Method 1 and Method 3 used identical calcination conditions (600 °C for 5 hours in air), and samples were completely dried prior to calcination in all methods. The mechanisms of the coating process for these three methods are described in Section 3.2.1. This could mean that the different crystalline phase structure of the coating layer is more likely caused by the use of different lithium precursors in the coating process. $CH_3COOLi{\cdot}2H_2O$ has been widely used with $ZrO(NO_3)_2.6H_2O$ or $Zr(NO_3)_4$ in the sol–gel method to coat LZO on CAM [114, 140, 108], but $LiNO_3$ has been reported infrequently. To account for differences in the crystallinity of coating layers between lithium precursors, high-magnification S(T)EM images (Figure 3.15) compare the morphology of 3 wt.% LZO-coated TARGRAY NMC811 prepared by (a) $CH_3COOLi2H_2O$ (3LiAcZO@NMC811_Cal650) and (b) $LiNO_3$ (3LiAcZO@NMC811_method 1) using the same coating process of Method 1. The material and method for these experiments have been described in Section 2.1.

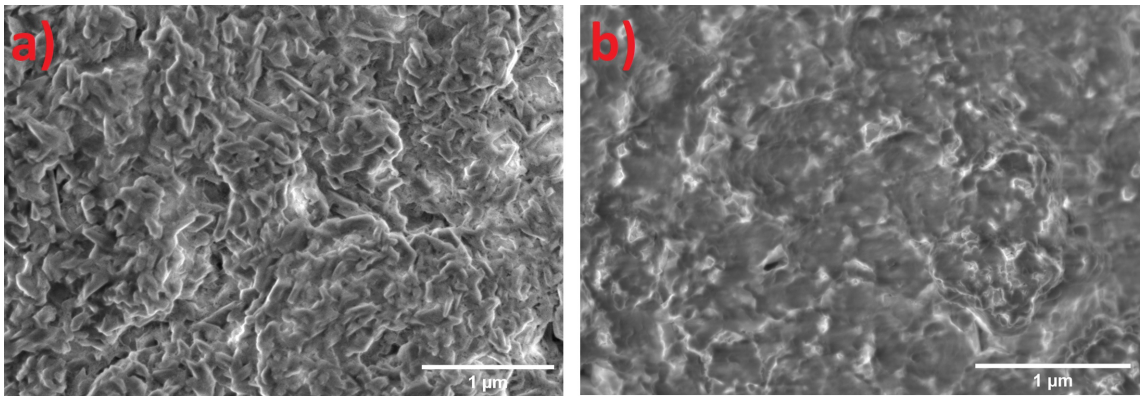

Figure 3.15: S(T)EM images at high magnification in SE mode of TARGRAY NMC811 after surface modification with 3 wt.% LZO using Method 1 with a) $CH_3COOLi2H_2O$ and b) $LiNO_3$ as the precursor.

The crystal structures of the two coating layers could be seen to be very different. EDX mapping revealed Zr atoms on the surfaces of both coating materials, as will be shown and discussed in the next section.

3.2.3 The Evidence of an Uniform LZO Coating Layer and Increased Coating Content Effects on TARGRAY NMC811

Method 1's final CAM products have the most uniformly LZO-coated TARGRAY NMC811. They were chosen as representative examples to show how the microstructure of TARGRAY NMC811 changes after surface modification and how it changes as the amount of LZO coating increases. Using Method 1, high-magnification S(T)EM images were utilized to evaluate the morphology of the LZO coating on the TARGRAY NMC811. The morphological changes in TARGRAY NMC811, 0.5LiAcZO@NMC811_Cal650, 1LiAcZO@NMC811_Cal650, 2LiAcZO@NMC811_Cal650, and 3LiAcZO@NMC811_Cal650 are compared in high-magnification S(T)EM images of Figure 3.16 (10100 nA of emission current and 1 kV of accelerating voltage), respectively. The morphology of the secondary and primary particles of as-received NMC811 from Targray prior to coating has been described in Section 3.1.2 and will be used again for ease of comparison. In general, the uncoated particles seem to have clean surfaces and aculeated edges prior to coating, despite the presence of traces (Figure 3.16).

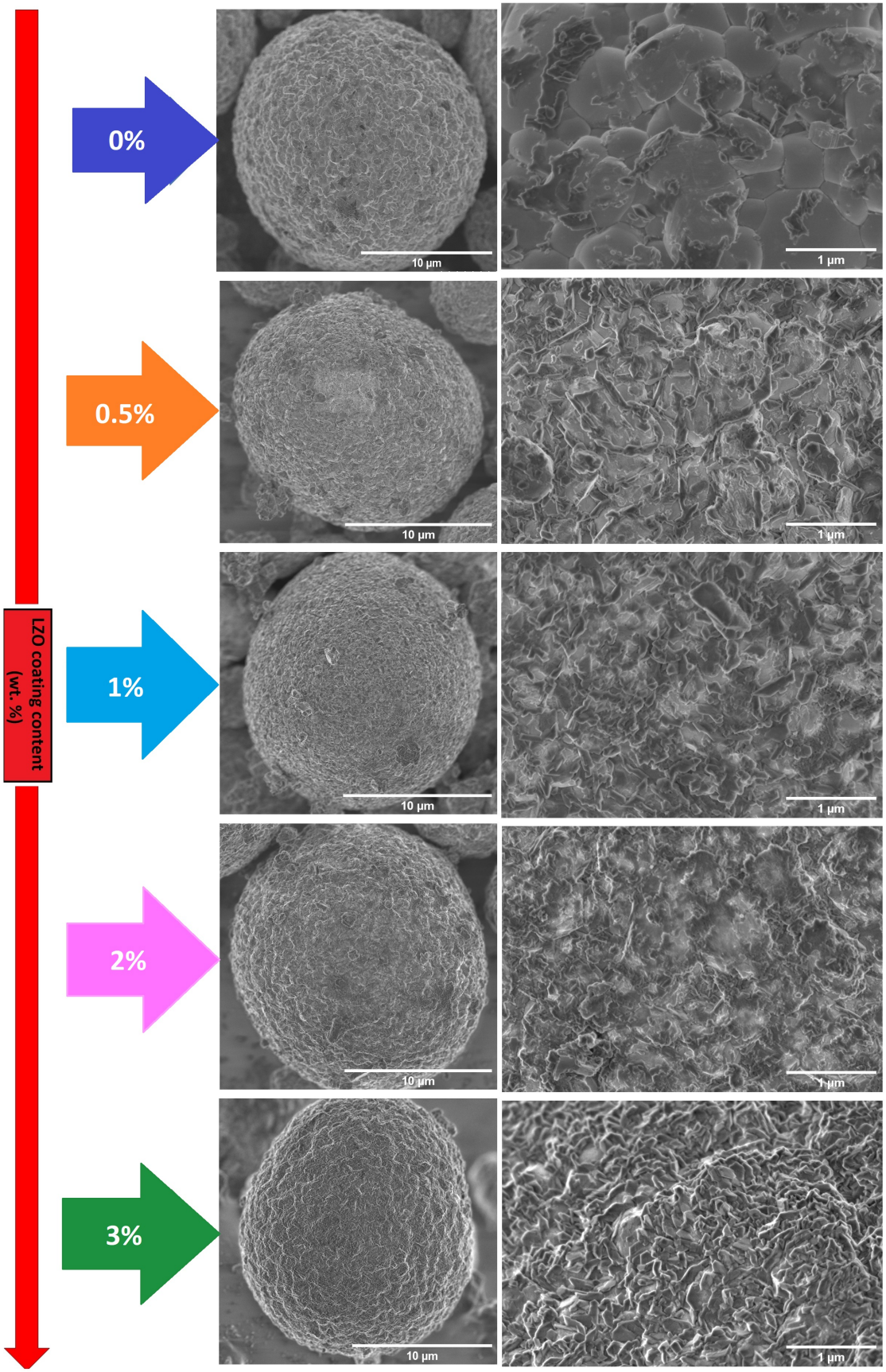

Figure 3.16: High-magnification S(T)EM images in SE mode of TARGRAY NMC811 and TARGRAY NMC811 coated with 0.5 wt.%, 1 wt.%, 2 wt.%, and 3 wt.% LZO using Method 1. The magnification increases as one moves from left to right.

The coated samples retain their spherical shape and are composed of many primary nanoparticles. But when compared to uncoated TARGRAY NMC811, the surface of all LZO-coated NMC811 secondary particles gets rougher as the coating content rises. In the case of a sample coated with 0.5 wt.% LZO, the magnified image reveals fuzzy surfaces and edges, and the primary particles are less defined. It could be seen that the coating material covered the neck region created by grain contact or the grain boundary, suggesting that LZO had been coated to the surface of materials [108]. As the coating quantity rises to 1 wt.% and 2 wt.%, the coating layer thickens and gets denser, and the grain boundaries between the primary particles become difficult to identify. In the maginfied picture of 3LiAcZO@NMC811_Cal650, almost the whole surface of the particle was covered with LZO nanoparticles, and the grain boundaries were no longer apparent, indicating that 3 wt.% LZO by mass of NCM is an excessive amount of LZO coating content. The excessive nanoparticle modification may relieve the interfacial resistance, but it may also prevent the transfer or diffusion of lithium ions. This is due to the fact that the sulfide-based solid electrolyte may permeate into the primary interparticle space [145].

The analysis of the uniformity of element distribution using EDX was performed on the same 2 wt.% and 3 wt.% of LZO-coated particles that were discussed above and depicted in Figure 3.17(a) and Figure 3.17(b), respectively.

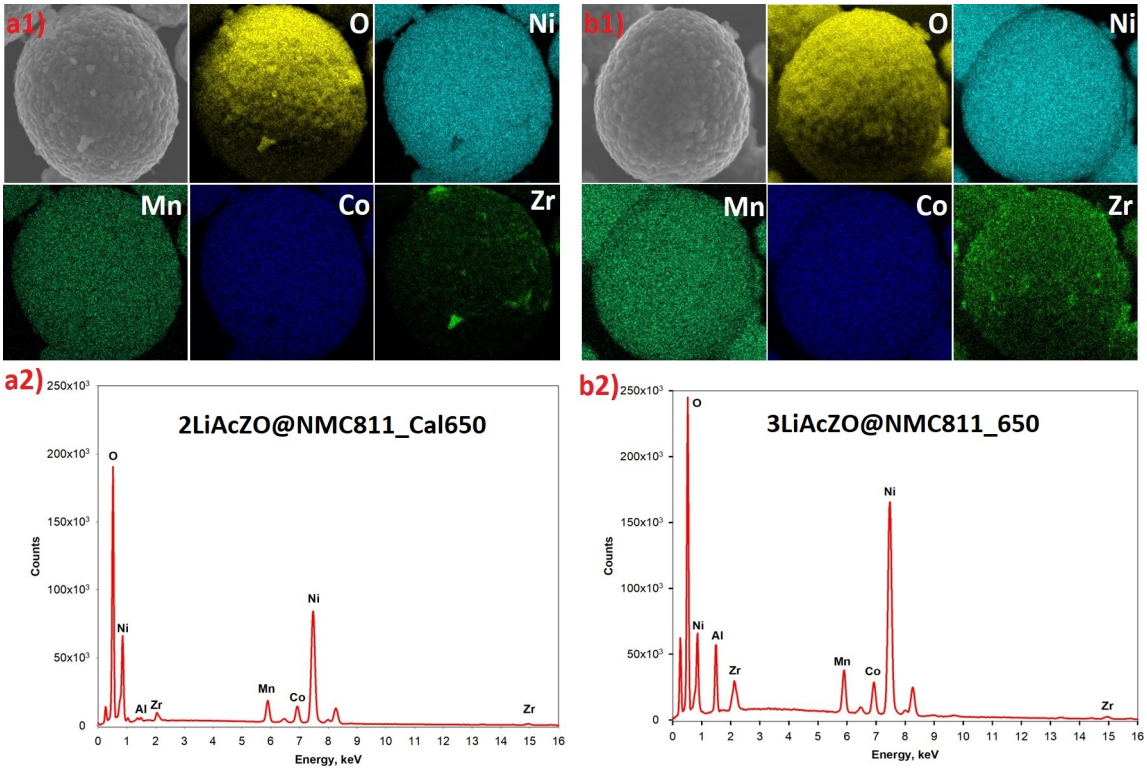

Figure 3.17: EDX mapping of O, Ni, Mn , Co and Zr and EDX spectra on the surface of a) 2 wt.% and b) 3 wt.% LZO-coated NMC811 using Method 1.

The Zr element is distributed extremely uniformly on the surface of the 3LiAcZo@NMC811 microspheres (Figure 3.17(a1)) and quite homogenously on the surface of the 2LiAcZo@NMC811 microspheres (Figure 3.17(b1)). An increase in the coating content causes a corresponding rise in the dot density of Zr in it's elemental mappings [108]. This homogeneous distribution, acting as a protective layer, would significantly improve the cycling and rate performances of NMC811 which will be discussed in the cell performance section. Compared to Figure 3.6, the Ni, Co, and Mn elements remain uniformly distributed on the surface of coated TARGRAY NMC811. As shown in Figure 3.17(a2) and Figure 3.17(b2) the Zr peaks are found in the EDX spectrum of 2LiAcZO@NMC811_Cal650 and 3LiAcZO@NMC811_Cal650, respectively. Compared to the spectrum of uncoated TARGRAY NMC811 in Figure 3.7, the Zr peaks are more visible, and their peak intensities rise with the mass percentage of the coating layer. It should be noted that the

EDX spectrum of the 3 wt.% LZO-coated sample has revealed an intense rise in Al atoms. This could be because of the way samples were collected after the calcination process. An Al cruciblbe and stick was used to collect all the calcined materials. The coating materials produced using $CH_3COOLi.2H_2O$ appear to have a different crystal structure than the LZO coating layers prepared using $LiNO_3$ as the lithium precursor, as discussed in Section 3.2.2. The high-magnification S(T)EM images of the TARGRAY NMC811 particle after its surface was modified using Method 1 and $LiNO_3$ are shown in Figure 3.18.

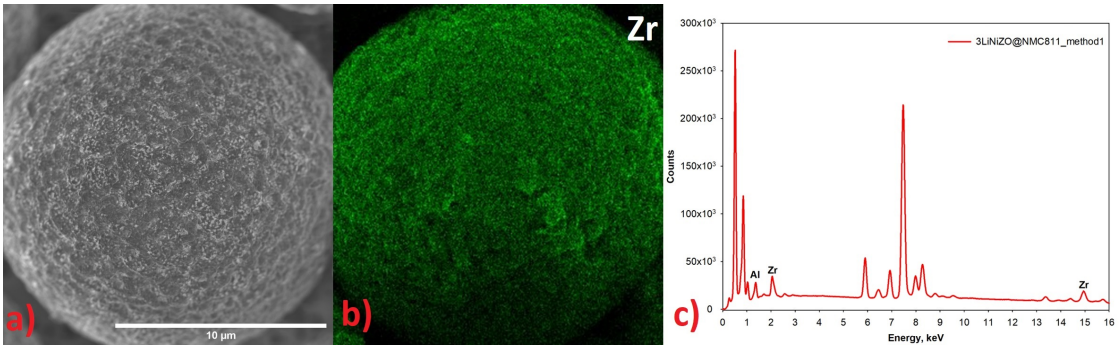

Figure 3.18: a) High-magnification S(T)EM image in SE mode, b) EDX mapping of Zr and c) EDX spectrum of 3LiNiZO@NMC811_method1.

It was observed that NMC811 is uniformly coated, and further Zr elemental mapping, as seen in Figure 3.18(b), could support this conclusion. High Zr atom peak intensities in the EDX spectrum, as illustrated in Figure 3.18(c), indicate that the particle may be coated with an excessive amount of Zr. Note that the intensity of the Al atom in the EDX spectrum of 3LiNiZO@NMC811_method1 is less than that of the Al atom in the EDX spectrum of 3LiAcZO@NMC811_Cal650 (Figure 3.17(b2)). This is owing to the fact that the experiment was conducted at the very end and with the caution of not contact the Al crucible excessively when collecting calcinated materials. Although the crystal structure of two LZO covering materials synthesized from distinct lithium precursors has not been identified, it will not be identified as part of the thesis's outcomes. However, based on the results above, the coating process that was designed for Method 1 has shown its reproducibility and effectiveness in creating a uniform coating layer utilizing different types of precursors.

MP-AES was measured to further indicate the Zr mass ratio in all coated samples using Method1 with $CH_3COOLi_2.2H_2O$ as the precursor, as shown in Figure 3.19.

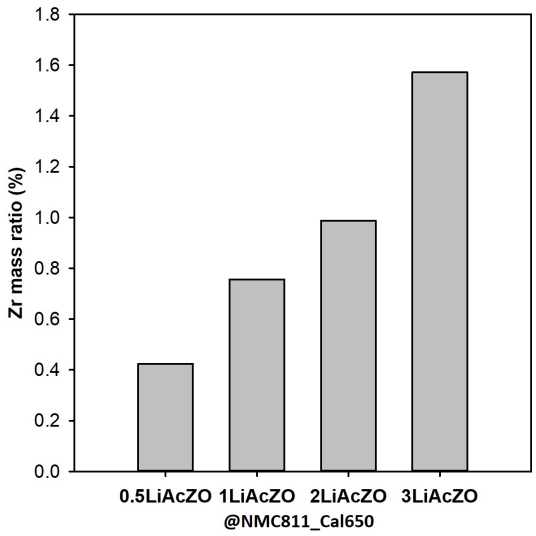

Figure 3.19: Zr mass ratios measured by MP-AES in all LZO-coated samples using Method 1.

MP-AES measurements indicate that the Zr mass ratio is 0.42 wt.%, 0.76 wt.%, 0.99 wt.% and 1.57 wt.% in 0.5LiAcZO@NCM811_Cal650, 1LiAcZO@NCM811_Cal650, 2LiAcZO@NCM811_Cal650 and 1LiAcZO@NCM811_Cal650 respectively. These findings could explain the increase of Zr dot densities in the Zr elemental mappings and the increase of Zr peak intensities in EDX spectra of the LZO-coated sample from a low to an excessive LZO coating content.

An elemental mapping of Zr was performed on the cross section of a large secondary particle using S(T)EM-EDX to further investigate the uniformity of the surface coating layer and the doping effect at the annealing temperature of 650 °C, as shown in Figure 2.1. It should be noted that in most studies, S(T)EM-EDX mapping was performed on the surface of nano- or micrometer-sized particles rather than their cross section. However, one difficulty with the surface EDX mapping is that it cannot differentiate between the coating effect and the doping effect. Because the Zr element is rich on the surface of TARGRAY NMC811 in the case of excessive coating content (3 wt.% LZO-coated NMC811 using Method 1), combined with the large size of the secondary particles, cross-section mapping could easily produce a strong contrast of the coating layers in terms of the spatial difference between the surface and bulk. As seen in Figure 3.20, a Zr ring was discovered on the particle surface of the 3LiAcZO@NMC811_Cal650 sample. In addition, the EDX spectrum reveals the presence of Zr, which has the highest dot density gathered on the surface's outermost layer. This could necessitate the formation of a surface Zr-rich phase LZO rather than elemental substitution to generate $Li(Ni_{0.8}Co_{0.1}Mn_{0.1})_{1-x}Zr_xO_3$ due to Zr diffusion. For electrochemical cyclability, coating may be more important than doping because surface sensitivity could be more important than bulk stability.

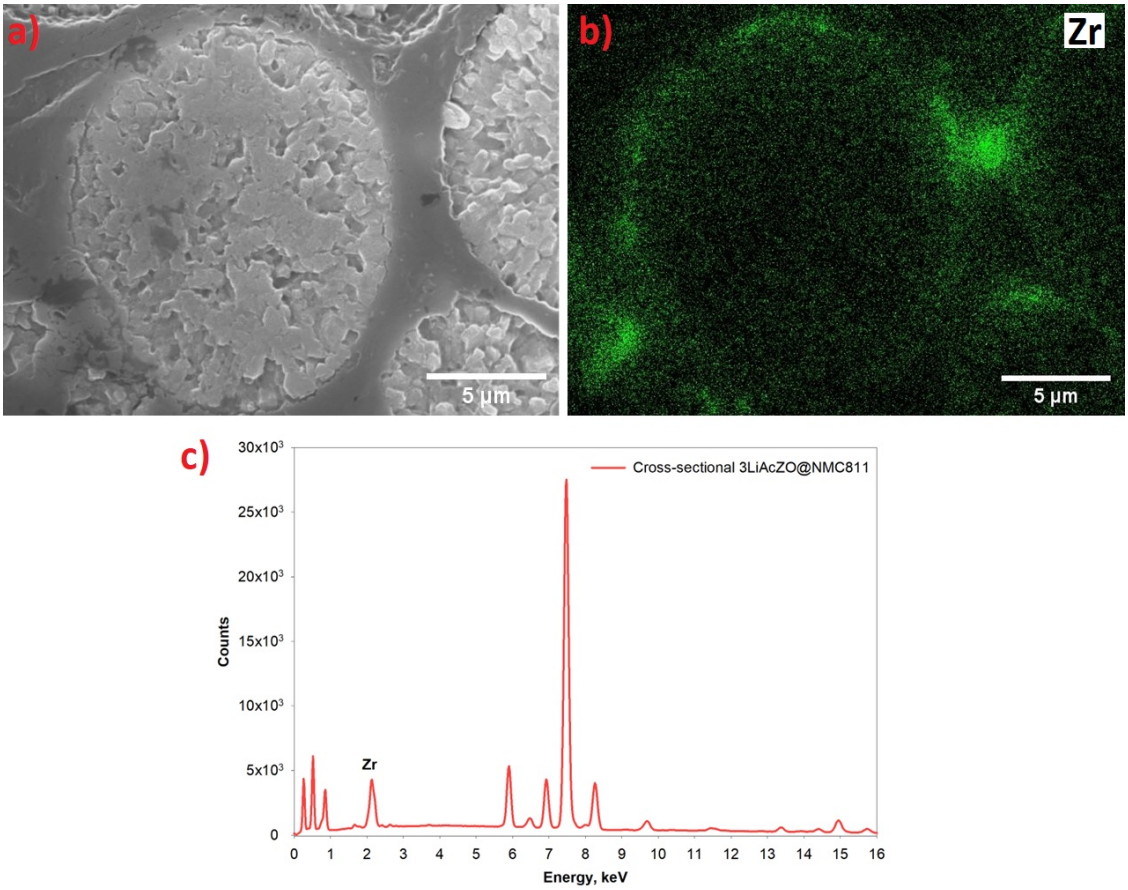

Figure 3.20: a) High-magnification S(T)EM image in SE mode of the 3 wt.% LZO-coated NMC811 particle cross section, b) the corresponding EDX mapping of Zr and c) it's EDX spectrum.

The X-Y distribution of chemical elements on the surface and in the bulk of TARGRAY NMC811 microsphere particles was obtained using S(T)EM in DF mode and line scan EDX analysis.

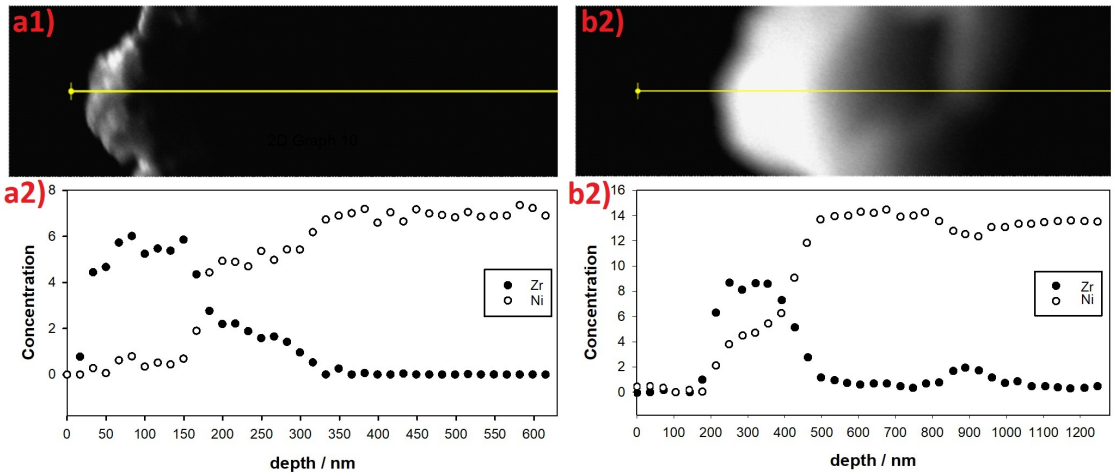

Figure 3.21: S(T)EM images in DF mode showing the areas marked with yellow lines where line EDX analysis was performed, as well as Zr content as a function of distance from the surface of the coated TARGRAY NMC811 particle to its bulk for a) 2 wt.% and b) 3 wt.% LZO-coated NMC811 samples using Method 1.

The working principle of DF mode in S(T)EM has been discussed in Section 2.6.3. The S(T)EM DF image of the 2LiAcZO@NMC811_Cal650 sample and the measuring line scan from the outer surface to more than 800 nm inside the sample's bulk are shown in Figure 3.21(a1). The yellow line scan in Figure 3.21(b1) DF image detected the elemental content in the 3LiAcZO@NMC811_Cal650 sample. Compared to the DF image of uncoated TARGRAY NMC811 (Figure 3.5b) the outer surface contrast of both coated samples differs, indicating that the surface atomic number is distinct, which could be from LZO coating layers. Figure 3.21(a2) and Figure 3.21(b2) display the Ni and Zr contents at the analyzed line (or line scans on a specimen) of the 2 wt.% and 3 wt.% LZO-coated sample using Method 1, respectively. At the surface of both samples, the amount of Zr is high, but it drops off quickly within a few hundred nanometers. This could imply that, in addition to the coating effect, which results in high Zr content on the surface of TARGRAY NMC811 particles, there is a small amount of $Li(Ni_{0.8}Co_{0.1}Mn_{0.1})_{1-x}Zr_xO_3$ formation at the surface's outermost area [107].

BF mode in S(T)EM was used to further demonstrate the distribution of LZO coating layer on TARGRAY NMC811. Figure 3.22a results are displayed for the 2LiAcZO@NMC811_Cal650 sample, whereasFigure 3.22b displays information for the 3LiAcZO@NMC811_Cal650 sample. When compared to the smooth surface without layering phenomenon of uncoated TARGRAY NMC811 (Figure 3.5a), the visible layered structure is observed on the surfaces of both samples.

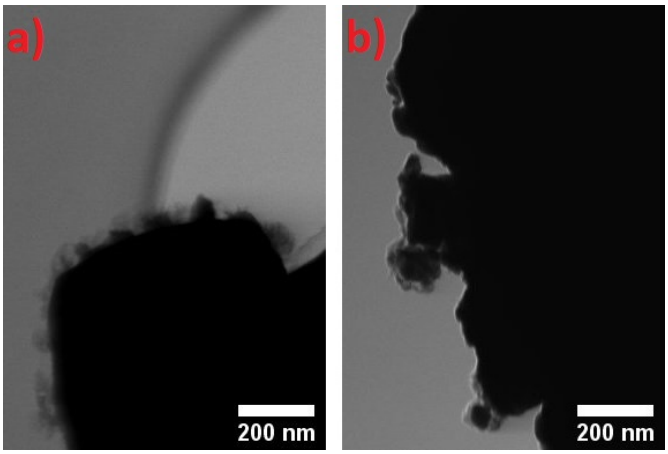

Figure 3.22: S(T)EM images in BF mode of a) 2 wt.% and b) 3 wt.% LZO-coated NMC811 samples using Method 1.

Combining all of these findings in the coated TARGRAY NMC811 using the process in Method 1, we may infer that TARGRAY NMC811 powder has been coated uniformly with varying amounts of LZO coating content.

3.2.4 Increased Annealing Temperature Effects on LZO-coated TARGRAY NMC811

Method 2, as described in Section 3.2.1 was conducted in order to explore the effect of coating atmosphere for LZO on the electrochemical behavior of TARGRAY NMC811. A recent work by Schipper et al. [141] shown that substantial Zr doping occurred when coating NMC811 with LZO and annealing the material at a high temperature ($\geq$ 700 °C). This study served as the inspiration for the development of calcination conditions in Method 2.

The high-magnification S(T)EM images of 1 wt.% and 3 wt.% LZO coated samples using a preheating step at 400 °C for 5 hours followed by annealing at 800 °C for 15 hours are shown in Figure 3.23.

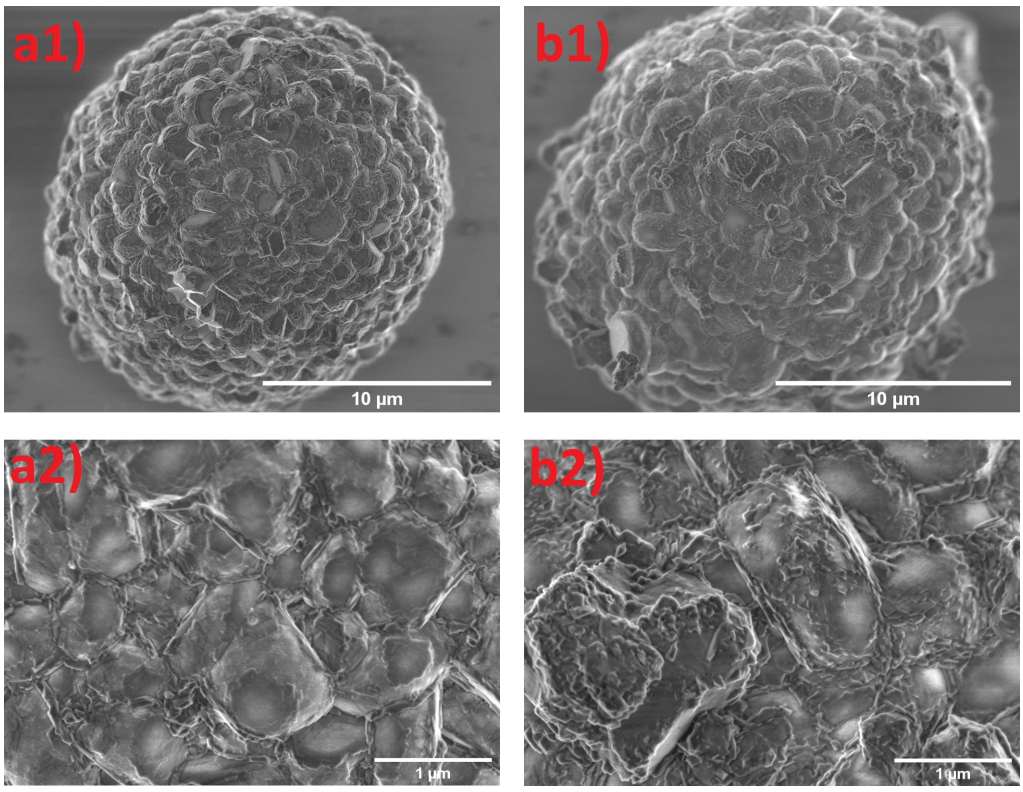

Figure 3.23: High-magnification S(T)EM images of a) 2 wt.% and b) 3 wt.% LZO-coated NMC811 samples using Method 3.

The layer phenomenon was clearly observed on the surface of both LZO-coated samples. Compared to the morphology of the same LZO weight fraction as determined by Method 1, the LZO on 1LiAcZO@NMC811_Cal800 and 3LiAcZO@NMC811_Cal800 obviously show a highly crystalline LZO phase. The transition of LZO into its crystalline phase could be done by raising the calcination heating temperature above the crystallization temperature of the material over an extended period of time [146]. Sato et al. [147] investigated in depth the thermal decomposition behaviors of zirconium hydroxide synthesized from an aqueous solution and reported that a metastable tetragonal zirconium oxide developed about 500 °C. This tetragonal ZrO_2 phase becomes a more stable monoclinic phase with P21/c symmetry as the temperature climbs from 500 to 600 °C.

Notably, the necks of the contact between primary particles in the 3LiAcZO@NMC811_Cal800

sample was still detectable in Figure 3.23b, despite the fact that 3 wt.% is the excessive amount of LZO coating. As shown in Figure 3.16, there is no indication of grain boundaries between primary particles in the 3 wt.% LZO-coated sample annealed at 650 °C. This may indicate that less LZO coating content was found on the surface of NMC811 at a higher annealing temperature due to the diffusion of Zr into the center bulk. This observation is consistent with the study of Song et al [107]. Song et al. found Zr diffused from the surface into the bulk of TARGRAY NMC811 as a result of annealing temperature at 800 °C. However, the author also found Zr in the form of LZO on the surface of coated NMC, although penetration into the bulk occurs.

Most of the studies have revealed that the doping effects may not show the improvements in cyclability of the cell [141, 107]. Furthermore, the S(T)EM images at low magnification show that secondary particles in both samples fractured into thousands of nano-sized primary particles, as shown in Figure 3.24(a) and Figure 3.24(b). These damages may have been caused by a physical contact when NMC811 powder was collected after calcination from an Al crucible by an Al stick. This observation may be closely related to the study of Zheng et al., who investigated the effect of calcination temperature on the primary particle size of Ni-rich cathode material calcined at temperatures ranging from 725 to 900 °C. According to the author, the materials calcined at various temperatures exhibit varying degrees of crack formation, which becomes more significant and severe as the calcining temperature increases. Zheng et al. believed the increasing size of the primary particles as the calcination temperature rises is a crucial factor in the creation of cracks. Materials calcined at relatively low temperatures (725 - 775 °C) consist of well-aligned nanoplate particles that cause less micro-strain during each Li^+ ion extraction. In contrast, materials prepared at higher temperatures (800 – 900 °C), display severe micro-cracks and voids inside the particles due to anisotropic volume variation-induced micro-strain. Li+ ion extraction during cyclying has not yet been performed on the 1LiAcZO@NMC811_Cal800 and 1LiAcZO@NMC811_Cal800. However, the secondary particle could be easily fractured when physical force from the Al stick and crack formation could also easily occur in these samples during cycling. It should be noted that the as-received NMC811 powder may have undergone an annealing treatment during synthesis. These results may suggest that the use of high temperatures ($\geq$ 800 °C) in the coating process may be harmful to the particles and unsuitable for the fabrication of cathode composites, which require the grinding of CAM, SE, and C and further pelleting of ASSBs, as described in Section 2.5

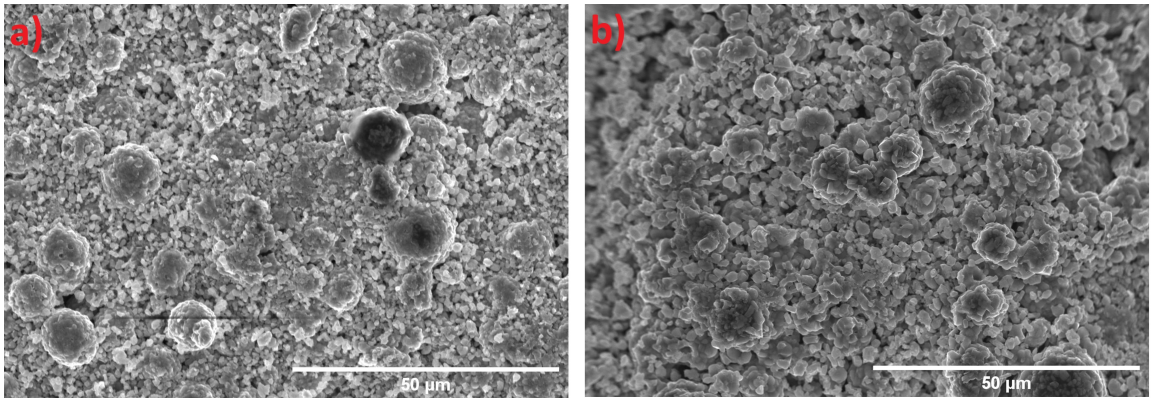

Figure 3.24: Low-magnification S(T)EM images of a) 2 wt.% and b) 3 wt.% LZO-coated NMC811 samples using Method 3.

3.2.5 Solvent Evaporation Effects on LZO-coated NMC811

The factor in the sol-gel coating process that may affect the uniformity of the coating layer should be addressed by comparing the LZO-coated NMC811's results in Section 3.2.3 from Method 1 with the results from Method 3, as shown in this part. The primary distinction between the coated samples of these two methods was established using S(T)EM analysis and EDX mappings. It should be emphasized that the sample with the excessive LZO coating content in each method were selected for the method comparison in order to clearly seen the variations in how LZO layer forms on TARGRAY NMC811 which are 3LiAcZO@NMC811_Cal650 for Method

1 and 3LiNiZO@NMC811_Cal650 for Method 3. The low-magnification S(T)EM image (Figure 3.25a) shows that the coated 3 wt.% LZO-coated TARGRAY NMC811 powder produced by Method 1 yields secondary particles that are remarkably monodispersed. Comparing the 3LiAcZO@NMC811_Cal650 to a low-magnification image of uncoated TARGRAY NMC811 (Figure 3.2), no differences were detected. In contrast, the 3 wt.% LZO-coated TARGRAY NMC811 powder using Method 3 was discovered to have agglomerated into enormous masses which consist numerous of NMC811 secondary particles, as shown in Figure 3.25b.

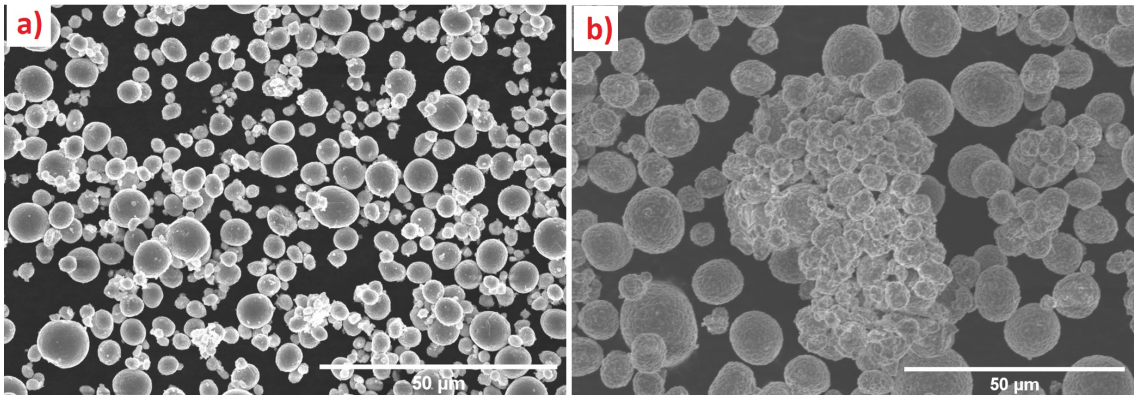

Figure 3.25: Low-magnification S(T)EM images of 3wt.% LZO-coated samples produced by the process in a) Method 1 and b) Method 2.

The high-magnification S(T)EM images of the 3LiNiZO@NMC811_Cal650 sample as the coating results of the solvent evaporation process in Method 3, as shown in Figure 3.24

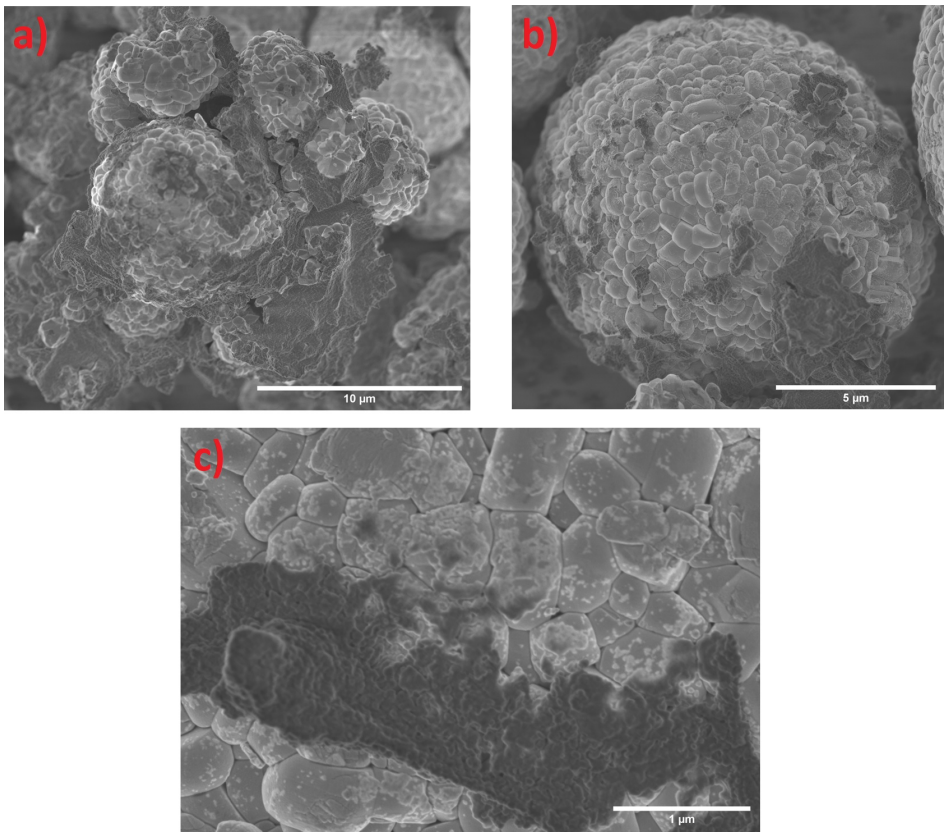

Figure 3.26: S(T)EM images at high magnification of a) the agglomeration, b) a secondary particle, and c) primary particles of 3 wt.%LZO-coated NMC811 using Method 3.

The factor that agglomerates secondary particles of NMC811 was investigated using a smaller agglomerated mass of particles in the high-magnification S(T)EM image in SE mode, as shown in Figure 3.26a. Secondary particles are agglomerated by an unidentified substance, as seen in the image. This amount could be the synthesized LZO based on the surface of successful coated samples (Figure 3.15 and Figure 3.16). Figure 3.26b displays a secondary particle of 3LiNiZO@NMC811_Cal650, it is evident that just a small part on the TARGRAY NMC811 surface was coated, leaving the majority of the smooth surface exposed. The magnified images (Figure 3.26c) reveal that the majority of the primary particles have a clear surface and aculeated edges. To further elucidate the unidentified substance that adsorbs on the surface and agglomerates TARGRAY NMC811 particles, EDX mapping was performed on some agglomerations, as shown in Figure 3.27. The contrast and resolution of the unidentified substance are reduced in all high-magnification S(T)EM images compared to Figure 3.26. This is explained by raising the acceleration voltage from 1 kV to 20 kV for EDX mapping, as discussed in Section 2.6.2 and Section 2.6.4. The Zr elemental mappings show that most of the dot densities come from the unidentified material and not from the surface of TARGRAY NMC811. this suggests that the LZO coating layers used in Method 3 have agglomerated TARGRAY NMC811 particles as well as been coated non-uniformly.

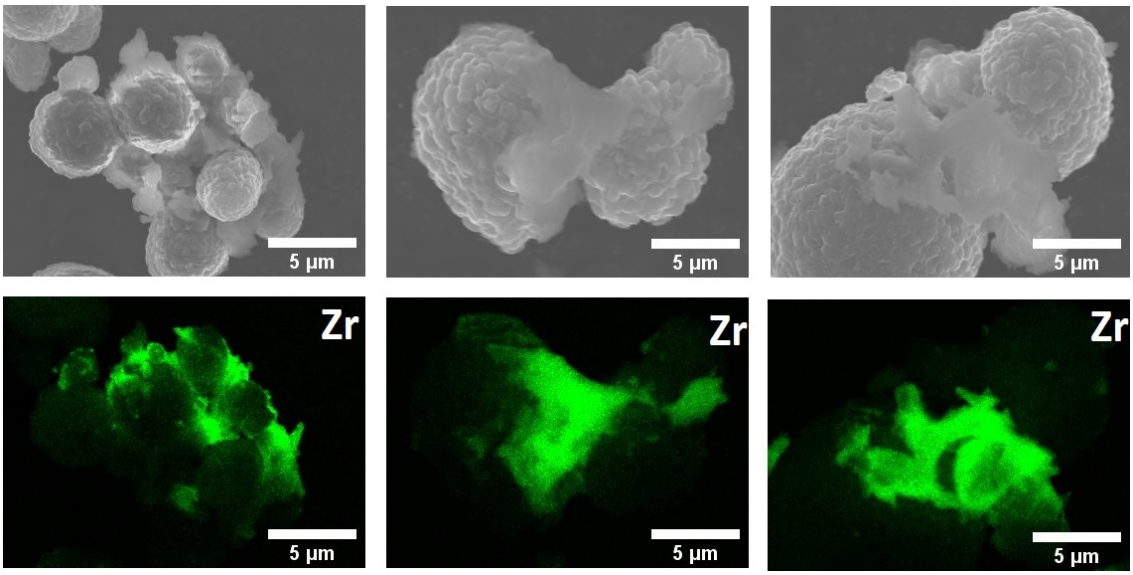

Figure 3.27: Zr elemental EDX mappings of 3LiNi@NMC811 particle agglomerations

As evident in Section 3.2.3, coating method 1 has produced homogeneous LZO coating layers on TARGRAY NMC811. It's important to note that the two methods use distinct lithium precursors. However, Method 1 can produce a uniform coating layer not only by using $CH_3COOLi.2H_2O$ as a lithium precursor, but also by using the same lithium precursor as Method 3 ($LiNO_3$), this has been discussed in Section 3.2.3 and the results are shown in Figure 3.18. A direct comparison would be possible by coating TARGRAY NMC811 with LZO using Method 3 with $CH_3COOLi.2H_2O$ as the precursor. The low-magnification S(T)EM image of 3LiAcZO@NMC811_method3 samples is shown in Figure 3.28a, with secondary particles still agglomerated into massive masses. Figure 3.26b shows a high-magnification S(T)EM image of a 3LiAcZO@NMC811_method3 with clearly visible non-uniform coating content as evidenced by Zr elemental mapping Figure 3.26c.

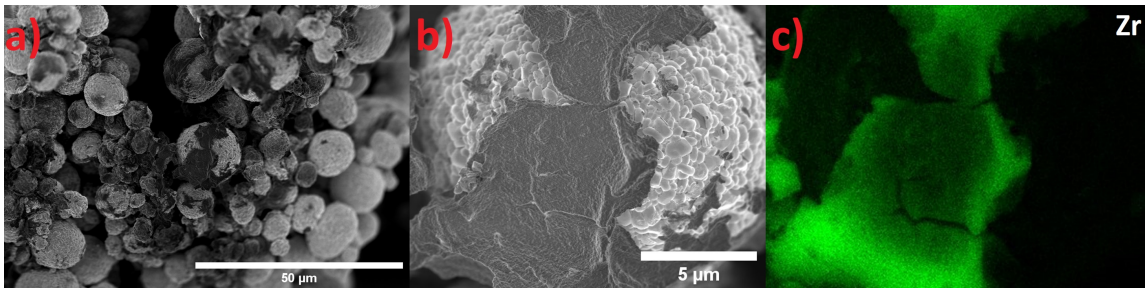

Figure 3.28: a) Low-magnification S(T)EM image of 3LiAcZO@NMC811_method3, b) High-magnification S(T)EM image of 3LiAcZO@NMC811_method3 and c) it's Zr elemental EDX mapping.

It is now apparent that the homogeneity of the LZO coating layer may not change while using the two kinds of lithium precursors mentioned in the same coating process. Therefore, it is important to look at the other difference in the process between Method 1 and Method 3. As discussed in Section 3.2.1, the evaporation of the solvent in the two methods is different. Method 1 included the drying of samples at 80 °C under vigorous stirring, while samples produced by Method 3 were dried in a close space without stirring, which may have reduced the interaction of hydrogen-bonding results in hydrolyzed ZrO_2 coating species that do not or weakly adsorp on the surface of TARGRAY NMC811 particles. According to Bokov et al. [139], the non-adsorbent ZrO_2 coating species may transform into large pieces of aerogel and condensate to a large mass of agglomeration after solvent evaporation in a close system under controlled temperature and pressure. Furthermore, the post-grinding step in Method 1 after the samples have completely dried could make the coated TarGray NMC811 powder remain monodisperse.

3.3 Solid state battery testing

3.3.1 Lithiation of In foil

Figure 3.29a depicts the morphology of a representative In foil before lithiation in coin-type cells with a Li counter electrode. The steps fabrication of Li-In alloys were described in Section 2.4. As shown in Figure 3.29b, homogeneous lithiation was obtained on the front side.

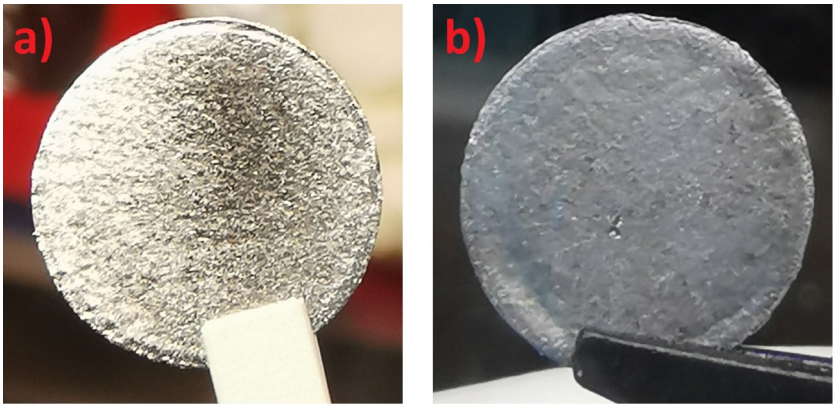

Figure 3.29: Morphology of a representative Indium foil a) before b) after lithiation with 0.1 $mA.cm^{-2}$. The lithiation was conducted at a current density of 0.1 $mA.cm^{-2}$ with a Li metal counter electrode.

Figure 3.30s depicts the voltage profile of the coin cell employed for coulometric titration of indium by lithium to produce Li-In alloy. In ASSBs, the Li-In alloys served as the anode electrode. When

lithium ions diffuse into the indium foil, the voltage drop is seen. The voltage drop to 0.517 V until reach to the stable cell voltage of 0.565 V.

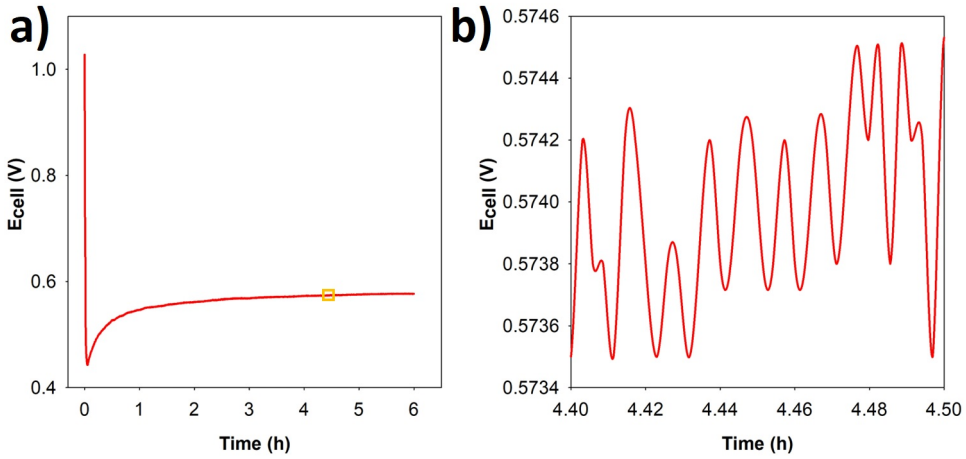

Figure 3.30: a) The voltage profile of the discharging cell used for lithiation. b) The magnified area of the voltage drop.

The magnified graph displays the marked area of the voltage under stable condition. The relaxation caused by the pulse lithiation procedure, as shown in Figure 3.30b.

3.3.2 Galvanostatic Cycling with Potential Limitation Testing

An electrochemical performance study on uncoated TARGRAY NMC811, coated with 0.5 wt.%, 1 wt.%, 2 wt.% and 3 wt.% LZO content using Method 1 was conducted in the voltage range of 2.38 V to 3.68 V utilizing pelletized ASSB half-cells, with argyrodite LPSCl and Li-In alloy as a solid electrolyte and an anode. The voltage range was considered based on the voltage drop of a Li-ion anode [148]. The assembly of ASSB half-cells has been described in Section 2.5. Two sets of experiments were performed at room temperature with varying C rates. The cycling performance was the first study of the cathode ASSB half-cells stability and capacity retention over time. In addition, the CAM initial discharge capacity was determined during this test. The rate performance was the second test performed to assess the power performance under various current loads of ASSB half-cells.

Cycling Performance Evaluation

All of the uncoated and coated samples listed above were cycled at a charge and discharge rate of 0.1 C for 2 cycles, and then the C-rate was raised to 0.2 C for 67 cycles. A total of 69 cycles were done in this test. The initial charge-discharge profiles of the pristine and coated samples at 0.1 C are shown in Figure 3.31.

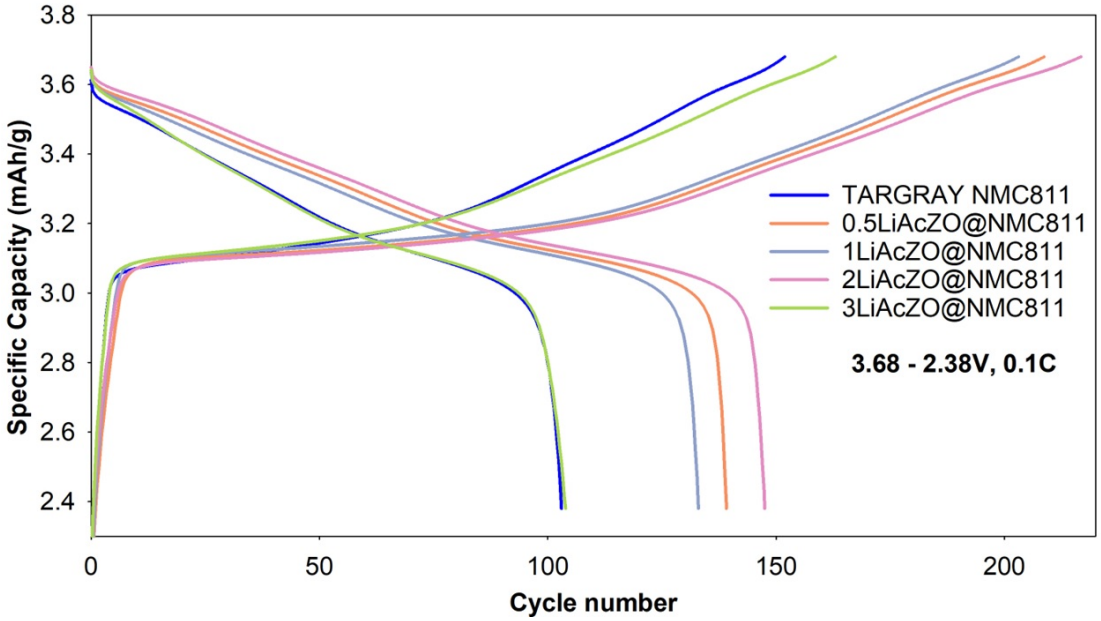

Figure 3.31: The initial charge/discharge profiles at 0.1C in the voltage range of 2.38 - 3.68 V of the uncoated TARGRAY NMC811, 0.5%, 1%, 2% and 3% LZO-coated NMC811 using Method 1.

At 3.1 V, all charge-discharge profiles display the monotonous potential plateaus of layered NMC811, which are ascribed to the Ni^{2+}/Ni^{4+} redox couple [140]. The discharge specific capacities of CAMs are 103, 139.1, 133, 147.5, and 103.9 mAh/g, respectively, as the LZO coating concentration increases from 0% to 3 wt.%. Compared to uncoated TARGRAY NMC811, the 0.5 wt.%, 1 wt.%, and 2 wt% LZO-coated NMC811 cathodes showed a significant increase in initial specific capacities in both charge and discharge. This may indicate that the interfacial resistance from the formation of a decomposition layer at the SE/CAM interfaces or the contact loss of the CAM was relieved by coating with LZO. However, both the charge and discharge specific capacities of the 3 wt.% LZO coating were dramatically decreased in comparison to the 2 wt.% LZO coating and similar to uncoated TARGRAY NMC811. Kim et al. [145] discovered a similar trend while increasing the coating content of LZO, which led to an increase in specific capacities before there was a significant drop in the excessive coating amount samples. The author stated why an extensive coating of LZO might lower discharge capacity. When LZO particles completely cover the cathode surface, the distance between the SE and CAM interfaces increases inefficiently, and performance declines. In addition, the mass ratio of CAM in the cathode composite would be affected by the significantly increased mass ratio of LZO and the initial capacity of the excessive LZO coating layers would decrease eventually [108].

All the cells are charged and discharged at 0.1 C for two cycles, followed by 67 cycles at 0.2 C in the same voltage range. The cycling performance of all samples at this C-rate is shown in Figure 3.32.

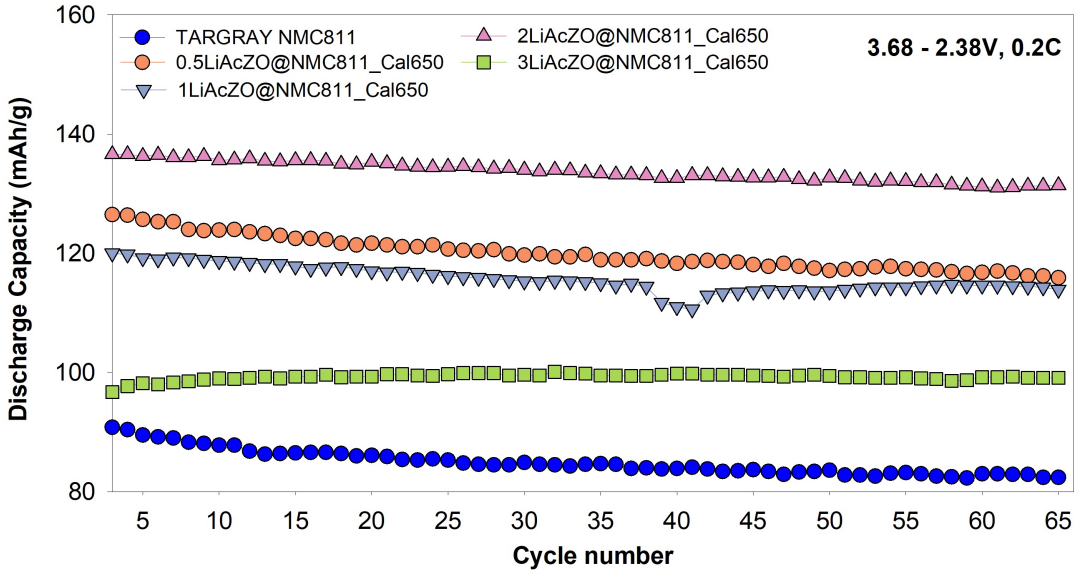

Figure 3.32: Cycle performances at 0.1C in the voltage range of 2.38 - 3.68 V of the uncoated TARGRAY NMC811, 0.5%, 1%, 2% and 3% LZO-coated NMC811 using Method 1.

According to the graph, these curves for uncoated and coated NMC811 exhibited almost identical trends, with only variations in capacity values. The uncoated NMC811 ASSB half-cells had an initial capacity of 90.8 mAh/g and a capacity retention of 90.75%. The 0.5 wt.% LZO-coated NMC811 cell had a significant rise in initial capacity with 126.5 mAh/g, although capacity retention was comparable at 90.9%. In comparison, the 1 wt.% LZO-coated NMC811 cell had a lower initial capacity of 120 mAh/g but a higher capacity retention of 94.4%. The cell composed of 2 wt.% LZO has the greatest initial capacity of 136.6 mAh/g, and its capacity retention is 92.6%. Finally, the ASSB half-cell containing 3 wt.% LZO was witnessed to have the highest capacity retention, almost 99.9%, whereas the initial capacity is 96.7 mAh/g. Evidently, the capacity retentions of all the cells made of the LZO-coated sample are greater than those of the uncoated TARGRAY NMC811, perhaps as a result of the protective coating layer formed around the CAM secondary particles. It should be noticed that after 67 cycles, the NMC811 cell made of the excessive LZO coating amount sample demonstrates remarkable stability with almost no capacity loss.

The capacity retention ratio (CRR) is defined by Hassan et al. [149] as the ratio of the capacity retention of coated CAM to the capacity retention of uncoated CAM. Figure 3.33 depicts the CRR of LZO-coated NMC811 using Method 1. The CRR of uncoated NMC811 is represented by the LZO weight percent of zero, which is equal to one.

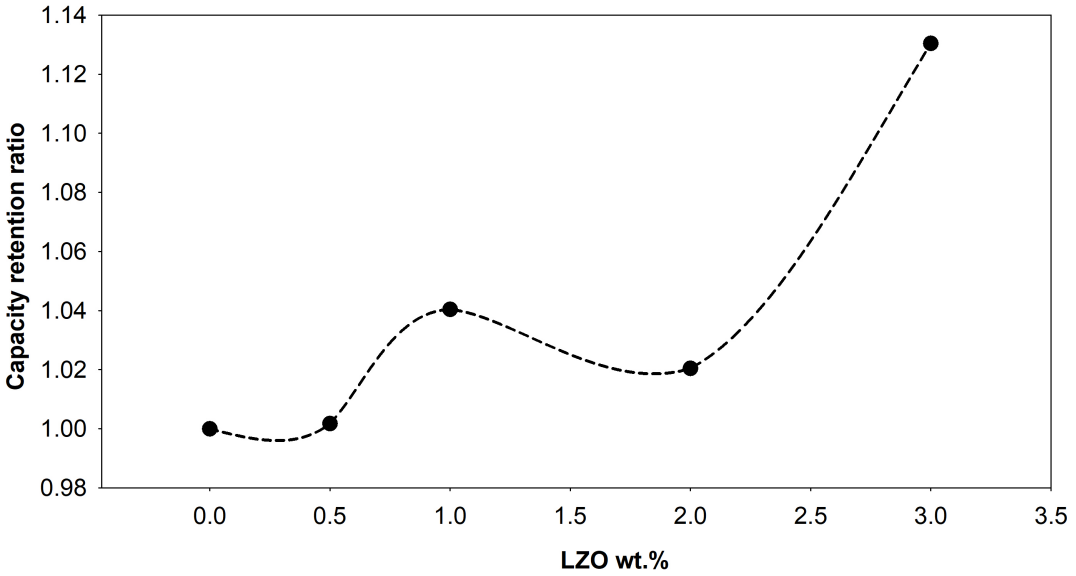

Figure 3.33: Capacity retention ratio of the all LZO-coated NMC811 using Method 1 for 69 cycles at 0.1C in the voltage range of 2.38 - 3.68 V.

The CRR of uncoated NMC811 is represented by the LZO content of 0%, which is equal to one. After 67 cycles, it is obvious that the sample coated with 3 wt.% LZO showed the highest ratio, which is 1.13. 1 wt.% LZO-coated samples had the second-highest CRR ratio, which is 1.04. The CRR of the sample coated with 2 wt.% LZO is lower, at 1.02. The CRR of a 0.5 wt.% LZO-coated sample is close to 1. The findings could indicate that LZO coating layer has not only enhanced specific discharge capacity of CAM, but also increased the stability during cycling. Most likely, the change in surface chemistry that led to this improvement was caused by the fact that the uniform LZO-coating layer could block the contact between the CAM and SE. This could prevent side reactions and lowered the surface resistance [108]. LZO-coating layer may also improve the transport of Li^+ of in cathode composite; hence, modifying CAM with an adequate quantity of LZO may effectively avoid capacity fading [108, 140]. A coating layer that is too thick may hinder the intercalation and deintercalation of Li^+.

Rate Performance Evaluation

For the evaluation of rate performance, uncoated TARGRAY NMC811, 1 wt.%, 2 wt.%, and 3 wt.% LZO-coated NMC811 samples were utilized in cathode composites to assemble new ASSB half-cells. In the new sets of testing, the same cut-off voltage of 2.38 V to 3.68 V was applied at various C-rates of 0.1C, 0.2C, 0.5C, 1C, and 2C, before returning to 0.1 C at ambient temperature. Regarding initial capacity, new ASSB half-cells were tested under identical conditions as the cycling performance evaluation. Consequently, the Coulombic efficiency values are provided in the accompanying Figure 3.34, which are the average measurements of two cells, one of which was assembled for rate performance and the other for cycling performance. In the initial cycle, uncoated TARGRAY NMC811 attained a Coulombic efficiency of 68.70 ± 1.17 wt.%. The Coulombic efficiency of cells utilizing 1 wt.%, 2 wt.%, and 3 wt.% LZO-coated NMC811 was 65.84 ± 0.54%, 67.65 ± 0.58%, and 64.84 ± 1.18%, respectively. In the second cycle, cells using uncoated and coated NMC811 exhibited similarly increase in Coulombic efficiency. Which are 98.05 ± 0.51% for the uncoated NMC811, 98.34 ± 0.04%, 98.29 ± 0.33% and 97.52 ± 0.48% for the 1 wt.%, 2 wt.%, and 3 wt.% LZO-coated NMC811, respectively. These results of ASSB half-cell test are similar in several studies of the full cell configuration of NMC cathode-based LIBs [107], from the creation of the solid electrolyte interphasic (SEI) layer on both electrodes to the rise of Coulombic efficiency from the first cycle to the second cycle.

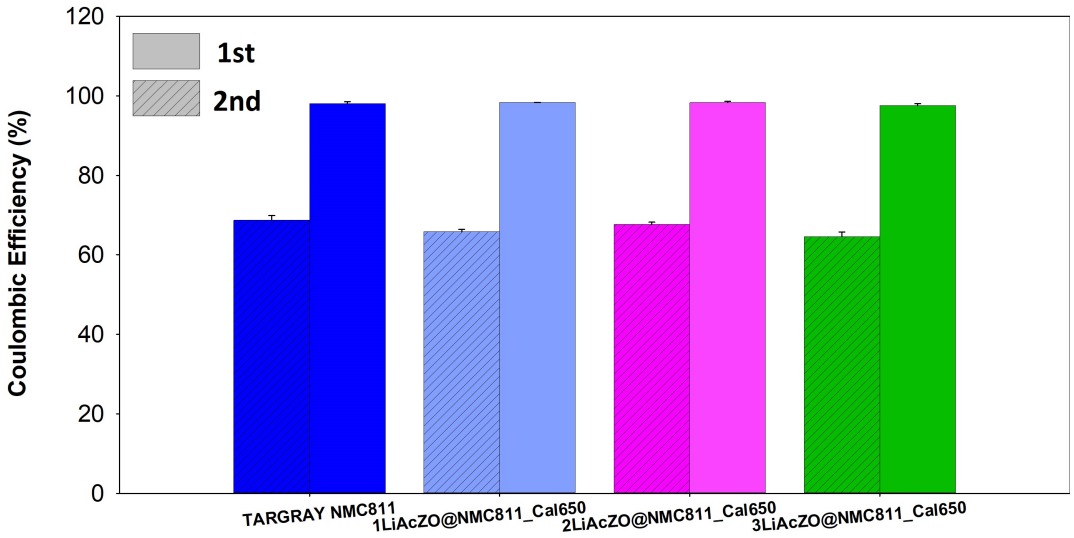

Figure 3.34: Coulombic efficiencies for the initial and second cycles at 0.1C in the voltage range of 2.38 - 3.68 V of the uncoated TARGRAY NMC811, 1%, 2% and 3% LZO coating NMC811 using Method 1.

Despite the increase in cycling performance due to surface coating, the first cycle Coulombic efficiencies of all samples were remained below 80%, which is consider as the low value for a cathode composite [148]. This suggests that the sulfide electrolyte is actively decomposing despite the surface modification during the first cycle, which might be attributable to different side reactions between the CAM and SE.

The results of the rate performance test comparing uncoated TARGRAY NMC811 to 1 wt.%, 2 wt.%, and 3 wt.% LZO-coated NMC811 are shown in Figure 3.35. Regarding the initial discharge capacity at 0.1C and comparing it to the initial discharge capacity of the cycling performance test, there is a difference in that the initial discharge capacity of uncoated TARGRAY NMC811 is higher than the value of 3 wt.% LZO-coated NMC811, which is 122.9 and 104.7 mAh/g, respectively. However, a similar trend is seen in 1 wt.% LZO-coated NMC811, which has the second greatest discharge capacity, and 2 wt.% LZO-coated NMC811, which has the highest discharge capacity; their corresponding discharge capacities are 124.7 and 149 mAh/g. These trend of specific discharge capacities is remain in the range of C-rate from 0.1C to 0.5C. It was clear that the discharge capacities of all the samples had significant drop as C-rate went up. The specific discharge capacities of uncoated TARGRAY NMC811 and 1 wt.% LZO-coated NMC approach the value of 3 wt.% LZO-coated NMC at 1C. Both of these values for uncoated and 1 wt.% coated NMC811 are less than 3 wt.% at 2C until the first order is reestablished when the C-rate returns to 0.1C. As shown in the data, coating TARGRAY NMC811 with 2 wt.% LZO results in the largest increase in terms of rate capability. At high C rates, these samples have higher capacities than the uncoated TarGray NMC811 and are maintained upon returning to 0.1 C. These result is consitent to the results of cycling performance which may imply the 2 wt.% LZO is the suitable of coating content for the increase in the electrochemical performance of NMC811.

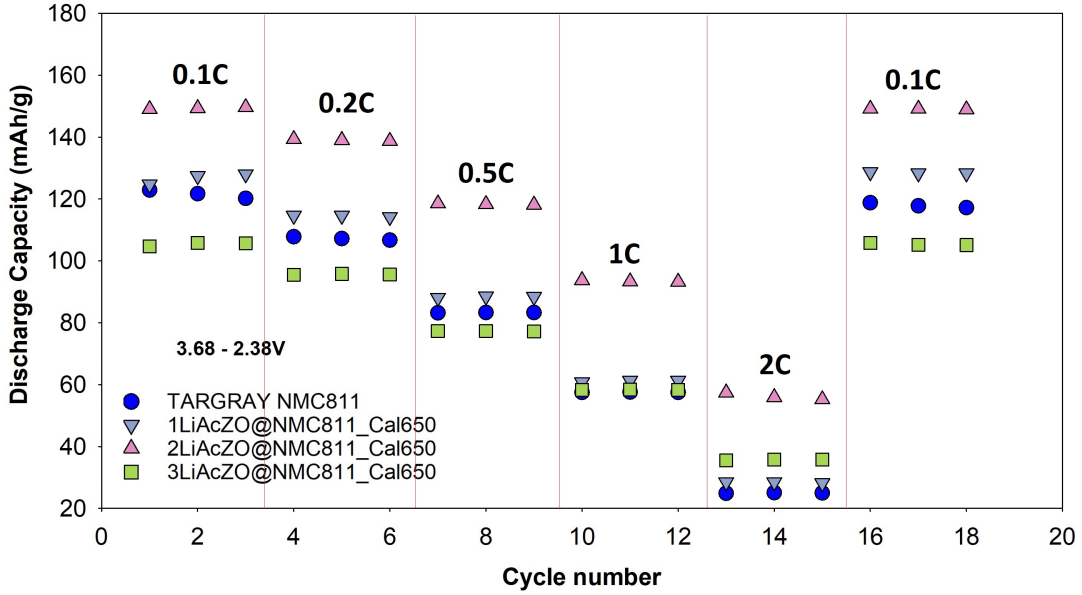

Figure 3.35: Rate performance in the voltage range of 2.38 - 3.68 V of the uncoated TARGRAY NMC811, 1%, 2% and 3% LZO-coated NMC811 using Method 1.

Chapter 4

Conclusion

In this thesis, an effective wet chemical water-free coating process was established to modify the surface of NMC811 with LZO, which improved the electrochemical performance of pelletized ASSBs using Ni-rich NCM based cathodes. In addition, this process did not require the preparation of water-sensitive NMC materials with citric acid in the moisture solvent, as is necessary in other commonly used sol-gel coating processes in order to obtain a homogeneous coating layer.

In addition, the conditions of calcination temperature, solvent evaporation, precursor kinds, and LZO coating concentration have been studied to understand the growth mechanism of the LZO coating layer on NMC811. Three wet coating (sol-gel) methods were designed as a result of variations in the aforementioned conditions. It has been found that both Method 1 and Method 2 can make a uniform coating through the solvent evaporation process of ethanol at 80 °C, which includes vigorous stirring in room condition. The evaporation conditions of Method 3 resulted in the formation of an inhomogeneous LZO coating layer capable of agglomerating NMC811 secondary particles. This was done in a closed system where the temperature and pressure were controlled and the solvent was not stirred as it evaporated.

In addition, the high temperature in the calcination process of Method 2 may have doped Zr into the NMC811 bulk material. It was also established that the material was unsuitable for the assembly of ASSBs because physical force exerted during handling, grinding, and pelleting might damage the NMC811 material and induce the fracture of secondary particles.

Method 1 is found to be beneficial for coating ready-to-use cathodes, due to the low temperature and the uniform coating layer that it could produce. Using this method, different weight percentages of LZO grew uniformly on the surface of commercial NMC811, and 3 wt.% LZO was determined to be excessive for producing a thick LZO coating layer.

ASSB half-cells were assembled, and GCPL was done to test the electrical performance of uncoated and coated NMC811. The thickness of the coating layer has been determined to be the influential physical parameter on the cycling performance of ASSB. ASSB half-cells assembled with 2 wt.% LZO coated sample can deliver the initial discharge capacity of from 147.5 - 149 mAh/g in comparasion with uncoated NMC811 (103 - 122.9 mAh/g). While the excessive coating level of 3 wt.% LZO ABBS half-cells decreased the initial discharge capacity to around 103.9 – 104.7 mAh/g, the capacity retention after 69 cycles remained at 99.9%, which was greater than 90.6% and 92.0% for uncoated NMC811 and 2 wt.% LZO-coated NMC811. With an adequate coating content, the LZO coating layer has not only increased the specific discharge capacity of CAM, but it has also increased the stability of ASSBs during cycling.

Further works

Low levels of interdiffusion between the CAM and coating might be advantageous to the performance of the cathode electrode. Therefore, more research is needed to determine the optimal temperature treatment during calcination could cause a little of Zr diffuse into bulk and how this affects the electrochemical performance of ASSBs. Additionally, a method of assembly for ASSB half-cells that could minimize the fracture of secondary particles should be developed. In addition, because it is known that uncoated NCM materials create oxygen during cycle [57], even in an ASSB environment, an intriguing further question would be if coatings may chemically stabilize NCM CAM at high potentials to further reduce gas emission.

Bibliography

[1] Arava Leela Mohana Reddy et al. 'Hybrid nanostructures for energy storage applications'. In: *Advanced Materials* 24.37 (2012), pp. 5045–5064.

[2] Zhenguo Yang et al. 'Electrochemical energy storage for green grid'. In: *Chemical reviews* 111.5 (2011), pp. 3577–3613.

[3] Antonino Salvatore Arico et al. 'Nanostructured materials for advanced energy conversion and storage devices'. In: *Materials for sustainable energy: a collection of peer-reviewed research and review articles from Nature Publishing Group* (2011), pp. 148–159.

[4] Yoshio Nishi. 'The development of lithium ion secondary batteries'. In: *The Chemical Record* 1.5 (2001), pp. 406–413.

[5] Tyler Or et al. 'Recycling of mixed cathode lithium-ion batteries for electric vehicles: Current status and future outlook'. In: *Carbon Energy* 2.1 (2020), pp. 6–43.

[6] Matthew Li et al. '30 years of lithium-ion batteries'. In: *Advanced Materials* 30.33 (2018), p. 1800561.

[7] Yang Zhao, Keegan R Adair and Xueliang Sun. 'Recent developments and insights into the understanding of Na metal anodes for Na-metal batteries'. In: *Energy & Environmental Science* 11.10 (2018), pp. 2673–2695.

[8] Jiajie Zhu, Husam N Alshareef and Udo Schwingenschlögl. 'Functionalized NbS2 as cathode for Li-and Na-ion batteries'. In: *Applied Physics Letters* 111.4 (2017), p. 043903.

[9] Li-Xia Yuan et al. 'Development and challenges of LiFePO 4 cathode material for lithium-ion batteries'. In: *Energy & Environmental Science* 4.2 (2011), pp. 269–284.

[10] Ryan A Adams, Arvind Varma and Vilas G Pol. 'Carbon anodes for nonaqueous alkali metal-ion batteries and their thermal safety aspects'. In: *Advanced Energy Materials* 9.35 (2019), p. 1900550.

[11] Shung-Ik Lee et al. 'A study of electrochemical kinetics of lithium ion in organic electrolytes'. In: *Korean Journal of Chemical Engineering* 19.4 (2002), pp. 638–644.

[12] Sarah G Stewart and John Newman. 'The use of UV/vis absorption to measure diffusion coefficients in LiPF6 electrolytic solutions'. In: *Journal of the Electrochemical Society* 155.1 (2007), F13.

[13] Peiyuan Guan et al. 'Recent progress of surface coating on cathode materials for high-performance lithium-ion batteries'. In: *Journal of Energy Chemistry* 43 (2020), pp. 220–235.

[14] Holger C Hesse et al. 'Lithium-ion battery storage for the grid—A review of stationary battery storage system design tailored for applications in modern power grids'. In: *Energies* 10.12 (2017), p. 2107.

[15] Shishuo Liang et al. 'Gel polymer electrolytes for lithium ion batteries: Fabrication, characterization and performance'. In: *Solid State Ionics* 318 (2018), pp. 2–18.

[16] Arumugam Manthiram. 'A reflection on lithium-ion battery cathode chemistry'. In: *Nature communications* 11.1 (2020), pp. 1–9.

[17] Ji Ung Choi et al. 'Recent progress and perspective of advanced high-energy Co-less Ni-rich cathodes for Li-ion batteries: yesterday, today, and tomorrow'. In: *Advanced Energy Materials* 10.42 (2020), p. 2002027.

[18] Wu Xu et al. 'Lithium metal anodes for rechargeable batteries'. In: *Energy & Environmental Science* 7.2 (2014), pp. 513–537.

[19] Quan Pang et al. 'An in vivo formed solid electrolyte surface layer enables stable plating of Li metal'. In: *Joule* 1.4 (2017), pp. 871–886.

[20] Tetsuo Nishida et al. 'Optical observation of Li dendrite growth in ionic liquid'. In: *Electrochimica acta* 100 (2013), pp. 333–341.

[21] Jürgen Janek and Wolfgang G Zeier. 'A solid future for battery development'. In: *Nature Energy* 1.9 (2016), pp. 1–4.

[22] Masahiro Tatsumisago, Motohiro Nagao and Akitoshi Hayashi. 'Recent development of sulfide solid electrolytes and interfacial modification for all-solid-state rechargeable lithium batteries'. In: *Journal of Asian Ceramic Societies* 1.1 (2013), pp. 17–25.

[23] Fudong Han et al. 'Suppressing Li dendrite formation in Li2S-P2S5 solid electrolyte by LiI incorporation'. In: *Advanced Energy Materials* 8.18 (2018), p. 1703644.

[24] Heinz Gerischer, Franco Decker and Bruno Scrosati. 'The electronic and the ionic contribution to the free energy of alkali metals in intercalation compounds'. In: *Journal of the Electrochemical Society* 141.9 (1994), p. 2297.

[25] Dino Tonti, Christian Pettenkofer and Wolfram Jaegermann. 'Origin of the electrochemical potential in intercalation electrodes: experimental estimation of the electronic and ionic contributions for Na intercalated into TiS2'. In: *The Journal of Physical Chemistry B* 108.41 (2004), pp. 16093–16099.

[26] René Hausbrand, Dirk Becker and Wolfram Jaegermann. 'A surface science approach to cathode/electrolyte interfaces in Li-ion batteries: Contact properties, charge transfer and reactions'. In: *Progress in Solid State Chemistry* 42.4 (2014), pp. 175–183.

[27] Janae Csavina et al. 'Effect of wind speed and relative humidity on atmospheric dust concentrations in semi-arid climates'. In: *Science of the Total Environment* 487 (2014), pp. 82–90.

[28] Gennady Cherkashinin, René Hausbrand and Wolfram Jaegermann. 'Performance of Li-ion batteries: contribution of electronic factors to the battery voltage'. In: *Journal of the Electrochemical Society* 166.3 (2019), A5308.

[29] Arup Chakraborty et al. 'Layered Cathode Materials for Lithium-Ion Batteries: Review of Computational Studies on LiNi1–x–y Co x Mn y O2 and LiNi1–x–y Co x Al y O2'. In: *Chemistry of Materials* 32.3 (2020), pp. 915–952.

[30] João Pedro Silva et al. 'Practical microwave-assisted solid-state synthesis of the spinel LiMn2O4'. In: *Solid State Ionics* 268 (2014), pp. 42–47.

[31] Raimund Koerver et al. 'Chemo-mechanical expansion of lithium electrode materials–on the route to mechanically optimized all-solid-state batteries'. In: *Energy & Environmental Science* 11.8 (2018), pp. 2142–2158.

[32] Arumugam Manthiram, Xingwen Yu and Shaofei Wang. 'Lithium battery chemistries enabled by solid-state electrolytes'. In: *Nature Reviews Materials* 2.4 (2017), pp. 1–16.

[33] Simon Randau et al. 'Benchmarking the performance of all-solid-state lithium batteries'. In: *Nature Energy* 5.3 (2020), pp. 259–270.

[34] Wenbo Zhang et al. 'Interfacial processes and influence of composite cathode microstructure controlling the performance of all-solid-state lithium batteries'. In: *ACS applied materials & interfaces* 9.21 (2017), pp. 17835–17845.

[35] Atsushi Sakuda, Akitoshi Hayashi and Masahiro Tatsumisago. 'Sulfide solid electrolyte with favorable mechanical property for all-solid-state lithium battery'. In: *Scientific reports* 3.1 (2013), pp. 1–5.

[36] Atsutaka Kato et al. 'Mechanical properties of Li2S–P2S5 glasses with lithium halides and application in all-solid-state batteries'. In: *ACS Applied Energy Materials* 1.3 (2018), pp. 1002–1007.

[37] Kang Xu. 'Electrolytes and interphases in Li-ion batteries and beyond'. In: *Chemical reviews* 114.23 (2014), pp. 11503–11618.

[38] John Christopher Bachman et al. 'Inorganic solid-state electrolytes for lithium batteries: mechanisms and properties governing ion conduction'. In: *Chemical reviews* 116.1 (2016), pp. 140–162.

[39] Zhizhen Zhang et al. 'New horizons for inorganic solid state ion conductors'. In: *Energy & Environmental Science* 11.8 (2018), pp. 1945–1976.

[40] Rusong Chen et al. 'Approaching practically accessible solid-state batteries: stability issues related to solid electrolytes and interfaces'. In: *Chemical reviews* 120.14 (2019), pp. 6820–6877.

[41] Laidong Zhou et al. 'Innovative approaches to Li-argyrodite solid electrolytes for all-solid-state lithium batteries'. In: *Accounts of Chemical Research* 54.12 (2021), pp. 2717–2728.

[42] Marvin A Kraft et al. 'Influence of lattice polarizability on the ionic conductivity in the lithium superionic argyrodites Li6PS5X (X= Cl, Br, I)'. In: *Journal of the American Chemical Society* 139.31 (2017), pp. 10909–10918.

[43] Marvin A Kraft et al. 'Inducing high ionic conductivity in the lithium superionic argyrodites Li6+ x P1–x Ge x S5I for all-solid-state batteries'. In: *Journal of the American Chemical Society* 140.47 (2018), pp. 16330–16339.

[44] Hans-Jörg Deiseroth et al. 'Li6PS5X: a class of crystalline Li-rich solids with an unusually high Li+ mobility'. In: *Angewandte Chemie International Edition* 47.4 (2008), pp. 755–758.

[45] Parvin Adeli et al. 'Boosting solid-state diffusivity and conductivity in lithium superionic argyrodites by halide substitution'. In: *Angewandte Chemie* 131.26 (2019), pp. 8773–8778.

[46] Shiao-Tong Kong et al. 'Lithium argyrodites with phosphorus and arsenic: order and disorder of lithium atoms, crystal chemistry, and phase transitions'. In: *Chemistry–A European Journal* 16.7 (2010), pp. 2198–2206.

[47] Saneyuki Ohno et al. 'Further evidence for energy landscape flattening in the superionic argyrodites Li6+ x P1–x M x S5I (M= Si, Ge, Sn)'. In: *Chemistry of Materials* 31.13 (2019), pp. 4936–4944.

[48] Holger Schneider et al. 'A novel class of halogen-free, super-conductive lithium argyrodites: Synthesis and characterization'. In: *Journal of Power Sources* 366 (2017), pp. 151–160.

[49] Pengbo Wang et al. 'Fast Ion Conduction and Its Origin in Li6–x PS5–x Br1+ x'. In: *Chemistry of Materials* 32.9 (2020), pp. 3833–3840.

[50] Wenze Huang et al. 'Superionic lithium conductor with a cubic argyrodite-type structure in the Li–Al–Si–S system'. In: *Journal of Solid State Chemistry* 270 (2019), pp. 487–492.

[51] Yuki Inoue et al. 'Synthesis and structure of novel lithium-ion conductor Li7Ge3PS12'. In: *Journal of Solid State Chemistry* 246 (2017), pp. 334–340.

[52] Shiao-Tong Kong et al. 'Li6PO5Br and Li6PO5Cl: The first Lithium-Oxide-Argyrodites'. In: *Zeitschrift für anorganische und allgemeine Chemie* 636.11 (2010), pp. 1920–1924.

[53] Laidong Zhou et al. 'New family of argyrodite thioantimonate lithium superionic conductors'. In: *Journal of the American Chemical Society* 141.48 (2019), pp. 19002–19013.

[54] Laidong Zhou et al. 'Solvent-engineered design of argyrodite Li6PS5X (X= Cl, Br, I) solid electrolytes with high ionic conductivity'. In: *ACS Energy Letters* 4.1 (2018), pp. 265–270.

[55] Shiao-Tong Kong et al. 'Lithium argyrodites with phosphorus and arsenic: order and disorder of lithium atoms, crystal chemistry, and phase transitions'. In: *Chemistry–A European Journal* 16.7 (2010), pp. 2198–2206.

[56] Ze Ma, Huai-Guo Xue and Sheng-Ping Guo. 'Recent achievements on sulfide-type solid electrolytes: crystal structures and electrochemical performance'. In: *Journal of materials science* 53.6 (2018), pp. 3927–3938.

[57] Philip Minnmann et al. 'Designing Cathodes and Cathode Active Materials for Solid-State Batteries'. In: *Advanced Energy Materials* 12.35 (2022), p. 2201425.

[58] Qiang Dai et al. 'Life cycle analysis of lithium-ion batteries for automotive applications'. In: *Batteries* 5.2 (2019), p. 48.

[59] Yunxian Qian et al. 'Influence of electrolyte additives on the cathode electrolyte interphase (CEI) formation on LiNi1/3Mn1/3Co1/3O2 in half cells with Li metal counter electrode'. In: *Journal of power sources* 329 (2016), pp. 31–40.

[60] Enrico Trevisanello et al. 'Polycrystalline and single crystalline NCM cathode materials—quantifying particle cracking, active surface area, and lithium diffusion'. In: *Advanced Energy Materials* 11.18 (2021), p. 2003400.

[61] Nicholas PW Pieczonka et al. 'Understanding transition-metal dissolution behavior in LiNi0. 5Mn1. 5O4 high-voltage spinel for lithium ion batteries'. In: *The Journal of Physical Chemistry C* 117.31 (2013), pp. 15947–15957.

[62] Woosuk Cho et al. 'Improved electrochemical and thermal properties of nickel rich LiNi0. 6Co0. 2Mn0. 2O2 cathode materials by SiO2 coating'. In: *Journal of Power Sources* 282 (2015), pp. 45–50.

[63] Tianyu Li et al. 'Degradation mechanisms and mitigation strategies of nickel-rich NMC-based lithium-ion batteries'. In: *Electrochemical Energy Reviews* 3.1 (2020), pp. 43–80.

[64] Felix Walther et al. 'Visualization of the interfacial decomposition of composite cathodes in argyrodite-based all-solid-state batteries using time-of-flight secondary-ion mass spectrometry'. In: *Chemistry of Materials* 31.10 (2019), pp. 3745–3755.

[65] Raimund Koerver et al. 'Redox-active cathode interphases in solid-state batteries'. In: *Journal of Materials Chemistry A* 5.43 (2017), pp. 22750–22760.

[66] Raffael Ruess et al. 'Influence of NCM particle cracking on kinetics of lithium-ion batteries with liquid or solid electrolyte'. In: *Journal of The Electrochemical Society* 167.10 (2020), p. 100532.

[67] N Kaiser et al. 'Ion transport limitations in all-solid-state lithium battery electrodes containing a sulfide-based electrolyte'. In: *Journal of Power Sources* 396 (2018), pp. 175–181.

[68] Tan Shi et al. 'High active material loading in all-solid-state battery electrode via particle size optimization'. In: *Advanced Energy Materials* 10.1 (2020), p. 1902881.

[69] Philip Minnmann et al. 'Editors' choice—quantifying the impact of charge transport bottlenecks in composite cathodes of all-solid-state batteries'. In: *Journal of The Electrochemical Society* 168.4 (2021), p. 040537.

[70] Joonam Park et al. 'Digital Twin-Driven All-Solid-State Battery: Unraveling the Physical and Electrochemical Behaviors'. In: *Advanced Energy Materials* 10.35 (2020), p. 2001563.

[71] Torgeir Matre Sandvik. 'Development of Li3YCl6-Coated NCA Cathode via Mechanofusion and its Electrochemical Evaluation in Argyrodite-Based Solid-State Batteries'. MA thesis. NTNU, 2022.

[72] Dzmitry Hlushkou et al. 'The influence of void space on ion transport in a composite cathode for all-solid-state batteries'. In: *Journal of Power Sources* 396 (2018), pp. 363–370.

[73] Anja Bielefeld et al. 'Influence of Lithium Ion Kinetics, Particle Morphology and Voids on the Electrochemical Performance of Composite Cathodes for All-Solid-State Batteries'. In: *Journal of The Electrochemical Society* 169.2 (2022), p. 020539.

[74] Kun Joong Kim et al. 'Solid-state Li–metal batteries: challenges and horizons of oxide and sulfide solid electrolytes and their interfaces'. In: *Advanced Energy Materials* 11.1 (2021), p. 2002689.

[75] Saneyuki Ohno et al. 'Linking Solid Electrolyte Degradation to Charge Carrier Transport in the Thiophosphate-Based Composite Cathode toward Solid-State Lithium-Sulfur Batteries'. In: *Advanced Functional Materials* 31.18 (2021), p. 2010620.

[76] Darren HS Tan et al. 'Elucidating reversible electrochemical redox of Li6PS5Cl solid electrolyte'. In: *ACS Energy Letters* 4.10 (2019), pp. 2418–2427.

[77] Van-Chuong Ho et al. 'Effect of an organic additive in the electrolyte on suppressing the growth of Li dendrites in Li metal-based batteries'. In: *Electrochimica Acta* 279 (2018), pp. 213–223.

[78] Dae Yang Oh et al. 'All-solid-state lithium-ion batteries with TiS 2 nanosheets and sulphide solid electrolytes'. In: *Journal of Materials Chemistry A* 4.26 (2016), pp. 10329–10335.

[79] Shingo Teragawa et al. 'Liquid-phase synthesis of a Li 3 PS 4 solid electrolyte using N-methylformamide for all-solid-state lithium batteries'. In: *Journal of Materials Chemistry A* 2.14 (2014), pp. 5095–5099.

[80] J Songster and AD Pelton. 'The In-Li (indium-lithium) system'. In: *Journal of phase equilibria* 12.1 (1991), pp. 37–41.

[81] William D Richards et al. 'Interface stability in solid-state batteries'. In: *Chemistry of Materials* 28.1 (2016), pp. 266–273.

[82] Cheng Ma et al. 'Interfacial stability of Li metal–solid electrolyte elucidated via in situ electron microscopy'. In: *Nano letters* 16.11 (2016), pp. 7030–7036.

[83] C John Wen and Robert A Huggins. 'Thermodynamic and mass transport properties of "LiIn"'. In: *Materials Research Bulletin* 15.9 (1980), pp. 1225–1234.

[84] Kazunori Takada et al. 'Solid state lithium battery with oxysulfide glass'. In: *Solid State Ionics* 86 (1996), pp. 877–882.

[85] Samantha A Webb et al. 'The electrochemical reactions of pure indium with Li and Na: anomalous electrolyte decomposition, benefits of FEC additive, phase transitions and electrode performance'. In: *Journal of Power Sources* 248 (2014), pp. 1105–1117.

[86] Zonghai Chen et al. 'Role of surface coating on cathode materials for lithium-ion batteries'. In: *Journal of materials chemistry* 20.36 (2010), pp. 7606–7612.

[87] Cary M Hayner, Xin Zhao and Harold H Kung. 'Materials for rechargeable lithium-ion batteries'. In: *Annual review of chemical and biomolecular engineering* 3 (2012), pp. 445–471.

[88] Kazunori Takada. 'Progress in solid electrolytes toward realizing solid-state lithium batteries'. In: *Journal of Power Sources* 394 (2018), pp. 74–85.

[89] Yizhou Zhu, Xingfeng He and Yifei Mo. 'Origin of outstanding stability in the lithium solid electrolyte materials: insights from thermodynamic analyses based on first-principles calculations'. In: *ACS applied materials & interfaces* 7.42 (2015), pp. 23685–23693.

[90] Sean P Culver et al. 'On the functionality of coatings for cathode active materials in thiophosphate-based all-solid-state batteries'. In: *Advanced Energy Materials* 9.24 (2019), p. 1900626.

[91] Jing Yang et al. 'Structure integrity endowed by a Ti-containing surface layer towards ultrastable LiNi0. 8Co0. 15Al0. 05O2 for all-solid-state lithium batteries'. In: *Journal of The Electrochemical Society* 163.8 (2016), A1530.

[92] Jae Ha Woo et al. 'Nanoscale interface modification of LiCoO2 by Al2O3 atomic layer deposition for solid-state Li batteries'. In: *Journal of The Electrochemical Society* 159.7 (2012), A1120.

[93] Kazunori Takada et al. 'Interfacial phenomena in solid-state lithium battery with sulfide solid electrolyte'. In: *Solid State Ionics* 225 (2012), pp. 594–597.

[94] Atsushi Sakuda, Akitoshi Hayashi and Masahiro Tatsumisago. 'Interfacial observation between LiCoO2 electrode and Li2S- P2S5 solid electrolytes of all-solid-state lithium secondary batteries using transmission electron microscopy'. In: *Chemistry of Materials* 22.3 (2010), pp. 949–956.

[95] Takashi Teranishi et al. 'Aluminum interdiffusion into LiCoO2 using atomic layer deposition for high rate lithium ion batteries'. In: *ACS Applied Energy Materials* 1.7 (2018), pp. 3277–3282.

[96] Wenbo Zhang et al. 'Degradation mechanisms at the Li10GeP2S12/LiCoO2 cathode interface in an all-solid-state lithium-ion battery'. In: *ACS applied materials & interfaces* 10.26 (2018), pp. 22226–22236.

[97] Philippe Knauth. 'Inorganic solid Li ion conductors: An overview'. In: *Solid State Ionics* 180.14-16 (2009), pp. 911–916.

[98] AM Glass, Kurt Nassau and TJ Negran. 'Ionic conductivity of quenched alkali niobate and tantalate glasses'. In: *Journal of Applied Physics* 49.9 (1978), pp. 4808–4811.

[99] AM Glass and K Nassau. 'Lithium ion conduction in rapidly quenched Li2O-Al2O3, Li2O-Ga2O3, and Li2O-Bi2O3 glasses'. In: *Journal of Applied Physics* 51.7 (1980), pp. 3756–3761.

[100] Paul Heitjans and Sylvio Indris. 'Diffusion and ionic conduction in nanocrystalline ceramics'. In: *Journal of Physics: Condensed Matter* 15.30 (2003), R1257.

[101] Yong Jeong Kim et al. 'Suppression of cobalt dissolution from the LiCoO2 cathodes with various metal-oxide coatings'. In: *Journal of The Electrochemical Society* 150.12 (2003), A1723.

[102] Zhaohui Chen and JR Dahn. 'Effect of a ZrO2 coating on the structure and electrochemistry of Li x CoO2 when cycled to 4.5 V'. In: *Electrochemical and solid-state letters* 5.10 (2002), A213.

[103] Yuhua Duan. 'Electronic structural and electrochemical properties of lithium zirconates and their capabilities of CO 2 capture: A first-principles density-functional theory and phonon dynamics approach'. In: *Journal of Renewable and Sustainable Energy* 3.1 (2011), p. 013102.

[104] Gabriele Pannocchia et al. 'Experimental and modeling studies on high-temperature capture of CO2 using lithium zirconate based sorbents'. In: *Industrial & engineering chemistry research* 46.21 (2007), pp. 6696–6706.

[105] K Nakagawa and T Ohashi. 'A novel method of CO 2 capture from high temperature gases'. In: *Journal of the Electrochemical Society* 145.4 (1998), p. 1344.

[106] Yue Xu et al. 'The preparation and role of Li2ZrO3 surface coating LiNi0. 5Co0. 2Mn0. 3O2 as cathode for lithium-ion batteries'. In: *Applied Surface Science* 361 (2016), pp. 150–156.

[107] Bohang Song et al. 'Long-life nickel-rich layered oxide cathodes with a uniform Li2ZrO3 surface coating for lithium-ion batteries'. In: *ACS Applied Materials & Interfaces* 9.11 (2017), pp. 9718–9725.

[108] Hongmei Liang et al. 'Improvement in the electrochemical performance of LiNi0. 8Co0. 1Mn0. 1O2 cathode material by Li2ZrO3 coating'. In: *Applied Surface Science* 423 (2017), pp. 1045–1053.

[109] Zhangxian Chen et al. 'Ultrahigh Capacity Retention of a Li2ZrO3-Coated Ni-Rich LiNi0. 8Co0. 1Mn0. 1O2 Cathode Material through Covalent Interfacial Engineering'. In: *ACS Applied Energy Materials* 4.12 (2021), pp. 13785–13795.

[110] Zhaoxin Guo et al. 'Amorphous Li2ZrO3 nanoparticles coating Li [Li0· 17Mn0· 58Ni0. 25] O2 cathode material for enhanced rate and cyclic performance in lithium ion storage'. In: *Materials Chemistry and Physics* 255 (2020), p. 123593.

[111] Mengjie Yu et al. 'Stabilizing High-Voltage Cathodes via Ball-Mill Coating with Flame-Made Nanopowder Electrolytes'. In: *ACS Applied Materials & Interfaces* (2022).

[112] Lingjun Li et al. 'Role of residual Li and oxygen vacancies in Ni-rich cathode materials'. In: *ACS Applied Materials & Interfaces* 13.36 (2021), pp. 42554–42563.

[113] Xing Li et al. 'Dual functions of zirconium modification on improving the electrochemical performance of Ni-rich LiNi 0.8 Co 0.1 Mn 0.1 O 2'. In: *Sustainable energy & fuels* 2.2 (2018), pp. 413–421.

[114] Jia Yang et al. 'New insight into lattice variations of Ni-rich NMC811 cathode induced by Li2ZrO3 coating'. In: *Materials Technology* 37.11 (2022), pp. 1926–1935.

[115] Ze Feng et al. 'A three in one strategy to achieve zirconium doping, boron doping, and interfacial coating for stable LiNi0. 8Co0. 1Mn0. 1O2 cathode'. In: *Advanced Science* 8.2 (2021), p. 2001809.

[116] João C Barbosa et al. 'Recent advances on materials for lithium-ion batteries'. In: *Energies* 14.11 (2021), p. 3145.

[117] Alexandria RC Bredar et al. 'Electrochemical impedance spectroscopy of metal oxide electrodes for energy applications'. In: *ACS Applied Energy Materials* 3.1 (2020), pp. 66–98.

[118] Aldahir A Hernández-Hernández et al. 'Iron oxide nanoparticles: synthesis, functionalization, and applications in diagnosis and treatment of cancer'. In: *Chemical Papers* 74.11 (2020), pp. 3809–3824.

[119] Sang Myoung Lee et al. 'The effect of zirconium oxide coating on the lithium nickel cobalt oxide for lithium secondary batteries'. In: *Electrochimica acta* 52.4 (2006), pp. 1507–1513.

[120] Petr Slepička et al. 'Methods of gold and silver nanoparticles preparation'. In: *Materials* 13.1 (2019), p. 1.

[121] Shi-Zhao Kang et al. 'Low temperature biomimetic synthesis of the Li2ZrO3 nanoparticles containing Li6Zr2O7 and high temperature CO2 capture'. In: *Materials Letters* 64.12 (2010), pp. 1404–1406.

[122] Liubin Ben et al. 'Unusual spinel-to-layered transformation in LiMn2O4 cathode explained by electrochemical and thermal stability investigation'. In: *ACS applied materials & interfaces* 9.40 (2017), pp. 35463–35475.

[123] Daxian Zuo et al. 'Recent progress in surface coating of cathode materials for lithium ion secondary batteries'. In: *Journal of Alloys and Compounds* 706 (2017), pp. 24–40.

[124] Hirokazu Kitaura et al. 'Improvement of electrochemical performance of all-solid-state lithium secondary batteries by surface modification of LiMn2O4 positive electrode'. In: *Solid State Ionics* 192.1 (2011), pp. 304–307.

[125] Atsushi Sakuda, Akitoshi Hayashi and Masahiro Tatsumisago. 'Electrochemical performance of all-solid-state lithium secondary batteries improved by the coating of Li2O–TiO2 films on LiCoO2 electrode'. In: *Journal of Power Sources* 195.2 (2010), pp. 599–603.

[126] Sungwoo Noh et al. 'Surface modification of LiCoO2 with Li3xLa2/3- xTiO3 for all-solid-state lithium ion batteries using Li2S–P2S5 glass–ceramic'. In: *Ceramics International* 39.7 (2013), pp. 8453–8458.

[127] Nobuya Machida et al. 'Electrochemical properties of all-solid-state batteries with ZrO2-coated LiNi1/3Mn1/3Co1/3O2 as cathode materials'. In: *Solid State Ionics* 225 (2012), pp. 354–358.

[128] Kazuya Okada et al. 'Preparation and electrochemical properties of LiAlO2-coated NMC111 for all-solid-state batteries'. In: *Solid State Ionics* 255 (2014), pp. 120–127.

[129] Akira Yano et al. 'Surface structure and high-voltage charge/discharge characteristics of Al-oxide coated LiNi1/3Co1/3Mn1/3O2 cathodes'. In: *Journal of the Electrochemical Society* 162.2 (2015), A3137.

[130] Rajendra Singh Negi. 'Surface Coatings of Nickel-Rich NCM Based Cathode Active Materials for Improved Electrochemical Performance of Lithium-Ion Batteries'. In: (2021).

[131] Camelia V Stan et al. 'X-ray diffraction under extreme conditions at the Advanced Light Source'. In: *Quantum Beam Science* 2.1 (2018), p. 4.

[132] Weilie Zhou et al. 'Fundamentals of scanning electron microscopy (SEM)'. In: *Scanning microscopy for nanotechnology*. Springer, 2006, pp. 1–40.

[133] Lina Li et al. 'Effect of Zr doping and Al-Zr co-doping on LiNi0. 5Co0. 25Mn0. 25O2 for lithium-ion batteries'. In: *Solid State Ionics* 346 (2020), p. 115220.

[134] Yi Lu et al. 'Enhanced electrochemical properties of Zr4+-doped Li1. 20 [Mn0. 52Ni0. 20Co0. 08] O2 cathode material for Lithium-ion battery at elevated temperature'. In: *Scientific Reports* 8.1 (2018), pp. 1–14.

[135] Li Zhao, Qing Wu and Jinzhu Wu. 'Improving rate performance of cathode material Li1. 2Mn0. 54Co0. 13Ni0. 13O2 via niobium doping'. In: *Journal of Solid State Electrochemistry* 22.7 (2018), pp. 2141–2148.

[136] *NMC BATTERY MATERIAL (LINIMNCOO2) Targray*. https://www.targray.com/li-ion-battery/cathode-materials/nmc.

[137] Alexander Quinn et al. 'Electron backscatter diffraction for investigating lithium-ion electrode particle architectures'. In: *Cell Reports Physical Science* 1.8 (2020), p. 100137.

[138] *Microwave Plasma Atomic Emission Spectroscopy (MP-AES)*. https://www.agilent.com/en/product/atomic-spectroscopy/microwave-plasma-atomic-emission-spectroscopy-mp-aes.

[139] Dmitry Bokov et al. 'Nanomaterial by sol-gel method: synthesis and application'. In: *Advances in Materials Science and Engineering* 2021 (2021).

[140] Ding Wang et al. ‘Improved high voltage electrochemical performance of Li2ZrO3-coated LiNi0. 5Co0. 2Mn0. 3O2 cathode material’. In: *Journal of Alloys and Compounds* 647 (2015), pp. 612–619.

[141] Florian Schipper et al. ‘From surface ZrO2 coating to bulk Zr doping by high temperature annealing of nickel-rich lithiated oxides and their enhanced electrochemical performance in lithium ion batteries’. In: *Advanced Energy Materials* 8.4 (2018), p. 1701682.

[142] Chiara Busà, Meltiani Belekoukia and Melanie J Loveridge. ‘The effects of ambient storage conditions on the structural and electrochemical properties of NMC-811 cathodes for Li-ion batteries’. In: *Electrochimica Acta* 366 (2021), p. 137358.

[143] Kui Meng et al. ‘Improving the cycling performance of LiNi0. 8Co0. 1Mn0. 1O2 by surface coating with Li2TiO3’. In: *Electrochimica Acta* 211 (2016), pp. 822–831.

[144] Xiaowen Zhan, Shuang Gao and Yang-Tse Cheng. ‘Influence of annealing atmosphere on Li2ZrO3-coated LiNi0. 6Co0. 2Mn0. 2O2 and its high-voltage cycling performance’. In: *Electrochimica Acta* 300 (2019), pp. 36–44.

[145] Young-Jin Kim et al. ‘Novel dry deposition of LiNbO3 or Li2ZrO3 on LiNi0. 6Co0. 2Mn0. 2O2 for high performance all-solid-state lithium batteries’. In: *Chemical Engineering Journal* 386 (2020), p. 123975.

[146] Simone Raoux et al. ‘Direct observation of amorphous to crystalline phase transitions in nanoparticle arrays of phase change materials’. In: *Journal of Applied Physics* 102.9 (2007), p. 094305.

[147] Taichi Sato et al. ‘Thermal decomposition of zirconium hydroxide’. In: *Thermochimica Acta* 34.2 (1979), pp. 211–220.

[148] Jun Su Lee and Yong Joon Park. ‘Comparison of LiTaO3 and LiNbO3 surface layers prepared by post-and precursor-based coating methods for Ni-rich cathodes of all-solid-state batteries’. In: *ACS Applied Materials & Interfaces* 13.32 (2021), pp. 38333–38345.

[149] Eman Hassan et al. ‘Effects of Coating on the Electrochemical Performance of a Nickel-Rich Cathode Active Material’. In: *Energies* 15.13 (2022), p. 4886.

Appendix

All the raw data could be found in this SharePoint folder. Because of the large size of the EDX mapping data folder, it can be found on the Nanonet NTNU system under the user name: quocat

https://studntnu-my.sharepoint.com/:f:/r/personal/quocat_ntnu_no/Documents/Appendix%20-%20Master%20Thesis%20Project?csf=1&web=1&e=OiDFLu

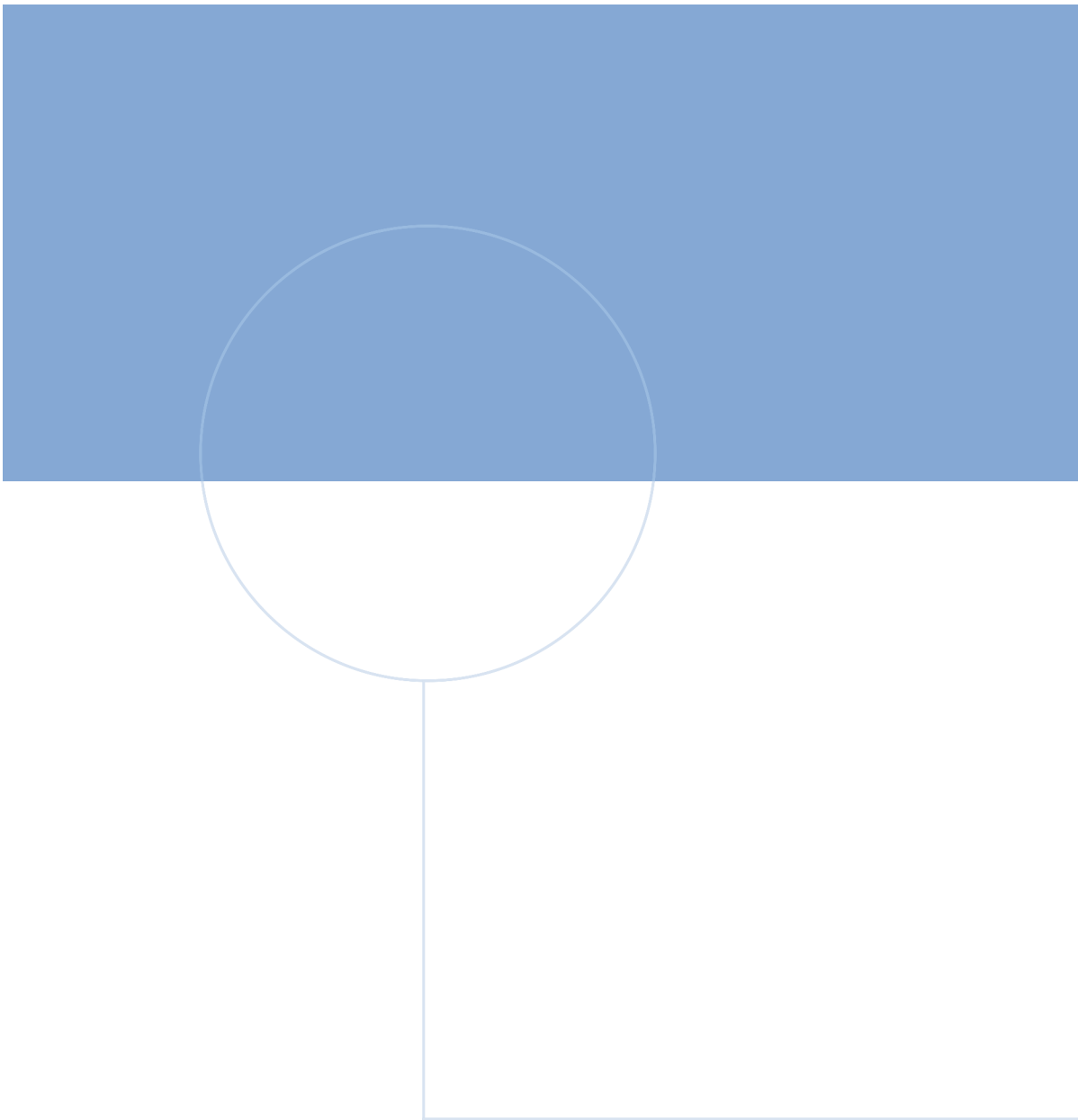

NTNU

Norwegian University of
Science and Technology